



HAL
open science

Numerical study of particle transport and deposition in porous media

Jianhua Fan

► **To cite this version:**

Jianhua Fan. Numerical study of particle transport and deposition in porous media. Fluids mechanics [physics.class-ph]. INSA de Rennes, 2018. English. NNT : 2018ISAR0003 . tel-01801207

HAL Id: tel-01801207

<https://theses.hal.science/tel-01801207>

Submitted on 28 May 2018

HAL is a multi-disciplinary open access archive for the deposit and dissemination of scientific research documents, whether they are published or not. The documents may come from teaching and research institutions in France or abroad, or from public or private research centers.

L'archive ouverte pluridisciplinaire **HAL**, est destinée au dépôt et à la diffusion de documents scientifiques de niveau recherche, publiés ou non, émanant des établissements d'enseignement et de recherche français ou étrangers, des laboratoires publics ou privés.

Thèse

UNIVERSITE
BRETAGNE
LOIRE

THESE INSA Rennes
sous le sceau de l'Université Bretagne Loire
pour obtenir le titre de
DOCTEUR DE L'INSA RENNES
Spécialité : Génie Civil

présentée par

Jianhua FAN

ECOLE DOCTORALE : SPI
LABORATOIRE : LGCGM

Numerical study of particle transport and deposition in porous media

Thèse soutenue le 29.03.2018
devant le jury composé de :

Azita AHMADI SENICHAULT

Professeur - ENSAM de Bordeaux / Président

Anthony BEAUDOIN

Maître de Conférences HDR - Université de Poitiers / Rapporteur

Nicolas LECOQ

Maître de Conférences HDR - Université Normandie (Rouen) /
Rapporteur

Dominique HEITZ

Chargé de recherche HDR - IRSTEA Rennes / Examineur

Huaqing WANG

Professeur - Université Normandie (Le Havre) / Examineur

Juan MARTINEZ

Professeur Emérite - INSA de Rennes / Examineur

Franck LOMINÉ

Maître de Conférences - INSA de Rennes / Co-encadrant de thèse

Mustapha HELLOU

Professeur - INSA de Rennes / Directeur de thèse



Numerical study of particle transport and deposition in porous media

Jianhua Fan



En partenariat avec



Acknowledgements

I would like to express my sincere gratitude to my advisors Prof. Mustapha Hellou and MCF Franck Lominé for the continuous support and valuable discussion during my Ph.D studies. Great thanks should be given to MCF Franck Lominé who devoted great time and efforts to the code used in my thesis. These two advisors helped me not only in research work but also in daily life. I learned a lot from their serious attitude and passion for life and work.

This work has been supported by China Scholarship Council (CSC) and INSA de Rennes. I would like to thank CSC for the financial support and the opportunity to study in France.

I also wish to express my thanks to the rapporteurs, MCF-HDR Anthony BEAUDOIN and MCF-HDR Nicloas LECOQ, and all the members of the committee, Prof. Azita AHMADI SENICHAULT, Prof. Juan MARTINEZ, researcher-HDR Dominique HEITZ and Prof. Huaqing WANG, for taking time to review this dissertation.

My special thanks would give to the teachers and all the Ph.D students in the laboratory: Prof.f Fekri Meftah, MCF Khaled Mohamed Bourbatache, Dr. Guilherme Fiorot, Jia Fu, Ilham Benhsine, Saly Serhal, Sambath Ky, Tran Van Hieu. Nelson Alvarado Patino, Ramez Baydoun, Chuan Chen, Boyuan Yang, Qingxiang Xiong.

I would like to thank Prof.f Yongbo Deng and all my friends from INSA de Rennes: Dr. Yi Liu, Tian Xia, Jiali Xu, Hengyang Wei, Shibo Liu, Gang Huang. Shijiang Wang, Hua Lu, Xiao Song, Yong Huang, Shijian Tian, Haiyun Yao, Qiong Wang, Ang Zhou, Yang Zhang, Ye Tian, Jinzeng Wang, Limiao Shi, Jiabin Liang, Jingjun Gao, for their encouragement and friend ship letting me feel happy and warm in the foreign country.

More important, I would like to sincerely thank my parents who give me encouragement, support, understanding for my study. Then I would like to thank Lu Wang who gives me sufficient supports, joys and love. They give me great power to complete my doctorate study. I love you, thank you for your effort and selfless dedication!

Contents

Introduction	1
1 Literature review on hydrodynamic and mechanical interaction of fluid and solid particles	7
1.1 Introduction	7
1.2 Flow of suspensions through porous medium	7
1.2.1 Governing equations in fluid flow	7
1.2.2 Porous media	9
1.2.2.1 Porosity of porous media	9
1.2.2.2 Characteristic of stack for sphere porous media	9
1.2.2.3 Particles deposition in porous media	12
1.2.3 Fluid flow in porous media	14
1.2.3.1 Darcy's law	14
1.2.3.2 Kozeny-Carman equation	15
1.2.3.3 Kuwabara solution	16
1.3 Filtration	19
1.3.1 Filtration type	19
1.3.2 Quality factor	22
1.3.3 Filtration efficiency	22
1.3.4 Single fiber capture efficiency	24
1.3.5 Capture mechanism	26
1.3.5.1 Brownian diffusion	26
1.3.5.2 Interception	28
1.3.5.3 Inertial impaction	29
1.3.6 Retention sites	33
1.3.7 Pressure drop across a filter	34

1.4	Numerical modeling for fluid-particle flows	35
1.4.1	Numerical methods for fluid phase	37
1.4.2	Numerical methods for solid phase	38
1.4.3	Choice of numerical method	39
1.5	Summary of earlier researchers' results for particle filtration	39
1.5.1	Particle capture on a single fiber	39
1.5.1.1	Particle capture on circular fiber	39
1.5.1.2	Particle capture on non-circular fiber	40
1.5.2	Particle transport in filter with multi-fiber	42
1.6	Conclusion	44
2	Lattice Boltzmann and Discrete Element methods	47
2.1	Introduction	47
2.2	Lattice Boltzmann method	49
2.2.1	Principle of lattice Boltzmann method	49
2.2.2	Boundary conditions on obstacles and systems	51
2.2.2.1	Boundary conditions on obstacles	51
2.2.2.2	Boundary conditions on systems	53
2.3	Discrete element method	58
2.3.1	Contact law	58
2.3.2	Normal contact force	59
2.3.3	Shear contact force	61
2.3.4	Particle dynamics	62
2.4	Coupling of LBM-DEM	63
2.4.1	Subcycling time integration	63
2.4.2	Forces and torques acting on the particles	65
2.5	Validations of LBM-DEM	66
2.5.1	2D Poiseuille flow	66
2.5.2	Couette flow	69
2.5.3	Flow around a fixed cylinder in 2D	71
2.5.4	Flow in porous media	74
2.5.5	Moving cylinder in channel flow	76
2.6	Conclusion	78

3	Numerical simulation of particle capture on single fiber	79
3.1	Introduction	79
3.2	One particle injection	80
3.2.1	Model description	80
3.2.2	One-way coupling	81
3.2.2.1	Particle motion of equation	82
3.2.2.2	Particle trajectory analysis	83
3.2.3	Two-way coupling	86
3.2.3.1	The effect of particle size	86
3.2.3.2	The effect of fiber shape	88
3.2.3.3	Quality factor of filter	89
3.3	Several particles injection	92
3.3.1	Particles injected at projected area of fiber	92
3.3.1.1	Model description	92
3.3.1.2	Capture efficiency of circular fiber	93
3.3.1.3	Capture efficiency of diamond and square fiber	95
3.3.1.4	Quality factor of filter for serveral particles injected	99
3.3.2	Particles injected along whole inlet	100
3.3.2.1	Model description	100
3.3.2.2	Pressure drop of clean filter	102
3.3.2.3	Filtration efficiency of filter	107
3.3.2.4	Quality factor of filter with rectangular fiber	110
3.4	Conclusion	114
4	Numerical simulation of filtration process for filter with staggered fibers	117
4.1	Introduction	117
4.2	Circular fiber arrangements	118
4.3	Numerical study of particles motion and deposition on staggered arrayed fibers with various shapes	122
4.3.1	Model description and filtration parameters	122
4.3.2	Pressure drop of clean filter with staggered fibers	124
4.3.3	Filtration efficiency of filter with staggered fibers	126
4.3.4	Capture contribution of each fiber to the filtration efficiency	134
4.3.5	Quality factor of filter with staggered fibers	139
4.4	Conclusions	141

Conclusion and perspectives	143
List of symbols	147
List of figures	149
Bibliography	155
Résumé en français	171

Introduction

Fluid-solid two phase flow widely exists in nature and engineering such as mining and cement industries, particle transport in porous media, industry of power generation as well as environmental engineering [1, 2, 3]. The response of solid phase can be strongly affected by the action of the fluid phase, i.e. fluidized bed reactor [4], pipe leakage [5], poured concrete for construction [6]. The fluid phase is characterized by its velocity and pressure and exerts hydrodynamic force on the interface of the solid, which leads to movement of the solid under its action. In turn, the distribution of flow velocity field varies due to the presence of the solid. This retroaction of the interaction between the fluid and the solid makes the problem of fluid-solid far more complex than its single-phase counterpart.

There are a variety of phenomena involving both fluids, mainly water or air, and solid particles. These phenomena raise a great number of scientific problems in terms of the complexity of physical mechanisms. The transport of solid particles suspended in fluid takes place in many physical processes [7], such as sediment transport, debris flow, soil erosion, filtration etc. To gain fundamental insight in fluid-solid systems, some examples of problems involving fluid-solid interactions are presented in Fig.1 and Fig.2

Particles involve in industrial emissions, which leads to contamination that directly bring about an antagonistic effect on human environment. It is essential to remove particles from their surrounding sources. The problem of removing particles from fluid has become increasingly significant from the point of reducing health hazard [10]. Thus an efficient fluid-solid separation system is required to deal with the problem of fluid purification.

Fluid-particle separation refers also to a process for filtrating particles from fluid. Filtration, one of the particle separation processes, is a very important technology [11] and occurs in human activities, examples include improving cement grouting in civil engineering [12], transport of colloids through the groundwater [13], the design of granular filter in chemical and biological engineering process [14], blood separation in microfluidic device [15]. One of the examples of filtration application is shown in Fig.3. Fig.3 illustrates the

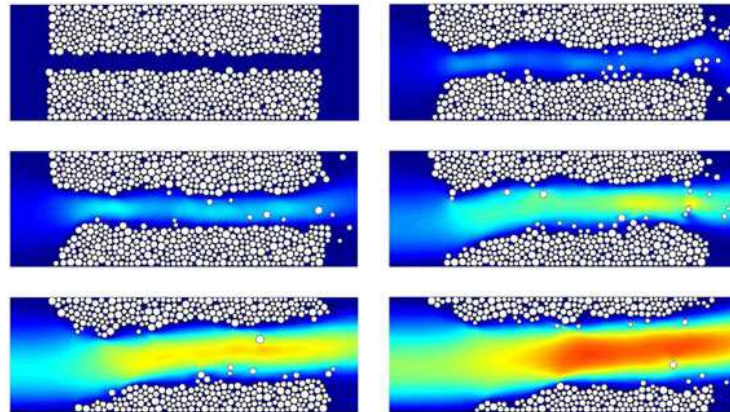


Figure 1: Example of problem involving fluid-solid interactions: snapshots from the numerical simulation of piping erosion [8]. Particles are detached under the hydraulic loading. Then, detached particles are transported by the flow toward the channel outlet.

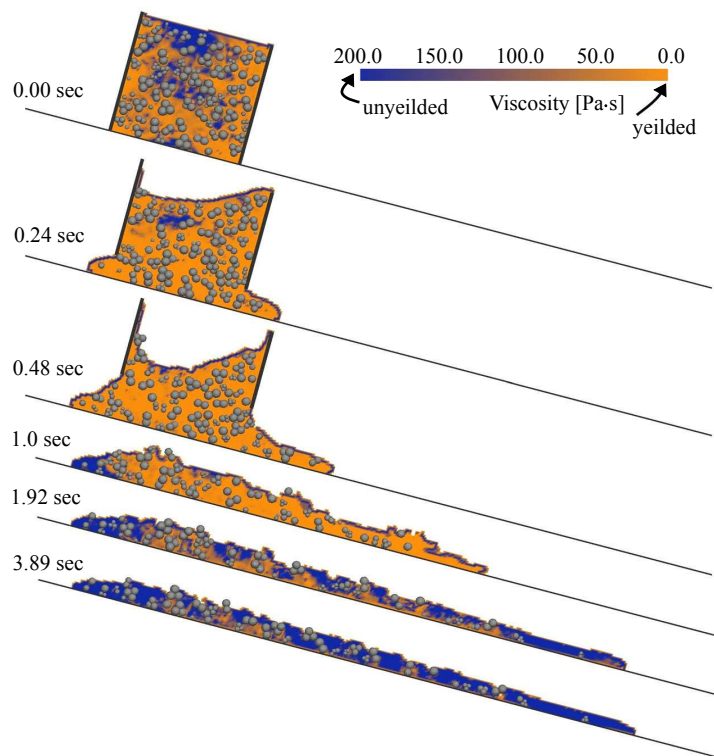


Figure 2: Example of problem fluid-solid involving interactions: gravity-driven flow [9], particles are represented in light gray and walls in dark gray. The yielded region of the fluid grows from a small portion to the whole sample. When a new equilibrium is reached, the yielded region reduces and the flow is slowed.

particle filtration stage and clean stage (top) and particle separation process (bottom) [16].

The separation technology is basic to a large number of manufacturing industries as well as environment control [14]. While understanding fluid-particle behavior seems remarkably advanced. For example, improving the particle filtration efficiency in industry can decrease the air pollution. Since particles being carried within fluid flows involved in interactions between fluid-particle, particle-particle and complex flow phenomena in the combined region, it is still difficult for us to control. To investigate such problem, a deep insight into the fluid-particle flow is required. Our objective is to study the phenomena of the particle transport and deposition in filters at the particle scale using numerical technique in this research. Quality factor, filtration efficiency and pressure drop of filter used to evaluate the filtration performance are investigated. To achieve this goal, the thesis is organized by four chapters. A brief outline of each chapter is described below.

Chapter 1 reviews the literature about fluid-solid flow. More specifically, it presents the flow of suspensions through porous medium, numerical modeling for fluid-particle flows and particle filtration process. The objective of this chapter is to present physical phenomena involved and used to describe fluid-particle interaction at particle scale. A summary of main studies and results are also presented with a quick review of numerical method that can be used to simulate such fluid-solid problems.

Chapter 2 presents a numerical method to simulate particle transport and deposition. This method is based on a coupled Lattice Boltzmann Method (LBM) and Discrete Element Method (DEM), whereas LBM is used to calculate the fluid and DEM is employed to deal with particle dynamics. The process for coupling of LBM-DEM is also described. The corresponding method is two-way coupling in the sense that particle motion affects the fluid flow and reciprocally. In order to validate the LBM and DEM, the classical fluid mechanics solutions are used to compare our simulation results.

Chapter 3 investigates particle capture on a single fiber with one-way coupling and two-way coupling methods. LBM with Lagrangian point-like approach as one-way coupling, where LBM-DEM considering the back-up influence of particle on fluid as two-way coupling. The particle trajectory and capture efficiency characterized by Stokes number are analyzed. The single fiber capture efficiency for circular, diamond and square cross-section is determined using the coupled LBM-DEM. The simulation results are compared with the work in literature. In this chapter we also studies filtration efficiency of filter with rectangular fiber. The influence of orientation angle and aspect ratio of rectangular fiber on pressure drop, filtration efficiency and quality factor for various Reynolds numbers are

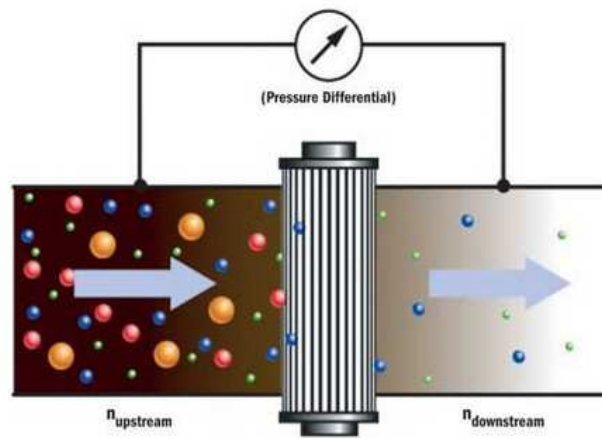
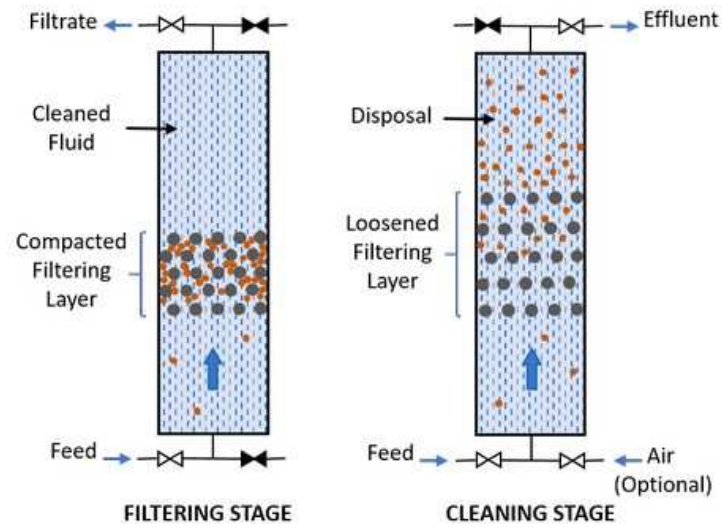


Figure 3: Filtration application, top: filtering stage and clean stage, bottom: particle separation process, n_{upstream} and $n_{\text{downstream}}$ represent the number of particle, at the upstream and downstream respectively [16].

numerically investigated. This study reveals very interesting points that can be helpful to optimize performance of filter.

Chapter 4 focus on the influence of arrangement of fiber on filtration process. The circular, diamond and square fiber are staggered arranged in a filter. The effects of Reynolds number, particle-to-fiber diameter ratio and particle-to-fluid density ratio on pressure drop and filtration efficiency of filter are investigated. The simulation results are compared to explore the fiber's cross-sectional shape effect on quality factor.

Finally, we summarize the general conclusions of the thesis and make recommendations for future work.

Chapter 1

Literature review on hydrodynamic and mechanical interaction of fluid and solid particles

1.1 Introduction

Particle transport in fluid flows has a wide range of applications. This phenomenon generally refers to fluid-particle and particle-particle interactions. These interactions lead to the complexity of flow field. For this reason, a flow field is initially needed. Then suspended particles flows in porous media can be described. Thus the objective of this chapter is to introduce the physical phenomena involved in particle transport and deposition in porous media at the particle scale. In this chapter, we first introduce the governing equation used for flow field and describe the porous media and fluid flow in porous media. Since the particle filtration is commonly used to describe the fluid-particle problems. Then the filtration parameters and capture mechanisms as well as the numerical methods are introduced. Finally some previous results about particle filtration in literature are presented.

1.2 Flow of suspensions through porous medium

1.2.1 Governing equations in fluid flow

In order to study the transport and deposition of particles flow through porous media, it is first of all necessary to analyze velocity flow field through porous media under steady state.

Generally, for the flow field, the classical approach is based on the numerical solution of Navier-Stokes equations [17]. Navier-Stokes equations are first numerically solved by using the finite volume method developed by Patankar [18]. The fluid phase is often viewed as a continuum for practical purposes in Navier-Stokes equations.

Continuity equation

The mass conservation law is known as the equation of continuity. In fluid dynamics, the rate of fluid mass enters a small stationary volume element is equal to the fluid mass leaving the volume element. It can be written as [19]:

$$\frac{\partial \rho}{\partial t} + \nabla \cdot (\rho \vec{u}) = 0 \quad (1.1)$$

where ρ is fluid density and \vec{u} is fluid velocity. The behavior of a fluid in porous medium should conform to this equation. For incompressible fluids with constant density, then ρ is constant in Eq.(1.1) and the continuity equation can reduce to:

$$\nabla \cdot \vec{u} = 0 \quad (1.2)$$

Navier-Stokes equations

The Navier-Stokes equations for flow of fluids of single phase are well accepted and closed-form solution for specific cases are well documented [20]. For constant fluid density ρ and constant viscosity μ , one form of the Navier-Stokes equations is expressed as:

$$\rho \left(\frac{\partial \vec{u}}{\partial t} + \vec{u} \cdot \nabla \vec{u} \right) = -\nabla p + \mu \nabla^2 \vec{u} + \rho \vec{f}_b \quad (1.3)$$

Navier-Stokes equations describe the momentum and mass conservation of fluid phase at time t with velocity \vec{u} , pressure p , dynamic viscosity μ and applied body force per unit mass \vec{f}_b . It is used for calculating flow in incompressible fluids.

Reynolds number (Re) is an important dimensionless quantity in fluid mechanics. Re is a criterion to determine the relative importance of inertial and viscous effects and defined as:

$$Re = \frac{\rho U D_f}{\mu} \quad (1.4)$$

where D_f is the characteristic length of porous media. Reynolds number is often used to

predict flow patterns. For general flow such as piping flow, when the Re is lower a critical value 2000 which is validated by experimental data [21], the flow is called laminar flow. However, for $Re > 2000$, the flow is called turbulent flow. For porous media, this limit is equal to 160 for Reynolds number. In laminar flow regime, if the Reynolds number is very small, much less than 1, the fluid is called creeping flow, where the viscous forces of the fluid dominate the inertial forces.

1.2.2 Porous media

1.2.2.1 Porosity of porous media

A porous medium is constituted by a solid matrix and voids called pores. These pores can be partially or completely filled with water, air and other fluid. Generally the fraction of volume of pores over the total volume in porous media is called porosity ϕ varying between 0 and 1. It is defined as the ratio of the volume of pores to the total sample volume.

$$\phi = \frac{\text{volume of pore}}{\text{total sample volume}} \quad (1.5)$$

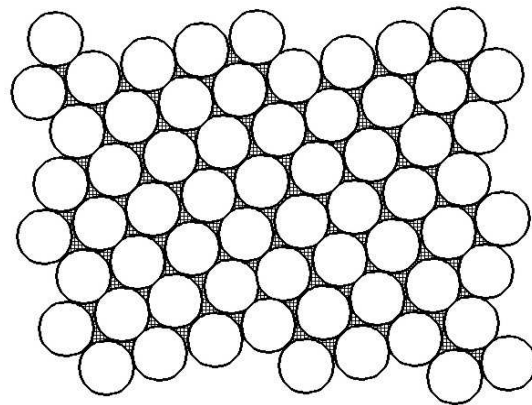
In a general way, there are three types of porosity, intergranular porosity, fracture porosity and cavernous porosity as illustrated in Fig.1.1 [22]. Intergranular porosity is encountered between the grains of soil, sediment, or incompletely cemented sedimentary rock. As shown in Fig.1.1 (a), the circles represent grains and cross-hatching represents the pore space. Fracture porosity is produced by the tectonic fracturing of rock. Crosses represent rock and black is fractures in Fig.1.1 (b). Cavernous porosity only occurs in rocks that can be chemically weathered by solution. The black region has been dissolved and filled with air as shown in Fig.1.1 (c), the blue region is almost filled with groundwater.

The porosity has the relationship with the volume occupied by the solid termed as solid volume fraction (or packing density) and can be given by:

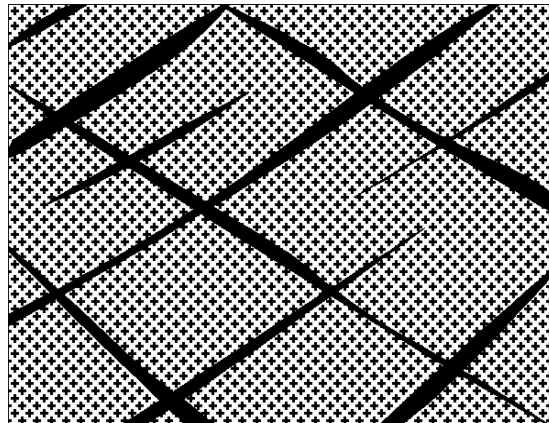
$$\Psi = 1 - \phi \quad (1.6)$$

1.2.2.2 Characteristic of stack for sphere porous media

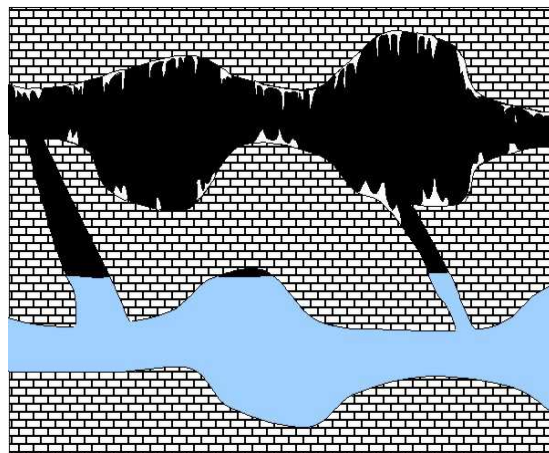
Consider the porous medium composed of sphere grains on periodic cubic lattice. The sphere grains touched each other and they are not compacted any more. The size of all the sphere are identical. The proportion of space filled by the spheres is called the packing



(a)



(b)



(c)

Figure 1.1: Porosity type (a) intergranular porosity, (b) fracture porosity, (c) cavernous porosity [22].

density. In three dimensions, the most four common types of unit cell are the simple cubic (SC), body-centered cubic (BCC), face-centered cubic (FCC) and hexagonal close packing (HCP) [23, 24, 25, 26] as presented in Fig.1.2. In Fig.1.2, the neighbouring sphere grain should contact each other, here we just show the location of each sphere for the sake of simplicity. Then the packing density of each cubic are presented in Table 1.1:

Table 1.1: Packing density.

Type of packing	SC	BCC	FCC	HCP
Packing density	$\frac{\pi}{6}$	$\frac{\sqrt{3}\pi}{8}$	$\frac{\sqrt{2}\pi}{6}$	$\frac{\sqrt{2}\pi}{6}$

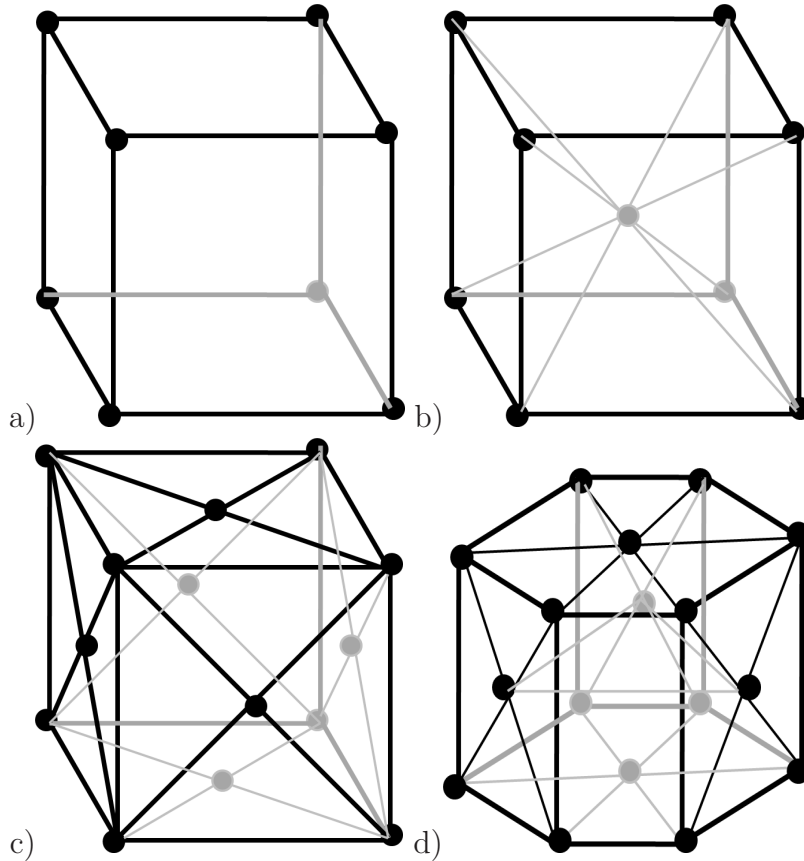


Figure 1.2: The structures for stacks of monotonous spheres, a) SC , b) BCC, c) FCC, d) HCP.

For type of SC, BCC, FCC and HCP, the maximum porosity of porous media is SC which has the minimum packing density. The porosity of SC is equal to $1 - \pi/6 = 47.6\%$. Another two simple arrangements within the close-packed packing correspond to regular

lattices. One is FCC and the bottom of FCC is triangle. Whereas, another is HCP and the bottom of HCP is hexagon. For FCC and HCP, each sphere is surrounded by 12 other spheres. Then the porosity of BCC and HCP is $1 - \frac{\sqrt{2}\pi}{6} = 25.9\%$.

When the sphere grains are randomly arranged, the packing density varies between the random loose packing (RLP) and the random close packing(RCP) [27]. The packing density for upper limit is referred to RCP $\Psi_{RCP} = 64\%$ and $\phi_{RCP} = 36\%$, the lower limit is RLP $\Psi_{RLP} = 56\%$ and $\phi_{RLP} = 34\%$ [27, 28].

1.2.2.3 Particles deposition in porous media

Particle size distribution

In the study of particles transport and deposition in porous media, particle size is a very important parameter which governs the flow of a dispersed two-phase mixture. Porous medium such as soils and sands are often described by their particle size distribution. Particle size distribution is often a critical parameter in the manufacture of many products [29, 30]. It can be used to predict physical properties such as permeability and porosity [31]. The most general definition of the spread of the particle size distribution is monodisperse or polydisperse. A monodisperse distribution is one in which the particles are all of the same size, whereas polydisperse suggests a wide range of particle sizes.

A typical example of particle size distribution of sand is given in Fig.1.3 [32]. It shows the percentage passing of a particular particle as a function of particle size. From Fig.1.3, for a certain size of particle, we can easily know the percentage passing of a particular particle size. For example in Fig.1.3, the particle size distribution is nearly 10% for 10 μm .

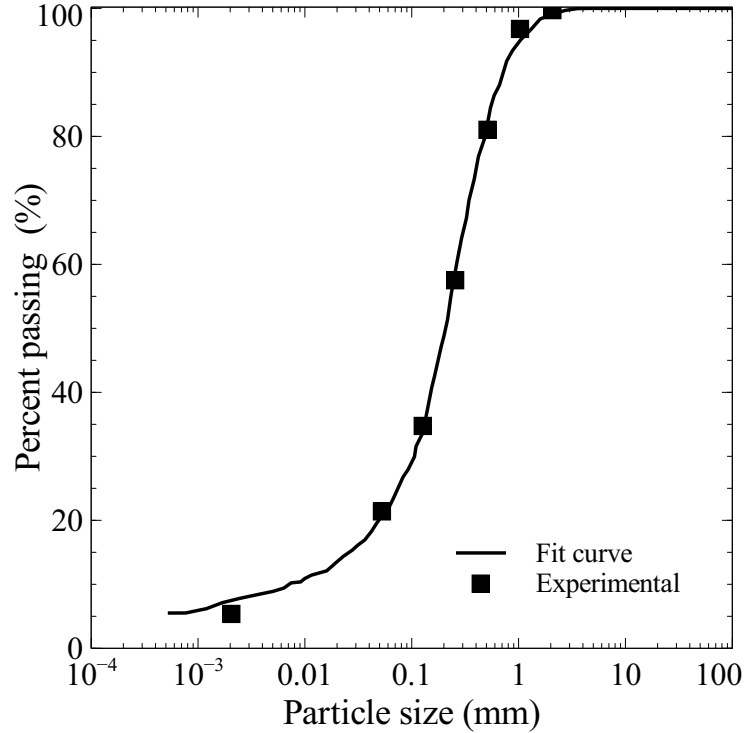


Figure 1.3: Example of particle size distribution curve [30].

Particle straining in constriction

The clogging of a porous media is characterized by the ratio between diameter of particles d_p and diameter of grains D_f . A particle penetrates a triangular constriction formed by three tangent spherical grains as shown in Fig.1.4. There exist a limit for particles, the limit can be determined by the following relation [33]:

$$\left\langle \frac{d_p}{D_f} \right\rangle_{\text{limit}} = \left(\frac{2}{\sqrt{3}} - 1 \right) = 0.154 \quad (1.7)$$

Above this limit, the pore size is smaller than diameter of particle, no particle can penetrate through the constriction and all particles are captured by the grains. If $\frac{d_p}{D_f} < 0.154$, the clogging of porous medium is weak and particle can easily be transported from the pore.

It is also possible to determine the straining by several particles. For three particles and four particles, the limit are respectively:

$$\left\langle \frac{d_p}{D_f} \right\rangle_{\text{limit}} = 0.1 \quad (1.8)$$

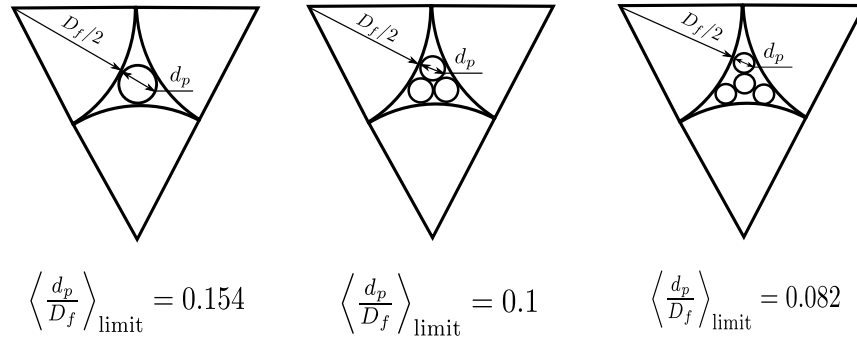


Figure 1.4: The threshold of particles trapped in a triangular construction [33].

$$\left\langle \frac{d_p}{D_f} \right\rangle_{\text{limit}} = 0.082 \quad (1.9)$$

It is noticed that simultaneous arrival of particle is not necessary for straining. However, straining may occur by the successive stoppages of particles. As the constriction is blocked, all particles entrained by fluid are retained at this place.

1.2.3 Fluid flow in porous media

The pore structure in porous media is often complex and complicated flow patterns exist within the pores and between the grains. Permeability is a measure of the ability of a porous medium to be traversed by an interstitial fluid flow. It is commonly used to investigate the effect of pore structure on the properties of porous media [34]. In general, the porous media are characterized by porosity and permeability. These two intrinsic magnitudes are macroscopic variables estimated on a representative elementary volume containing a large number of microscopic entities composing the material.

1.2.3.1 Darcy's law

Fluid flow through porous media plays an important role in a variety of engineering system. Here we consider the saturated porous media for which the volume of the pores is completely filled with fluid. Permeability and pressure drop are two important parameters in porous media. Darcy's law which regards the medium as continuum is satisfactory for the prediction of flow through porous media [35]. Here the considered porous medium is homogeneous and isotropic. Thus, the pressure drop corresponding to a desired flow rate through the porous medium can be obtained by Darcy's law:

$$Q = \frac{-\kappa A \Delta p}{\mu L} \quad (1.10)$$

Where Q is the volume flow rate, μ is the dynamic viscosity of fluid. κ and A are respectively permeability of the medium and a cross-sectional area perpendicular to the fluid flow direction. Δp is the total pressure drop between inlet and outlet, L is total length on which the pressure difference acts.

$$Q = V_D A \quad (1.11)$$

$$\vec{V}_D = \frac{-\kappa}{\mu} \nabla p \quad (1.12)$$

where \vec{V}_D is the flow rate per unit area of the cross section, ∇p is pressure gradient. We can get the fluid velocity V_P through the pores by the following:

$$\vec{V}_P = \frac{\vec{V}_D}{\phi} \quad (1.13)$$

1.2.3.2 Kozeny-Carman equation

Kozeny-Carman equation is used to predict the flow rate through porous media such as filter beds and fluidized beds [14]. It is obtained on the basis that flow is laminar and expressed as:

$$\frac{\Delta p}{L} = \frac{180\mu (1 - \phi)^2}{\Phi_s^2 D_p^2 \phi^3} V_D \quad (1.14)$$

where Φ_s is the sphericity of the particles and $\Phi_s = 1$ for a sphere, which is the measure of how closely the shape of a particle approaches a perfect sphere. D_p is the diameter of the related spherical particle. We product A at both sides of Eq 1.14 and get:

$$\frac{\Delta P}{L} A = \frac{180\mu (1 - \phi)^2}{\Phi_s^2 D_p^2 \phi^3} Q \quad (1.15)$$

$$Q = \Gamma \cdot \frac{\Delta P}{L} A \cdot \frac{\phi^3}{(1 - \phi)^2} \quad (1.16)$$

for the fixed fluid and porous media, $\Gamma = \frac{\Phi_s^2 D_p^2}{180\mu}$ is constant. By combining with the Eq 1.10, the link between porosity and permeability is created as follows:

$$\Gamma \cdot \frac{\phi^3}{(1 - \phi)^2} = \frac{-\kappa}{\mu} \quad (1.17)$$

Darcy's law and Kozeny-Carman equation are used to describe the flow of fluid through porous media. In order to obtain detailed information about the flow field associated with the porous medium, the solution of flow field in porous media need to be determined.

1.2.3.3 Kuwabara solution

In porous media, the flow field determination is generally difficult and problem must be solved numerically. Nevertheless, in some relatively simple configurations, it can be solved analytically. For example, we can introduce an analytical solution of Stokes equation based on stream function expressed as:

$$\nabla^4 \Psi(r, \theta) = 0 \quad (1.18)$$

and the general solution of Stokes equation finally can be given as follows [36]:

$$\begin{aligned} \Psi(r, \theta) = & a_0 + b_0 \ln(r) + c_0 r^2 + d_0 r^2 \ln(r) \\ & + (a_1 r^{-1} + b_1 r \ln(r) + c_1 r + d_1 r^3) \sin(\theta) + (a'_1 r^{-1} + b'_1 r \ln(r) + c'_1 r + d'_1 r^3) \cos(\theta) \\ & + \sum_{n=2}^{\infty} (a_n r^{-n} + b_n r^{-n+2} + c_n r^n + d_n r^{n+2}) \sin(n\theta) \\ & + \sum_{n=2}^{\infty} (a'_n r^{-n} + b'_n r^{-n+2} + c'_n r^n + d'_n r^{n+2}) \cos(n\theta) \end{aligned} \quad (1.19)$$

where $a_0, b_0, c_0, d_0, a_1, b_1, c_1, d_1, a'_1, b'_1, c'_1, d'_1, a_n, b_n, c_n, d_n, a'_n, b'_n, c'_n, d'_n$ are coefficients.

The components of velocity are satisfied and calculated using the following relationships:

$$V_r = \frac{\partial \Psi}{r \partial \theta} \quad (1.20)$$

$$V_\theta = -\frac{\partial \Psi}{\partial r} \quad (1.21)$$

The symmetry condition:

$$\begin{cases} \Psi(r, \theta) = -\Psi(r, -\theta) \\ \Psi(r, \theta) = \Psi(r, \pi - \theta) \end{cases} \quad (1.22)$$

These conditions lead to the following relations:

$$\begin{cases} a_0 = b_0 = c_0 = d_0 = 0 \\ a'_1 = b'_1 = c'_1 = d'_1 = 0 \\ a'_n = b'_n = c'_n = d'_n = 0 \end{cases} \quad (1.23)$$

and the coefficients of the even term of the $\sin(n\theta)$ are zero, we use $2n$ instead of n

$$a_{2n} = b_{2n} = c_{2n} = d_{2n} = 0 \quad (1.24)$$

Therefore, the expression of the streamfunction and the velocity are:

$$\begin{aligned} \Psi(r, \theta) = & (a_1 r^{-1} + b_1 r \ln(r) + c_1 r + d_1 r^3) \sin(\theta) + \\ & \sum_{n=2,3,\dots}^{\infty} (a_{2n-1} r^{-2n+1} + b_{2n-1} r^{-2n+3} + c_{2n-1} r^{2n-1} + d_{2n-1} r^{2n+1}) \sin((2n-1)\theta) \end{aligned} \quad (1.25)$$

$$\begin{aligned}
 V_r &= (a_1 r^{-2} + b_1 \ln(r) + c_1 + d_1 r^2) \cos(\theta) + \\
 &\quad \sum_{n=2,3,\dots}^{\infty} [(a_{2n-1} r^{-2n} + b_{2n-1} r^{-2n+2} + c_{2n-1} r^{2n-2} + d_{2n-1} r^{2n}) (2n-1)] \cos((2n-1)\theta) \\
 V_\theta &= (-a_1 r^{-2} + b_1 \ln(r) + b_1 + c_1 + 3d_1 r^2) \sin(\theta) - \\
 &\quad \sum_{n=2,3,\dots}^{\infty} [(-2n+1)a_{2n-1} r^{-2n} + (-2n+3)b_{2n-1} r^{-2n+2} + \\
 &\quad (2n-1)c_{2n-1} r^{2n-2} + (2n+1)d_{2n-1} r^{2n}] \sin((2n-1)\theta)
 \end{aligned} \tag{1.26}$$

For the boundary condition of the streamfunction, we use the Kuwabara model [37, 38] in which the boundary is a cylindrical outer boundary as shown in Fig.1.5 (b). A series of periodic arrangement of cylinders with a square unit is shown in Fig.1.5 (a).

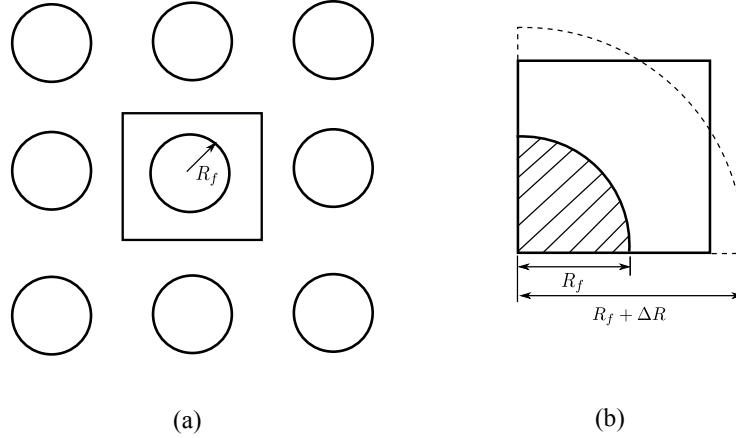


Figure 1.5: (a) Cylinders with square unit cell. (b) Solution domain for exact solutions of streamfunction.

At the surface of the fiber, we have:

$$v_r = v_\theta = 0, \quad \text{at } r = R_f \tag{1.27}$$

For the outer boundary condition, Kuwabara uses

$$v_r = \cos \theta \quad \text{and} \quad \xi = 0, \quad \text{at } r = R_f + \Delta R \tag{1.28}$$

where ξ is the vorticity, then Kuwabara's solution is

$$\Psi_K(r, \theta) = R_f [C_1 \left(\frac{r}{R_f}\right)^3 + C_2 \frac{r}{R_f} + C_3 \frac{R_f}{r} + C_4 r \ln\left(\frac{r}{R_f}\right)] \sin \theta \quad (1.29)$$

where C_1, C_2, C_3, C_4 are the coefficients, which are found using the boundary conditions (1.27)-(1.28)

$$C_4 = -\frac{4}{2 \ln(1 - \phi) - 1 + 4\phi + (1 - \phi)^2} \quad (1.30)$$

$$C_1 = -\frac{C_4(1 - \phi)}{4} \quad (1.31)$$

$$C_3 = C_1 + \frac{C_4}{2} \quad (1.32)$$

$$C_2 = -C_1 - C_3 \quad (1.33)$$

where ϕ is the porosity, for the circular unit it is given by:

$$\phi = 1 - \left(\frac{R_f}{(R + \Delta R)}\right)^2 \quad (1.34)$$

The Kuwabara's solution is known, then the fluid velocity field can be calculated in such simple configurations.

1.3 Filtration

1.3.1 Filtration type

Filtration is commonly used to describe the deposition and transport of particles from fluid suspension through a porous medium. Particle separation from the fluid requires a high efficiency filtration system. In terms of filtration process, variety of filtration type exists, they can be classified into cake filtration, granular filtration, fibrous filtration [39].

Cake filtration

Cake filtration for particle separation is often carried out in several stages such as cake formation and growth [39]. A filter cake is formed by the solid particles that are retained on the surface of filter medium as shown in Fig.1.6. At the initial stage of cake filtration, the smaller particles can penetrate into the filter layer. In the subsequent filtration process,

the accumulation of these particles gradually leads to the increase of the thickness of the cake, then smaller particles deposit within the porous cake formed by the large particles [40, 41]. Finally it allows only the passage of the suspending fluid.

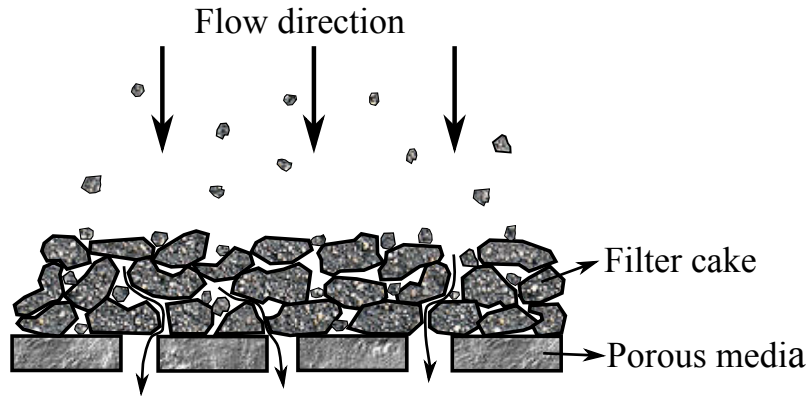


Figure 1.6: Cake filtration

Granular filtration

Granular filtration is a process that primarily clarifies dilute suspensions using granular media as collected bodies. In granular filtration, two solid phases are included: one is the granular media through which the fluid flows, and the other solid phase comprises particles that are suspended in the fluid phase [42]. Granular porous media initially are free of particles, they can accumulate deposits by removing particles from suspension (see Fig.1.7) [43]. For granular filtration, particle deposition takes place throughout the entire filter medium.

Fibrous filtration

Fibrous filtration refers to the process in which the removal of particles from fluid pass through fibrous media. In terms of the constituted filter media, particle retention occurs in the form of filter cake either throughout the medium or at the surface of the medium. If the medium is formed by packing fibers loosely such as those applied in air-condition, particle retention mostly happens within the interior of the medium [14]. This kind of fibrous filtration is similar to granular filtration. Generally speaking, a fibrous filter medium comprise nature and synthetic materials for use in both gas and liquid application. Fig.1.8 presents fibrous filtration process where particles are collected at the surface of the fibers.

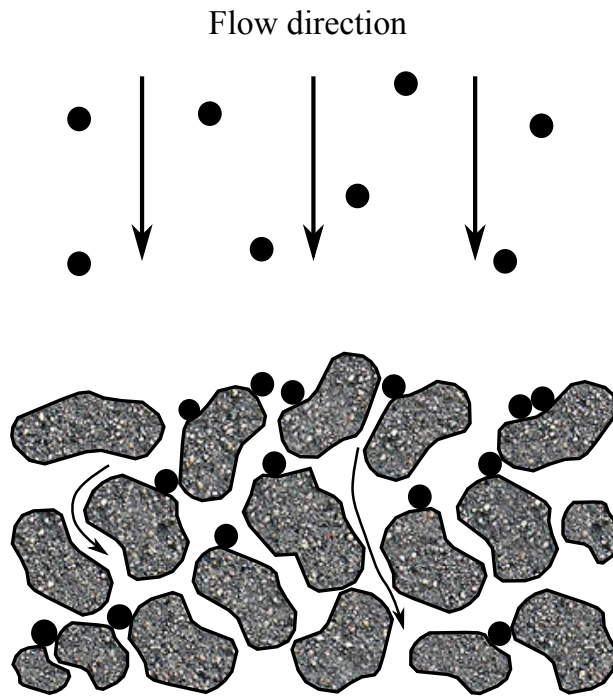


Figure 1.7: Schematic view of granular filtration [43]

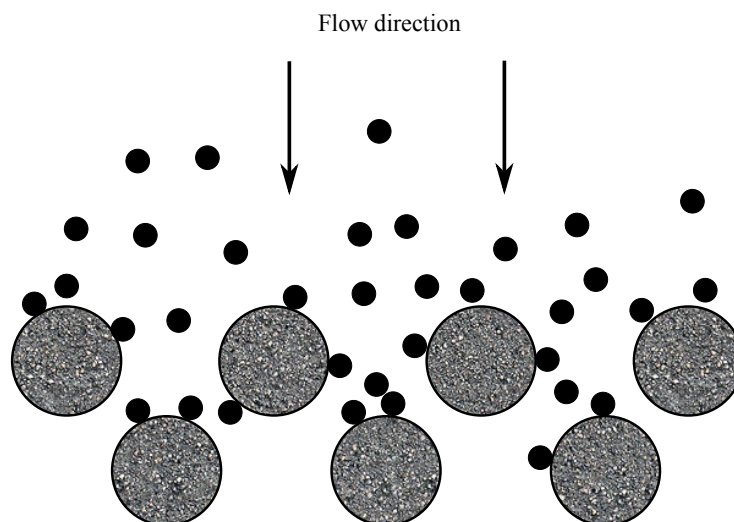


Figure 1.8: Schematic view of fibrous filter

1.3.2 Quality factor

In several decade years, many researchers have focused on the study of particle filtration process [38, 44, 45, 46]. The filter composed of fibers is used to remove the particle from the fluid, thus the filter performance need to be estimated in order to ensure the long term use of filter. A best-performing filter first of all not only assures a high filtration efficiency of filter η but also maintains a low pressure drop Δp . The detailed of the parameters is presented in the next section. In order to judge the performance of filter, the definition of quality factor (or the figure of merit), which is an indicator of the ratio of penetration rate P ($P = 1 - \eta$) to the pressure drop, is expressed as [11]:

$$QF = \frac{-\ln(P)}{\Delta p} \quad (1.35)$$

From the filter quality factor standpoint, the larger value of quality factor QF indicates a better quality of fibrous filter.

1.3.3 Filtration efficiency

The deposition of particles on the surface of filter medium can modify the pore morphology. The accumulation of the particles leads to the filter clogging. As a consequence, the permeability declines and pressure drop increases which damage filter life. Thus, it is essential to quantitatively estimate a filter performance. A filter is generally composed of a number of unit bed elements (UBE) connected in series. The UBE consists of several individual collectors with some simple geometry such as a capillary, sphere or constricted tube as depicted in Fig.1.9. Generally, a filter performance is described by its overall efficiency, which is deduced from the efficiency of UBE by simple association formula, that will be introduced hereafter.

Here we use circular circle to represent fiber in filter as shown in Fig.1.10. The filtration efficiency of a filter η is depicted in Fig.1.10 (a) and defined as [14]:

$$\eta = \frac{c_{in} - c_{eff}}{c_{in}} \quad (1.36)$$

where c_{in} and c_{eff} denote the influent and effluent particle concentrations, respectively. A filter generally includes a number of UBEs, the efficiency of the i th UBE is illustrated in Fig.1.10 (b) and given:

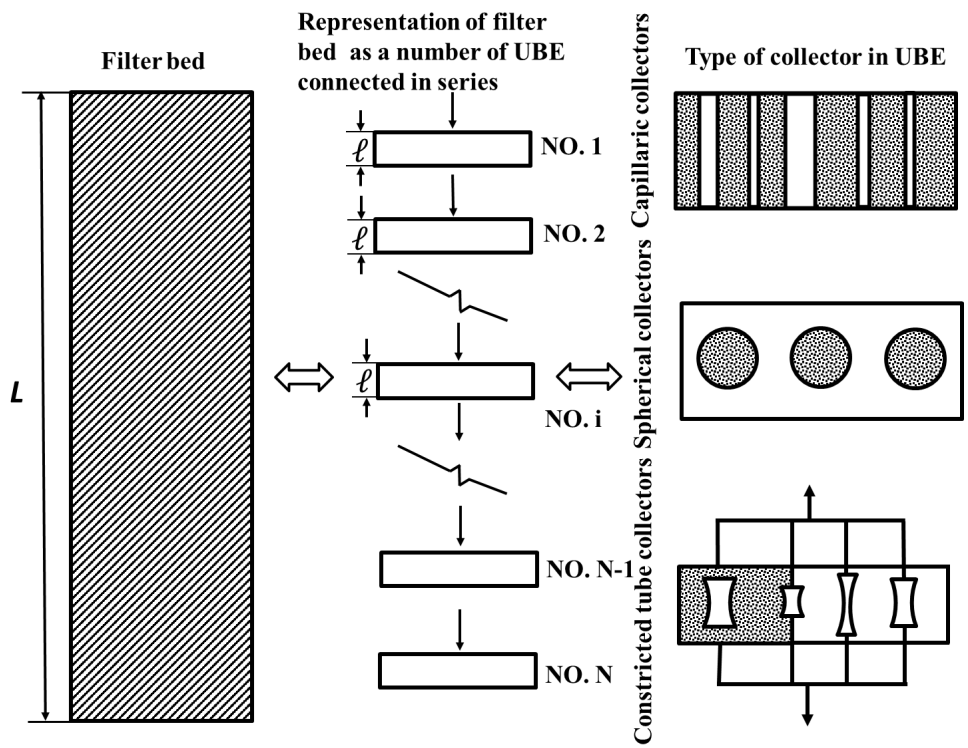


Figure 1.9: Schematic representation of filter [14]

$$e_i = \frac{c_{i-1} - c_i}{c_{i-1}} \quad (1.37)$$

where c_i represents the particle concentration of the suspension exiting the i th unit collector. The efficiency of UBE is dependent on both individual collector efficiency and arrangement of porous media. The individual collector efficiency corresponds to the fraction of particles encountering the collector. It is not only relative to the nature and mechanism of the transport of particle from the suspension to the collector surface and adhesion of the particles to the collector surface, but also to the flow field around the individual collector. Finally, the filtration efficiency can be expressed in terms of efficiency of UBE :

$$\eta = 1 - \prod_{i=1}^N (1 - e_i) \quad (1.38)$$

where N is total number of UBEs connected in series, \prod is the symbol of product.

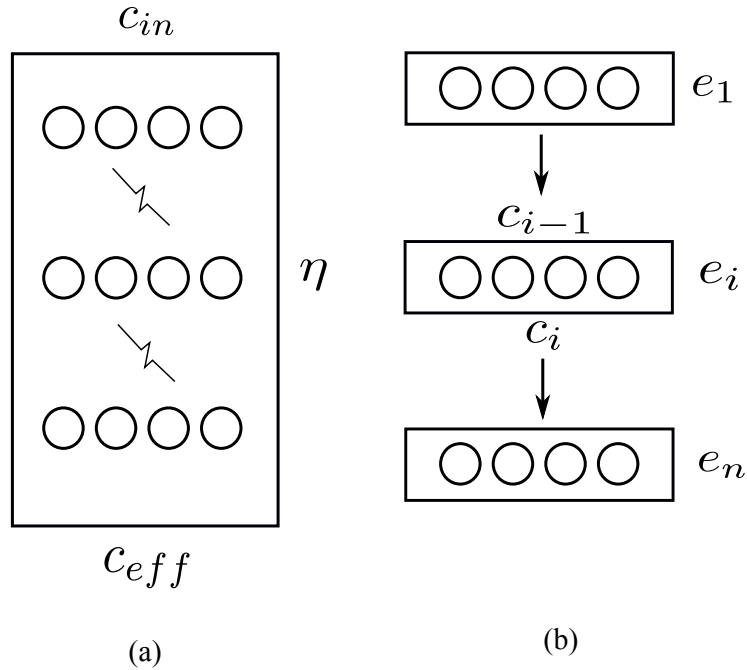


Figure 1.10: Filtration efficiency of filter (a) and efficiency of UBE (b)

1.3.4 Single fiber capture efficiency

The flow of particles through porous media is a very complex phenomenon due to the diversity of the mechanisms involved [33]. A number of factors are responsible for particle

transport. As a transported solid particle approaches a fiber, the particle deposits on the surface of fiber by simultaneous action of several mechanisms, such as Brownian diffusion, interception and inertial impaction [47]. The filtration efficiency η of clean filter medium is closely linked to single fiber capture efficiency η_s . Single fiber capture efficiency is defined as [48]:

$$\eta_s = \frac{\text{number of particles captured by fiber}}{\text{number of particles in the volume geometrically swept out by fiber}} \quad (1.39)$$

It is based on mass balance on a filter element of thickness dl and integrated on the total filter thickness L . Then the relationship of total filtration efficiency and single fiber capture efficiency is [49]:

$$\eta = 1 - \exp \left[-\frac{4\beta\eta_s L}{\pi(1-\beta)D_f} \right] \quad (1.40)$$

where β is the solid volume fraction occupied by the fibers. D_f is the fiber diameter.

Single fiber capture efficiency is related to collision efficiency and adhesion probability [44]. Collision efficiency of fiber η_c is the ratio of number of particle collided with fiber to the number of particles entering the project area of fiber. The relation ship between the single fiber capture efficiency η_s and collision efficiency η_c can be expressed:

$$\eta_s = \eta_c j \quad (1.41)$$

where j is adhesion probability specifying the fraction of particles adhered on the fiber with respect to the total number of particles contacting with it. In this work, the adhesion probability $j = 1$, so the single fiber capture efficiency is simply taken equal to the collision efficiency.

The single fiber capture efficiency η_s depends on the capture mechanism involved in filtration process. The mechanical single fiber capture efficiency is expressed as [50]:

$$\eta_s = 1 - (1 - \eta_D)(1 - \eta_R)(1 - \eta_I) \quad (1.42)$$

where η_D is capture efficiency due to Brownian diffusion, η_R is efficiency due to interception, η_I is capture efficiency due to inertial impaction. For a particular range of particle size, generally one mechanism is dominant, the terms in Eq (1.42) $\eta_D\eta_R$, $\eta_D\eta_I$, $\eta_R\eta_I$ and $\eta_R\eta_D\eta_I$ are neglected. Thus the single fiber capture efficiency can be calculated as:

$$\eta_s = \eta_D + \eta_R + \eta_I \quad (1.43)$$

For the purpose of better understanding the meaning and physical significance of mechanisms, we will now examine the particle behavior individually and present the three mechanisms.

1.3.5 Capture mechanism

1.3.5.1 Brownian diffusion

In diffusion, particles transport from a higher concentration to a lower concentration, whereas in Brownian diffusion, particle suspended in a fluid transports irregularly due to the collisions with the surrounding particles. Brownian diffusion is one of the basic particle capture mechanisms [51]. The influence of the Brownian diffusion force on particle deposition is significant for the submicrometer particles [14]. Brownian diffusion is the dominant factor when particle size is generally smaller than $0.1 \mu\text{m}$ [47] for the deposition in a filter medium. The Brownian force is usually taken into account for analyzing the trajectories of small particles. Fig.1.11 illustrates the particle trajectory subject to capture by Brownian diffusion. The Brownian motion is strong enough to move particle from the original streamlines to the surface of a fiber. This contribution increases as the particle size decreases.

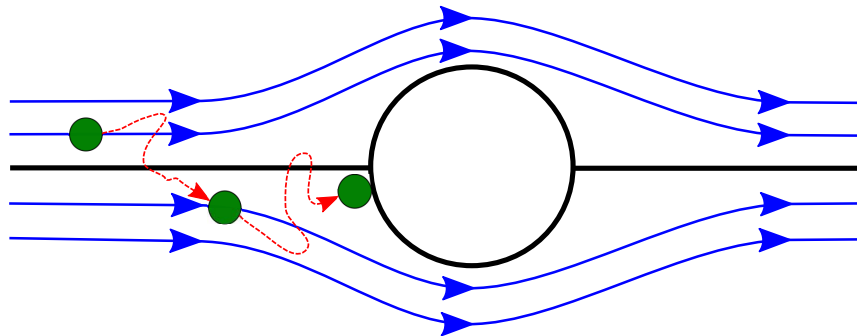


Figure 1.11: Particle capture by Brownian diffusion

The particle capture corresponding to Brownian diffusion is related to the dimensionless number called Péclet number Pe , which is the ratio of advective transport of particles to their Brownian transport (or random transport of particles) near a fiber surface [52]. The Péclet number provides an indication of the relative importance of diffusion and convection

[53]. The Péclet number is:

$$Pe = \frac{UD_f}{D} \quad (1.44)$$

where U is flow velocity, D_f is fiber diameter and D is Brownian diffusion coefficient defined as:

$$D = \frac{k_B T C_u}{3\pi\mu d_p} \quad (1.45)$$

where k_B is the Boltzmann constant and T is the temperature. μ and d_p are the fluid dynamic viscosity and particle diameter. C_u is the Cunningham coefficient (or slip correction factor) related to the particle diameter d_p and mean free path of gas molecules λ given by [54]:

$$C_u = 1 + \frac{2\lambda}{d_p} \left[1.257 + 0.4 \exp\left(-0.55 \frac{d_p}{\lambda}\right) \right] \quad (1.46)$$

When the Brownian diffusion is the dominant capture mechanism for small particles, the single fiber capture efficiency is approximately equal to diffusion capture efficiency η_D . In some articles, a number of theoretical formulas for capture efficiency due to Brownian diffusion are developed. Stechkina (1966) [55] dealt with filter model consisting of a system of parallel circular cylinders and proposed a diffusion equation based on the boundary layer analysis:

$$\eta_D = 2.9K_u^{-1/3}Pe^{-2/3} + 0.624Pe^{-1} \quad (1.47)$$

where K_u is the hydrodynamic factor of Kuwabara's flow [10, 37] and is equal to:

$$K_u = -\frac{1}{2} \ln \beta - 0.75 + \beta - \frac{1}{4}\beta^2 \quad (1.48)$$

where β is the volume fraction occupied by the solid.

For submicron particles, which have a low diffusion coefficient and a large Péclet number, Lee and Liu (1982) [56] presented an analysis of the convective Brownian diffusion equation to determine the capture efficiency:

$$\eta_D = 2.6 \left(\frac{1-\beta}{K_u} \right)^{1/3} Pe^{-2/3} \quad (1.49)$$

Eq 1.49 used the Kuwabara's flow field to consider the interference effects between the

neighboring fibers, however, this equation does not account for the effect of slip at the gas-fiber interface [57].

For nanoparticles, which have a small Péclet number (Pe is of the order of unit), Wang et al. [53] developed an empirical power law model for diffusion capture efficiency depending on Pe , they gave the following empirical equation:

$$\eta_D = 0.84Pe^{-0.43} \quad (1.50)$$

Eq 1.50 agreed well with experimental data. It is noticed that the power of Pe is -0.43 not $-2/3$ as in eq 1.49, indicating lower dependence of capture efficiency on Pe .

1.3.5.2 Interception

The second basic capture mechanism is interception in the filtration process. Some particles deposited on the surface of a fiber are the result of interception. Particle size is generally larger than $0.1 \mu\text{m}$ for interception mechanism [47]. In this size range, particles are assumed to have the same mass as fluid particles and follow the fluid streamlines [58]. Interception takes place when the distance between the center of a particle and surface of a fiber is equal to or less than the particle radius, even if particle remains on the corresponding streamline [57]. Fig.1.12 illustrates particle capture by the fiber due to interception effect.

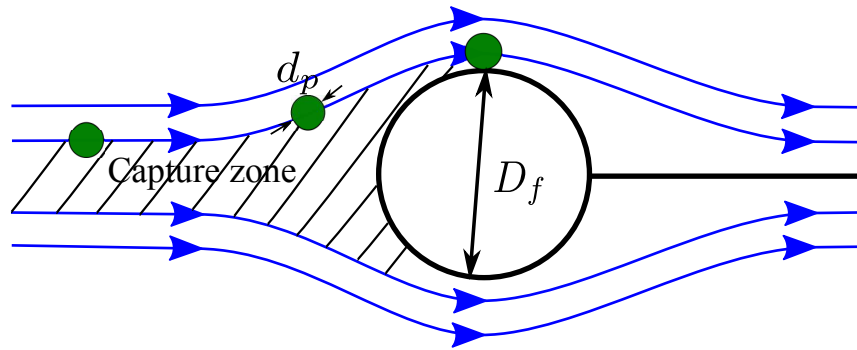


Figure 1.12: Particle capture by interception

For each size fiber, there exists a specified region as shown in Fig.1.12 (capture zone), within which all the particles are captured by the fiber in the fluid flow. Outside of this region, particles are not deposited on the fiber and flow out from the filter. The interception efficiency of single fiber due to the interception mechanism depends on intercept coefficient R , which is defined as the ratio of particle diameter to fiber diameter as follows:

$$R = \frac{d_p}{D_f} \quad (1.51)$$

Some investigators provided a number of empirical relations to calculate the interception efficiency. A complete expression for the interception efficiency of single fiber η_R is obtained from the Kuwabara's solution [37]. This complete expression is [56]:

$$\eta_R = \frac{1+R}{2K_u} \left[2 \ln(1+R) - 1 + \frac{1}{(1+R)^2} \left(1 - \frac{\beta}{2} \right) - \frac{\beta}{2} (1+R)^2 \right] \quad (1.52)$$

Interception is a capture mechanism between diffusion and inertial impaction regime. However, it is common to observe that interception exists with other capture mechanisms at the same time in fluid flow. For the capture efficiency via simultaneous action of diffusion and interception, one of the simplest way is considering these two mechanisms together to obtain single fiber capture efficiency. Lee and Liu [56] provided a final equation to calculate capture efficiency for diffusion and interception.

$$\eta_{DR} = 2.6 \left(\frac{1-\beta}{K_u} \right)^{1/3} Pe^{-2/3} + \left(\frac{1-\beta}{K_u} \right) \frac{R^2}{1+R} \quad (1.53)$$

When using the Eq.(1.53), one assumption is that particle is mainly dominated by one mechanism (interception or diffusion), the contribution from the other mechanisms is small.

1.3.5.3 Inertial impaction

One of the major capture mechanisms in filtration process is inertial impaction in the absence of external force such as electrostatic force and gravitational force [59]. Particle departs from streamlines when it is transported in fluid. When it is close to the fiber, fluid streamlines start to change direction. However, particle trajectory is different from fluid streamlines near to a fiber. Due to inertia, it is unable to adjust to the abrupt changes from corresponding streamlines, then inertial impaction occurs. This mechanism can be observed for particle size greater than $1 \mu\text{m}$ [14, 60]. Fig.1.13 illustrates that the particle is captured due to inertial impaction.

Some of particle trajectories deviate from the fluid streamlines due to their inertia and may intersect with the fiber surface. This intersection leads to the particle deposition. Inertial impaction is governed by the dimensionless parameter Stokes number (St) which characterized the behavior of particles suspended in fluid flow. The Stokes number can be viewed as the ratio of the characteristic time of particle to the characteristic flow time

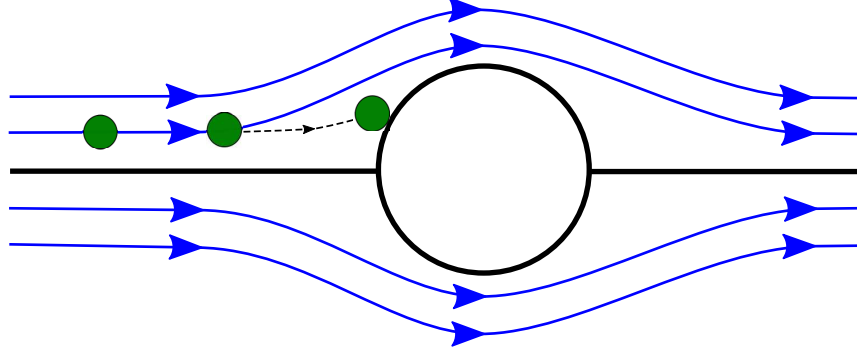


Figure 1.13: Schematic representation of particle capture by inertial impaction

around the fiber [61] and it is given by:

$$St = \frac{\rho_p d_p^2 U}{18\mu D_f} \quad (1.54)$$

where ρ_p is the particle density. This mechanism plays an important role for capture efficiency when the effect of inertial impaction in the filtration regime is significant. Generally, large particle with large St number is easy to be captured by the inertial impaction mechanism [47].

A series of equations used to compute the capture efficiency due to inertial impaction are proposed by some researchers. Landahl and Herrmann (1949) [62] experimentally determined the efficiency due to inertial impaction. Their work resulted in the following correlation for fiber Reynolds number equal to 10:

$$\eta_I = \frac{St^3}{St^3 + 0.77St^2 + 0.22} \quad (1.55)$$

The limitation of eq 1.55 is that it does not predict the capture efficiency for small St .

For small Stokes number, the capture efficiency is given by [63]

$$\eta_I = \frac{StJ}{2K_u} \quad (1.56)$$

where J is a parameter derived in the Kuwabara's flow field,

$$J = (29.6 - 28\beta^{0.62})R^2 - 27.5R^{2.8} \quad (1.57)$$

The Eq 1.56 is valid for $0.01 \leq R \leq 0.4$ and $0.0035 \leq \beta \leq 0.111$.

Brown (1993) [64] considered inertial impaction for circular fiber at large Stokes number

and gave

$$\eta_I = \frac{1 - \zeta}{St} \quad (1.58)$$

where ζ is a constant depending on the flow field. Brown gave $\zeta = 0.805$ for the Kuwabara's flow field with $\beta = 0.05$. It notices that the Eq 1.58 does not take the particle size into account.

In some cases, the inertial impaction and interception exit in the same flow regime. Both of them need to be considered at the same time. Different authors, Stechkina [63] and Davies [65] also proposed different equations to compute the capture efficiency combining the interception and inertial impaction. Schweers et al. (1994) [44] improved the approximation proposed by Suneja and Lee [66] who solved the Navier-Stokes equation to obtain the capture efficiency. The correlation obtained by Schweers et al. is:

$$\eta_{IR} = \left(\frac{St}{St + 0.8} - \frac{2.56 - \log Re - 3.2R}{10\sqrt{St}} \right) (1 + R) \quad (1.59)$$

Eq 1.59 is used under the following conditions: $1 < Re < 60$ and $0 < R < 0.15$.

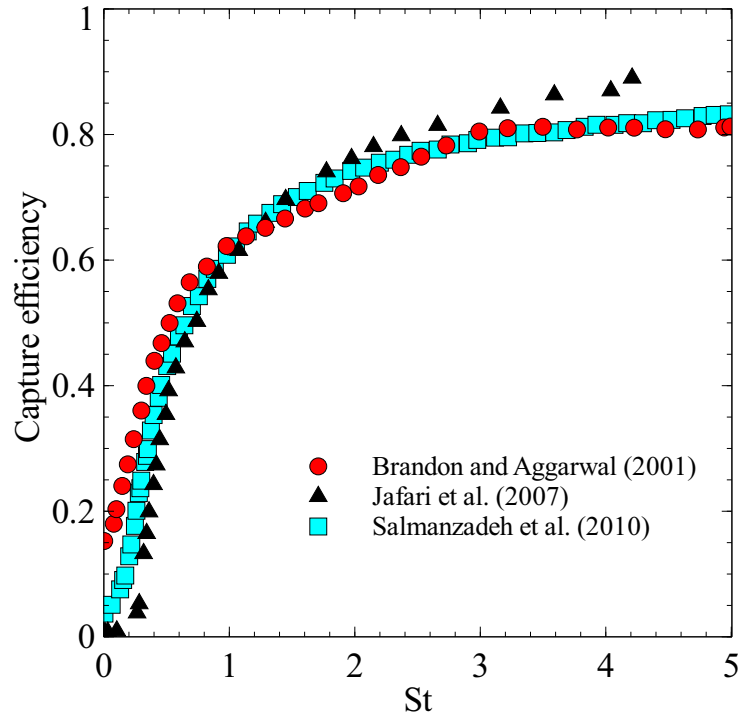


Figure 1.14: Capture efficiency of square block as a function of St

Capture efficiency as a function of Stokes number are examined by several researchers

[67, 68, 69]. Fig.1.14 exhibits an example of capture efficiency on the front of side of a square block placed in a channel as a function of St . This figure indicates that the capture efficiency increases rapidly with the particle Stokes number.

The dependence of filtration efficiency of filter due to different capture mechanisms on the particle diameter is established. As illustrated in Fig.1.15 [70], the decrease in particle diameter enhances the capture efficiency of filter by Brownian diffusion whereas the increase in particle diameter leads to the increase of filtration efficiency of filter by interception and inertial impaction. It is noted that there is a region where diffusion and interception exist at the same time, causing a minimum filtration efficiency of filter. The minimum filtration efficiency of filter will vary depending with the type of filter and flow velocity.

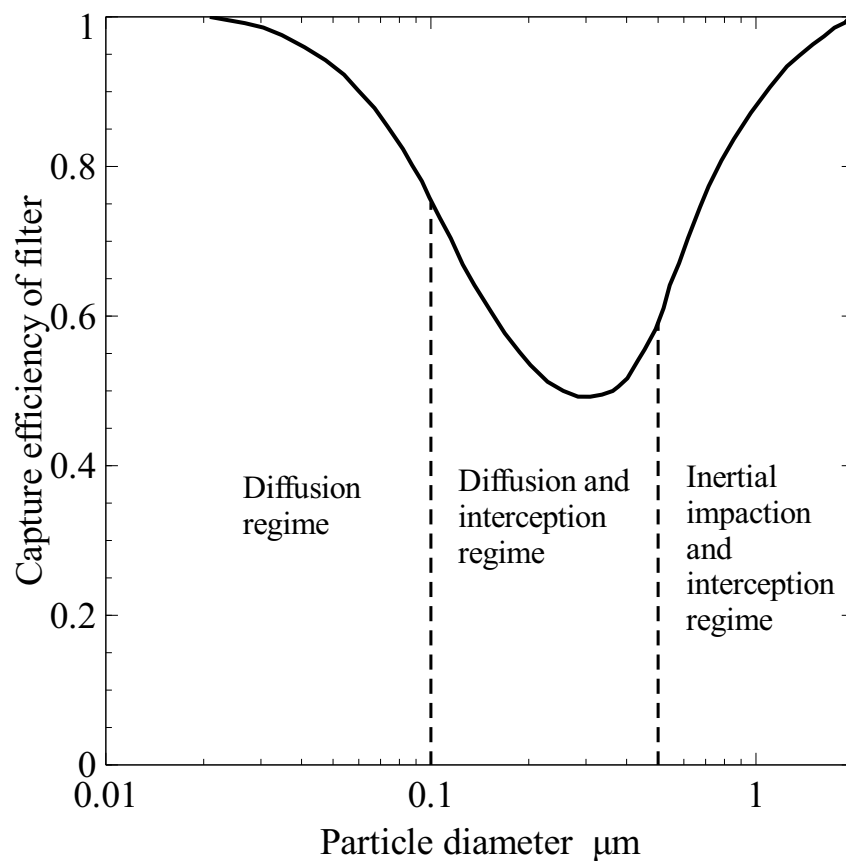


Figure 1.15: Filtration efficiency of filter versus particle diameter illustrating different capture mechanisms [70]

1.3.6 Retention sites

The elementary mechanisms of particles deposition in porous media is described in the following section. Delanchambre [71] defined four retention sites that can limit the particle migration as illustrated in Fig.1.16.

- **Surface sites:** The retention of the particle occurs on the surface of the porous medium (Fig.1.16 a).

- **Crevice sites:** The particle in the suspension is located at the contact line between two convex surface of two grains. The particle can be retained by this mechanical wedging in the crevice (Fig.1.16 b).

- **Constriction sites:** Some pores formed by three convex grains in contact are very frequent in porous medium. When these narrow pores whose dimensions are smaller than those of the suspended particles, the particle stops (Fig.1.16 c).

- **Cavern sites:** Several grains formed a small pocket like the elbows of the pores, the fluid can not penetrate through this cavern so that the transported particle is retained (Fig.1.16 d).

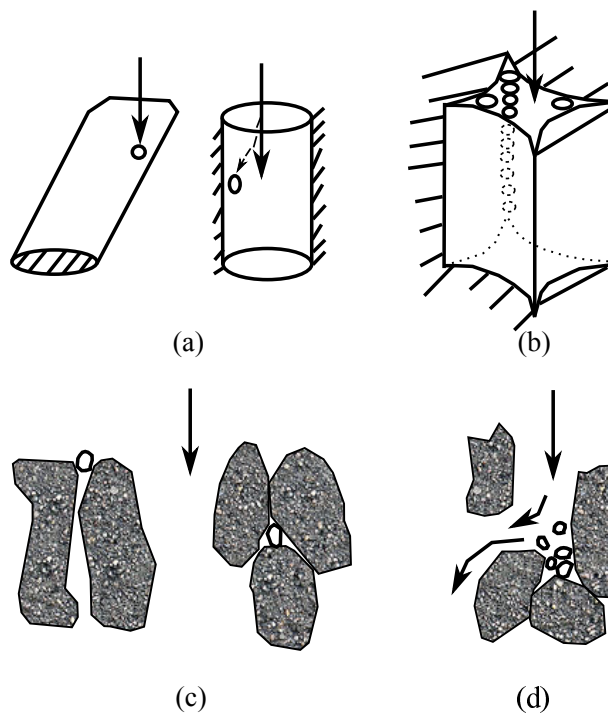


Figure 1.16: Retention sites (a) surface sites, (b) crevice sites, (c) constriction sites (d) cavern sites [71]

1.3.7 Pressure drop across a filter

As explained before, prediction of pressure drop across a filter is a very important part during filtration process. Pressure drop or flow resistance is a critical factor. Large flow resistance can cause the failure of a filter. Pressure drop is used to evaluate the filtration performance. It can be directly evaluated from the fluid flow. It can be expressed in terms of the fluid dynamic viscosity μ , filter thickness L , filtration velocity U and fiber diameter D_f [57] as:

$$\frac{\Delta p}{L} = f \frac{\mu U}{D_f^2} \quad (1.60)$$

where f stands for the pressure drop factor. When the particles accumulates inside a filter, the adhesion of particles to the surface of fiber cause the increase in pressure drop. The problem associated with the pressure drop can be analyzed by estimating the drag force of fiber. A number of theoretical works considering the calculation of pressure drop have been presented. Kuwabara [37] solved Stokes equations to propose a mathematical model for computing the pressure drop factor. The expression is given:

$$f(\beta) = \frac{4\pi}{K_u} \quad (1.61)$$

Davies [72] developed an empirical correlation to estimate the pressure drop factor which is based on a large number of experimental data. This common relation is given as:

$$f(\beta) = 64\beta^{3/2}(1 + 56\beta^3) \quad (1.62)$$

Another empirical expression for predicting pressure drop factor is given by Jackson and James [73]. This expression is based on the three-dimensional media and presented as follows:

$$f(\beta) = \frac{20\beta}{3(-\ln \beta - 0.931)} \quad (1.63)$$

The above mentioned correlations demonstrate that pressure drop factor just depend on the solid volume fraction β . Liu and Wang [58] presented a relation where pressure drop factor can be expressed as a function of Reynolds number Re , solid volume fraction β , Knudsen number Kn and ratio of horizontal to vertical distance between fibers $\frac{l}{h}$. The relation of pressure drop factor in multi-fibrous filters can be mathematically sumerized as:

$$f = W \left(Re, \beta, Kn, \frac{l}{h} \right) \quad (1.64)$$

Knudsen number is used to measure the degree of rarefaction in fluid flow and defined as $Kn = 2\lambda/D_f$. It is noticed that the effect of Knudsen number on the pressure drop factor can be neglected for small value of Kn according to literature [72]. Based on the filtration efficiency of filter and pressure drop presented above, then we can calculate the quality factor defined in section 1.3.2.

1.4 Numerical modeling for fluid-particle flows

The fluid-particle flow plays an important role in experiment and industrial process of particle filtration, it is essential to understand the phenomenon of particle transport in fluid flow and the relative physical problems. Because the cost of experiments can be excessive and some information can not be easy to obtain experimentally, numerical simulation of fluid-particle flow provides a promising way to deal with this kind of issues. In recent years, researchers of this field have developed fluid-particle flow models such as one-way coupling, two-way coupling and four-way coupling [74, 75, 76]. One-way coupling means the fluid phase and solid phase are computed separately, only considering the drag force acting on the particles. Two-way coupling means that the back effect of solid phase on the fluid phase is taken into account. Four-way coupling considers the fluid-particle and particle-particle interactions.

The fluid-particle flow models have gradually popularized from one-way coupling to two-way coupling and four-way coupling. In terms of volume fraction of particles Φ_p , Fig.1.17 displays the range of applicability of the different computational approach [74].

For a low value of $\Phi_p \leq 10^{-6}$, the effect of particle on the fluid can be neglected, thus one-way coupling could be sufficient. In the second regime $10^{-6} < \Phi_p \leq 10^{-3}$, the mutual interaction between the fluid and particle need to be considered: two-way coupling. As increased in the volume fraction of particle $\Phi_p > 10^{-3}$, both the fluid-particle interaction and particle-particle interaction should be included, four-way coupling is needed.

In this section, different types of numerical models for simulating the particle transport in fluid flow are outlined. It includes the numerical methods for fluid phase and particle phase respectively.

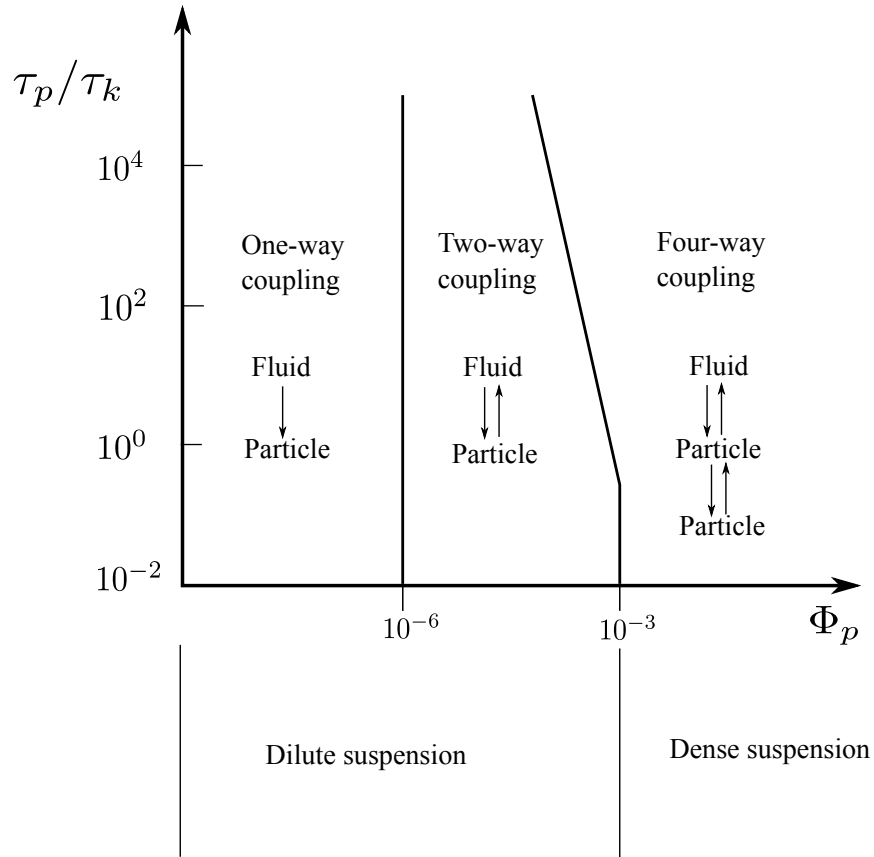


Figure 1.17: Map of flow regimes in particle-laden flows [74], Φ_p : volume fraction of particles, $\Phi_p = NV_p/V$, N : number of particles, V_p : volume of a single particles, V : volume occupied by particles and fluid, d_p : diameter of particle, τ_p : particle response time $= \rho_p d_p^2 / (18 \rho_f \nu)$ for Stokes flow, τ_k : Kolmogorov time scale $= (\nu/\epsilon)^{1/2}$, where ρ_p and ρ_f are particle and fluid density, ϵ is the dissipation rate of turbulence kinetic energy, Stokes number is $St = \tau_p/\tau_k$.

1.4.1 Numerical methods for fluid phase

The problem of fluid-solid firstly requires the selection of a velocity field. Computational Fluid Dynamics (CFD) uses the numerical methods and algorithms to model and analyze the problem of fluid mechanics. In order to solve this kind of problem, Navier-Stokes equation is usually solved using different numerical methods such as Finite Element Method (FEM) [77, 78], Finite Volume Method (FVM) [79, 80], Finite Difference Method (FDM) [81], Smoothed Particle Hydrodynamics (SPH) [82, 83, 84] and Lattice Boltzmann Method (LBM) [85, 86, 87, 88].

The fluid dynamics problems are solved by traditional numerical method FEM, FVM, FDM. The common feature of these methods is that they divide a domain into several elements using structured or unstructured mesh. Then it reconnects elements at nodes as if nodes were pins or drops of glue that hold elements together. They are stable and give very good precision to the problems of the fluid dynamics . However, for some types of problems, these methods are suited poorly. Problems in question are especially those with an extreme deformation as a moving boundary. The complications arising while solving these problems result from the use of a mesh [89].

Smoothed particle hydrodynamic is a Lagrangian method where the numerical results can be achieved without mesh [82]. It is originally designed to use in astrophysical applications. In SPH, the studied domain for fluid field is discretized in particles. These particles interact with each other and move while carrying a set of physical properties of the medium. An advantage of SPH is that it allows boundaries to move or deform as modeling the interaction of several fluid phases bound by a free surface. Therefore, SPH is commonly used to analyze high deformation events and to involve the bodies moving problems in fluids [84]. According to literature [82], errors obtained by SPH can sometimes be larger than those obtained using grid-based methods. Moreover, SPH can be more time consuming than alternative techniques for a given application.

The LBM method is an approach based on the Boltzmann equation which describes the evolution of a fluid. LBM is different from the conventional numerical method, i.e. FEM and FVM, which solve the macroscopic Navier-Stokes equation. It uses a kinetic equation model and corresponding relations between the real simulated statistical dynamic at microscopic level and transport equation at the macroscopic level [90]. It describes fluid phase from the mesoscopic perspective in principle. The detail of principle of LBM will be introduced in chapter 2. Breuer [79] makes a comparison of results obtained using LBM and FVM by simulating confined flow around a square mounted inside a plane channel. The

agreement between LBM and FVM simulation results is excellent by comparing the profiles of streamwise velocity and cross-stream velocity. As literature stated [79], FVM is more efficient for simple geometries whereas LBM is advantageous for highly complex geometries such as those happening in porous media. Beside this, LBM has also its advantage in efficiency, parallel scalability [85].

1.4.2 Numerical methods for solid phase

An analysis of transport of particles in fluid flow needs a through understanding of both flows and particles. It is important to know the information of trajectory and velocity of each individual particle in fluid flow. Particle-tracking method has been applied to determine trajectory and velocity of particle by solving particle equations of motion. Numerical method such as FEM [91], FVM [92] and Discrete Element Method (DEM) [93, 94] are used to model the particle transport under the effect of various forces.

Conventional continuum methods, such as the FEM and FVM, may be appropriate to describe the behavior of small particles, which the size of particle is much smaller than the mesh size. FEM is flexible enough to treat homogeneous materials and non-linear boundary conditions. Therefore, FEM is mostly used to study mechanics problems of structures and solids. FEM and FVM are not suitable to handle the interface tracking problems, i.e., loss of solids involving the use of very small meshes and requiring a remesh process which takes much computational time. FEM and FVM have limited success in the simulations of particulate flows with a high number of particles, especially in three-dimensional simulations [95].

DEM is one of the generally suitable method for modeling the mechanical behavior of particles. It has grown considerably to become a reliable and powerful research tool for the modeling of grain issue. DEM is based on the concept that individual material elements are considered to be separate and are connected only along their boundaries by appropriate physically based interaction laws [96]. It allows us to study these discrete systems in the presence of physical phenomena at the particle scale. Since DEM can treat the spontaneous particle-particle interactions, it has a broad variety of applications in soil mechanics, granular materials and fluid mechanics [97]. The basic difference between the DEM and continuum-based methods is that the contact patterns between components of the system are continuously changing with the deformation process for the former, but are fixed for the latter [97]. An example of particle contact with DEM is performed by Lominé and Oger [98]. They present experiments and numerical model based on DEM to study

transport properties of particles through porous structure, which access the internal motion of particles and examine the influence of physical parameters on the relevant percolation behavior. The detail of the DEM will be presented in chapter 2.

1.4.3 Choice of numerical method

The numerical treatment of the particle transport problems depend on the size of particle in relation with the grid or mesh size [96]. For small particle size within a grid cell, fluid phase is generally described by the Navier-Stokes equations where FEV and FVM are often used. However for the problems in which the particle size is large more than one grid, LBM can make it particularly suitable for larger sized particles from the computational point of view. Large particles can be accommodated within LBM framework. Another advantage of LBM is the simplicity in the implementation of the algorithm and its capability of modeling problems with complex interior fluid domains. For fluid-particle interactions, DEM has capability to extend to deal with multiphysic issues. Thus, a coupled LBM and particle methods, LBM-DEM, can be implemented. The combined LBM-DEM solution strategy is chosen to simulate the fluid-particle systems with volume fraction of particles in the framework of this thesis.

1.5 Summary of earlier researchers' results for particle filtration

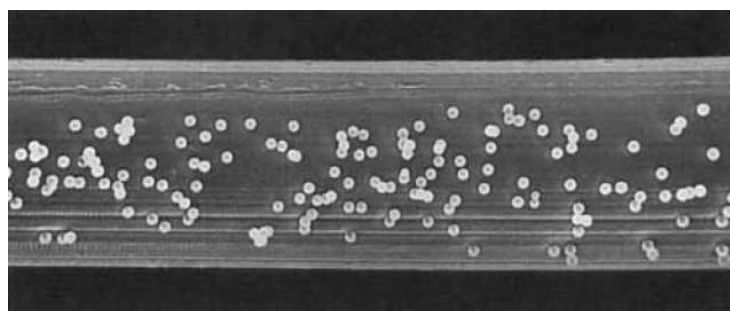
1.5.1 Particle capture on a single fiber

A real filter consists of many individual fibers and its filtration efficiency is heavily dependent on the one of single fiber [59]. Hence, the comprehensive investigation of particle captured by the single fiber is necessary. In order to achieve this, studying the particle deposit on the surface of single fiber is an effective way [99]. In this part, we present particle capture on circular and non-circular fiber.

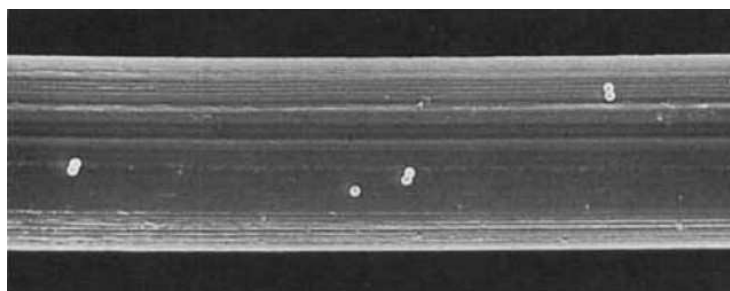
1.5.1.1 Particle capture on circular fiber

Cylindrical fiber with circular cross-section, as one of the most attractive and common shapes, has been widely used to study the filtration process. In early studies, many researches employed theoretical analyses [100], numerical simulations [101, 102] and exper-

imental measurements [103] to examine particle deposition over different obstacles such as cylinders, spheres and disks [104]. Lee and Liu [56] considered a theoretical approach, based on Kuwabara's flow field [37], to predict the filtration of aerosol particles where diffusion and interception are dominant, the fiber capture efficiency calculated from the proposed expression agrees with that of experiment [105]. Schweers et al. [44] determined experimentally the single fiber capture efficiency where the configuration of neighboring fibers was considered. Fig.1.18 displays the particles captured by two consecutively aligned fiber. The most of particle are almost captured by the upper fiber.



(a) upper fiber



(b) lower fiber

Figure 1.18: Scanning electron micrograph (SEM) of particles captured by the fibers [44].

1.5.1.2 Particle capture on non-circular fiber

With the fast development of new instruments for manufacturing technology, the production of non-circular fiber cross-sectional shapes is becoming viable. Researches show great interest for the study of filtration by non-circular fibers [11, 68, 69, 106, 107]. Non-circular fiber have larger specific surface area compared to the circular cross-section fiber with the same volume fraction. Due to this, it is easy to perform higher capture efficiency of particles and to increase mechanical strength, porosity, particle loading capacity for fibers.

Several researches have been dedicated to square or rectangular fibers. Jafari et al. [69] used the square cylinder to numerically investigate the particle deposition and dispersion. The simulation results show that the Brownian diffusion affects the deposition rate of the ultrafine particle on both the front and back sides of the square cylinder.

Brandon and Aggarwal [67] numerically modeled the particle deposition on a square prism in unsteady vertical flows and investigated the effect of Reynolds number on particle trajectory and deposition. They concluded that the Reynolds number has very little effect on the deposition. However, Re has more discernible influence on particle distribution. Zhu et al. [59] numerically and analytically investigated the impaction-dominated filtration process with rectangular fiber for particulate size much smaller than the one of fiber. Influence of fiber aspect ratio, filter volume fraction, particulate size and Stokes number on collection efficiency of a rectangular fiber have been determined for impaction-dominated filtration. The results showed that the efficiency of combined interception and impaction is a parabolic function of Stokes number, the overall size-averaged filtration efficiency is higher than that of median sized particles. Hosseini and Tafreshi [106] investigated the effect of a fiber's cross-section shape on pressure drop and collection efficiency with nanofibers and microfibers. They found that the fiber geometry is more important for pressure drop prediction rather than single fiber capture efficiency estimation. Wang et al. [108] simulated the particle capture process of elliptical fiber. They gave the fitted correction factors which are used to calculate the fiber capture efficiency and pressure drop dominated by Brownian diffusion, interception and inertial impaction respectively. These fit correction factors exhibit reasonable predictions and can be applied in engineering. Huang et al. [109] numerically studied the pressure drop and capture efficiency for diffusional dominant mechanism with rectangular, trilobal, quatrefoil and triangular cross-sections at low Reynolds number. They concluded that the capture efficiency due to diffusion of noncircular fibers is higher than that of the circular fiber with the same volume fraction. The dimensionless force on the noncircular fibers is independent of Reynolds number when $Re < 1$. Wang [110] solved the Stokes flow across an array of rectangular fibers and proposed an empirical formula to calculate the drag of a single square fiber. Fardi and Liu [111] studied the capture efficiency of rectangular fiber dominated by the Brownian diffusion and interception mechanisms. The single fiber capture efficiency due to the pure diffusion and pure interception was found to be proportional to powers of the Peclet number and the interception number, respectively.

1.5.2 Particle transport in filter with multi-fiber

The influence of neighboring filters can affect the deposition pattern on a certain filter. Hence, the filtration process is more complicated than the deposition on a single fiber. The capture efficiency and pressure drop are influenced by the structure of the filter [112]. Understanding particle behavior in filter with multi-fiber is of significant importance for improving the filter performance.

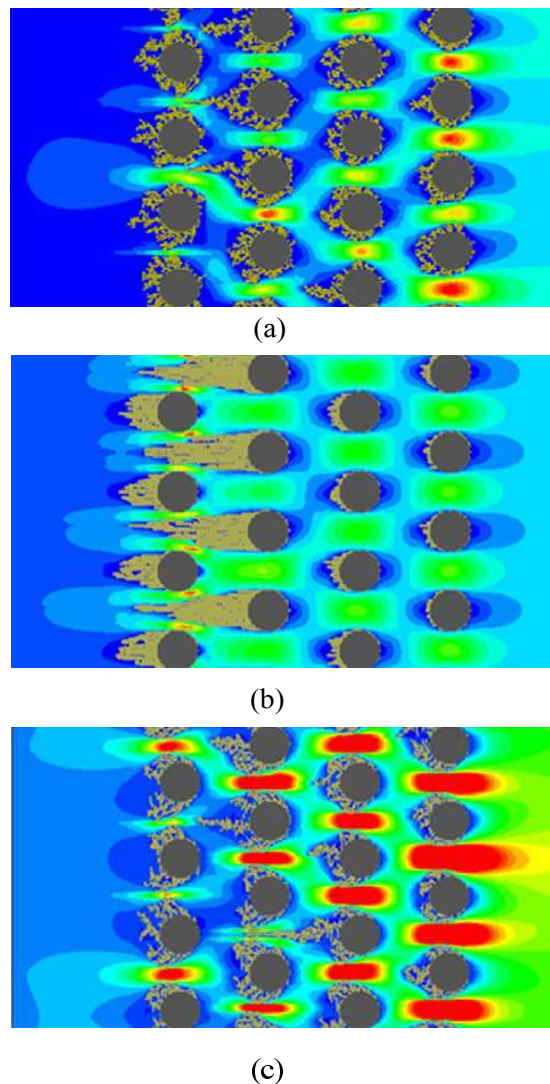


Figure 1.19: Particles captured by different capture mechanisms, (a) diffusion ($Pe = 102$), (b) inertial impaction ($St = 1.61$), (c) interception ($R = 0.0357$) [112].

Liu and Wang [58] analyzed several parameters including volume fraction and fiber

separation ratio during the filtration process. It was found that both the pressure drop and interception efficiency increase with the fiber separation ratio at a given volume fraction. The optimal fiber separation ratio can be used to improve the efficiency and reduce the pressure drop. Wang [112] numerically investigated the pressure drop and filtration efficiency of filter for clean multi-fiber and particle loading multi-fiber cases. It has been found that the staggered model is better than the parallel model from the view of the filtration efficiency and the pressure drop. Fig.1.19 presents particle loading staggered fiber cases with different capture mechanisms.

Ansari et al. [90] investigated and the motion and deposition of particles in the regular and irregular structure filters using the LBM. They found that most of the particles deposited on the first block in the filter for both structures. Fig.1.20 illustrates an example of particle trajectories in the regular and irregular structure filter for $Re = 5$.

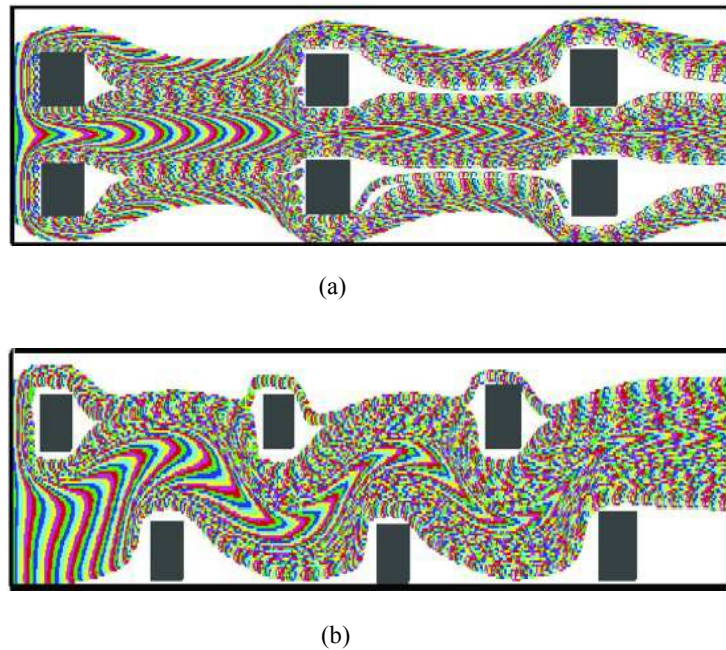


Figure 1.20: Particles trajectories in the regular and irregular structure filter for $Re = 5$ (a) regular structure filter, (b) irregular structure filter, [90].

Lin et al. [113] examined how the obstruction morphology (circular, square and diamond staggered arrayed) affects particle-surface collision efficiency in a free-stream flow. They concluded that the collision of particles on diamond-shaped obstruction is more favorable than that on cylindrical and square obstruction with the presence of vortex-shedding. Fardi and Liu [114] investigated the pressure drop with a staggered array of rectangular

fibers in a viscous fluid flow. The dimensionless drag force on rectangular fiber with aspect ratio > 1 is independent of aspect ratio. However, for fiber aspect ratio ≤ 1 , the dimensionless drag force is a function of both the aspect ratio and fiber solid volume fraction.

1.6 Conclusion

In this chapter, we posed the problem of the particle transport driven by fluid in porous media, which is one of phenomena existing in fluid-solid two-phase flow. This phenomenon involving fluid-particle interactions has been the subject of fluid-solid separation.

Firstly, flow of suspensions through porous medium is presented. Continuity equation and Navier-Stokes equation are often used in fluid flow. The porous media is described such as porosity and characteristic of porous media. For simple configurations of porous media, Kuwabara solution can be used to determine the flow field. Secondly, the knowledge of filtration including filtration type, quality factor, filtration efficiency and pressure drop are reviewed. These important parameters are commonly used in particle filtration process. The relation between filtration efficiency of filter and single fiber capture efficiency is introduced due to three mechanisms (Brownian diffusion, interception and inertial impaction) involved in filtration process. Thirdly, for the purpose of understanding the particle behavior as their transport in porous media, several numerical methods are presented here to simulate fluid and solid phases. LBM has the advantage of simplicity in dealing with the complex boundary condition and in the implementation of the algorithm. DEM has the capability to model problems with a large number of particles. Thus, the coupled LBM-DEM is chosen to investigate the particle transport and deposition in filtration process. Finally, we conclude the earlier researchers' results for particle filtration. Since the single fiber is the fundamental element to constitute a filter, particle capture on circular and non-circular single fiber is reviewed. Then particle transport in filter with multi-fiber is described, where different fiber arrangements are considered.

For particle transport and deposition, it generally refers to fluid-particle and particle-particle interactions. Due to these interactions and different capture mechanisms, they lead to the complexity of particle filtration process. Some details of this process are not well understood. Thus, in order to consider the influence of particle motion on the flow field and particle-particle interactions, we use the coupled LBM-DEM to study the particle filtration process. In the following chapter, we present the detail of the LBM and DEM respectively and a coupling between LBM and DEM. A series of examples are given to valid our code. In

this work, we use the LBM-DEM to investigate the single fiber capture efficiency, filtration efficiency, pressure drop and quality factory of filter. The effect of fiber's cross-sectional shape, fiber arrangement and relative parameters on filtration performance are studied.

Chapter 2

Lattice Boltzmann and Discrete Element methods

2.1 Introduction

Lattice Boltzmann method (LBM) was originally developed from the lattice gas cellular automata (LGCA) [115, 116] used for modeling physics and solving a series of fluid dynamics problems. LBM is based on Boltzmann's equation proposed by Ludwig Boltzmann in 1872. The Boltzmann equation makes it possible to describe the evolution of the distribution function $f(\vec{x}, \vec{c}, t)$, defined as the probability density associated with a particle in the position \vec{x} with a velocity \vec{c} at time t .

$$\frac{\partial f(\vec{x}, \vec{c}, t)}{\partial t} + \vec{c} \cdot \nabla_x f(\vec{x}, \vec{c}, t) + \frac{\vec{F}^{ext}}{m} \cdot \nabla_c f(\vec{x}, \vec{c}, t) = \Omega(f) \quad (2.1)$$

where F^{ext} is the external force acting on the particle in the fluid. The term $\Omega(f)$ represents the variation of the number of particles due to collision in a volume element of the phase space. Chapman and Enskog[117, 118] used a complex collision operator to derive the Navier-Stokes equation from the Boltzmann equation.

The first lattice gas cellular automata model was introduced by Hardy, Pomeau and de Pazzis (called HPP) [119, 120] in 1973. HPP is a two-dimensional model where fluid is located at each lattice node. However, it uses a square lattice with insufficient symmetries to derive Navier-Stokes equation [121]. In 1986, Frisch, Hasslacher and Pomeau (named FHP) [115] proposed a hexagonal lattice. This model based on hexagonal lattice instead of square lattice studied transport properties of fluids. The correct Navier-Stokes

equation was obtained through the lattice gas automata on a hexagonal lattice for first time. FHP creates a new situation for LGCA, which makes it develop rapidly. However, despite the advantages provided by this model, the biggest problems of FHP is noise. By the ends of 1980s, McNamara and Zanetti [122] provided a method to replace the Boolean variables. This method governs the evolution of particle occupancies, in LGCA by calculating the time evolution of a probability density distribution of the particles, the time evolution is controlled by Boltzmann equation. This model, commonly referred to as 'Lattice-Boltzmann', completely eliminated the statistical noise and saved much computer time [123]. The kinetic form of Lattice Boltzmann is still the same as the LGCA and the collision operator has the drawback of complexity. Therefore a lot of work has been investigated to find ways to reduce this complexity. In 1989, Higuere and Jinenez [124] who linearized the collision operator by introducing the equilibrium distribution function simplify the model. Several research groups independently proposed single relaxation time for collision operator making use of a relaxation time towards the local equilibrium [125, 126, 127]. This linear collision operator was introduced by Bhatnagar-Gross-Krook (BGK) [128]. The BGK dramatically reduces the computation cost and gives pretty good results in various applications [86, 96, 129, 130, 131].

Lattice Boltzmann method has a number of characteristics that are different from those of traditional fluid dynamics methods [132]. The conventional numerical methods, such as finite element and finite volume methods, compute flow field by solving the incompressible Navier-Stokes equation. LBM, as an efficient alternative for fluid flow, solves fluid field in terms of density distribution function from the perspective of mesoscopic level. The fluid phase in LBM is considered as fictitious fluid particles which can collide and propagate on a lattice. The macroscopic properties (i.e., pressure, fluid density and velocity) can be obtained through the density distribution functions of fluid particles. Compared with conventional methods, LBM demonstrates significant advantages due to its parallel computation and capability to deal with complex boundary conditions [76]. In the following section, we describe the details for LBM including the principle and implementation of boundary conditions.

2.2 Lattice Boltzmann method

2.2.1 Principle of lattice Boltzmann method

The computational domain in LBM is first divided into a regular lattice with spacing h . The fluid phase in LBM is then assumed as a group of fluid particles which are located at each node of the lattice. They are constrained to migrate along the links between the nearest regular lattices and collide with each other at the grid points. Here, we employ the classical two dimensional D2Q9 model proposed by D'Humières et al.[121]. In the D2Q9 model, a computational domain is discretized using square lattice with nine discrete velocities \vec{e}_i (shown in Fig.2.1). Discrete velocities in the D2Q9 model are defined as:

$$\vec{e}_i = \begin{cases} (0, 0) & (i = 0) \\ C(\cos \frac{\pi(i-1)}{2}, \sin \frac{\pi(i-1)}{2}) & (i = 1, \dots, 4) \\ \sqrt{2}C(\cos \frac{\pi(2i-9)}{4}, \sin \frac{\pi(2i-9)}{4}) & (i = 5, \dots, 8) \end{cases} \quad (2.2)$$

in which C means the lattice speed given by:

$$C = h/dt \quad (2.3)$$

dt is the time step.

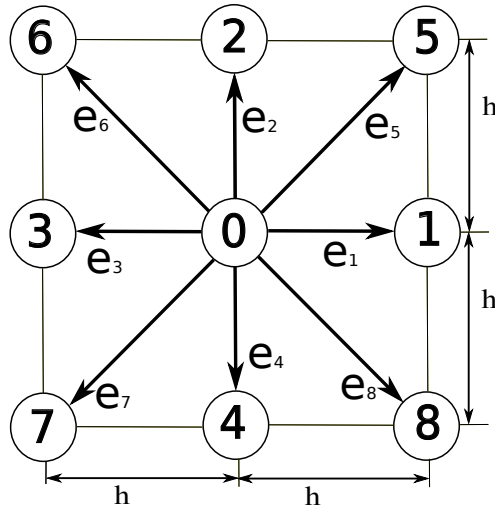


Figure 2.1: Discrete velocities in the D2Q9 model.

The particle distribution function or density distribution function f_i , as primary vari-

able in the LBM, represents the amount of fluid particles moving with velocity \vec{e}_i along the i th direction of the node located at position \vec{x} and at discrete time t . Thus, the nine distribution functions are associated with each node in the D2Q9 model. Macroscopic fluid variables as fluid density ρ and velocity \vec{u} of the fluid which is derived from the moments of distribution function are given by:

$$\rho = \sum_{i=0}^8 f_i \quad (2.4)$$

$$\vec{u} = \frac{1}{\rho} \sum_{i=0}^8 f_i \vec{e}_i \quad (2.5)$$

LBM algorithm is an iterative process over time. At each time step, the fluid particles located on regular lattice have to experience an essential sequence of two mechanisms, called collision and propagation. By adopting a linearized collision operator, BGK (Bhatnagar-Gross-Krook) [128], to deal with fluid particle collision [133], the evolution equation can be given:

Collision step:

$$f_i(\vec{x}, t^+) = f_i(\vec{x}, t) - \frac{1}{\tau} [f_i(\vec{x}, t) - f_i^{eq}(\vec{x}, t)] \quad (i = 0, \dots, 8) \quad (2.6)$$

Propagation step:

$$f_i(\vec{x} + \vec{e}_i dt, t + dt) = f_i(\vec{x}, t^+) \quad (2.7)$$

where the term $f_i(\vec{x}, t^+)$ in Eq (2.6) and (2.7) is called post-collision term, t^+ is an intermediate time $t < t^+ < t + dt$ and follows the collision process. τ is a dimensionless parameter named relaxation time. For any grid node at position \vec{x} , $\vec{x} + \vec{e}_i dt$ is its nearest node along the direction i . f_i^{eq} is the i th equilibrium distribution functions defined as:

$$f_i^{eq}(\vec{x}, t) = w_i \rho \left(1 + \frac{3}{C^2} \vec{e}_i \cdot \vec{u} + \frac{9}{2C^4} (\vec{e}_i \cdot \vec{u})^2 - \frac{3}{2C^2} \vec{u} \cdot \vec{u} \right) \quad (2.8)$$

where w_i is the weight coefficient which is dependent on the model. In the D2Q9 model, $w_0 = \frac{4}{9}$, $w_{1,2,3,4} = \frac{1}{9}$, $w_{5,6,7,8} = \frac{1}{36}$. The kinematic viscosity of fluid ν is related to the lattice velocity C , relaxation time τ and the lattice spacing h through following relation:

$$\nu = \frac{1}{3} \left(\tau - \frac{1}{2} \right) Ch \quad (2.9)$$

It is noted that the restriction of τ in Eq (2.9) satisfies $\tau > 0.5$. Smaller values of τ

imply smaller time steps and therefore increase computational cost. Generally, results are acceptable for $\tau < 1.5$ [134]. According to Eq (2.3) and Eq (2.9), the time step of LBM is:

$$dt = \frac{1}{3\nu} \left(\tau - \frac{1}{2} \right) h^2 \quad (2.10)$$

The fluid is considered to be slightly compressible. The value of Mach number is limited to $M = \frac{u_{max}}{C} \leq 0.1$ in order to insure the compressibility error M^2 less than 1%, where u_{max} is the highest velocity in the flow. The fluid pressure is determined by:

$$p = C_s^2 \rho \quad (2.11)$$

where C_s is the speed of sound, defined as $C_s = \frac{C}{\sqrt{3}}$ [8].

2.2.2 Boundary conditions on obstacles and systems

2.2.2.1 Boundary conditions on obstacles

Solid particles or any other kinds of obstacles are handled with the LB method by positioning them on the lattice. Fig.2.2 shows for example a circular solid obstacle mapped on the LB lattice. The nodes inside an obstacle which are the closest ones to its external surface are called "Solid Boundary" (SB) nodes (red). All the fluid nodes located outside the obstacle, with at least one direction pointing towards a SB node, are called "Fluid Boundary" (FB) nodes (green). All other nodes are fluid nodes (blue). We call a link between a SB and a FB node as a boundary link σi as illustrated in Fig.2.3. Boundary seen by LBM and real solid boundary are shown respectively. A boundary link σi means the direction i pointing from fluid to solid. $-\sigma i$ simply denotes the opposite direction of σi .

The simplest scheme to calculate momentum transfer between a SB and a FB node is the "mid-plane bounce-back" boundary condition on the boundary links [135]. In this method, the solid surface is assumed to be located halfway between the fluid node and solid node. Since fluid particles cannot cross the solid border line that limits the outer solid domain, particle distribution functions coming from SB or FB nodes are reflected along the boundary link σi . For a stationary solid surface, the propagation step, given by Eq 2.7 is then replaced by:

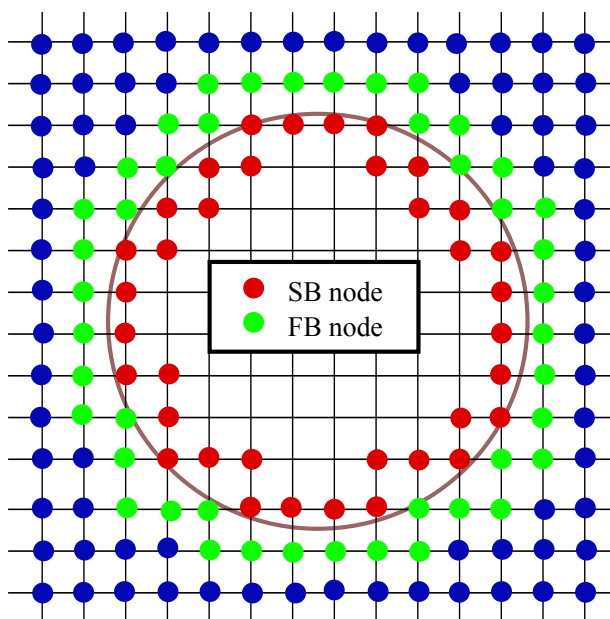


Figure 2.2: A circular solid obstacle mapped on the LB lattice.

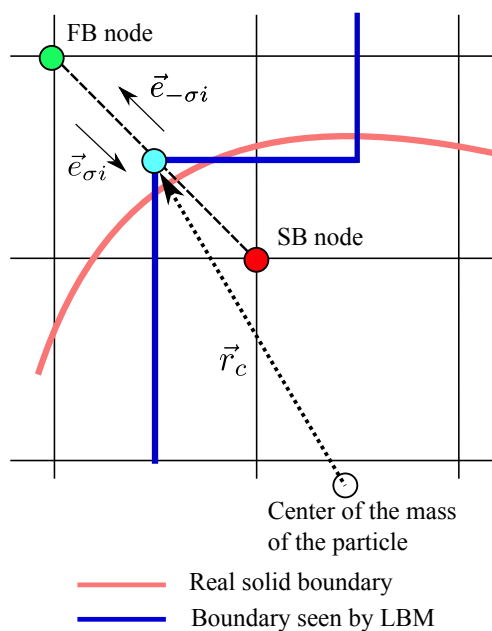


Figure 2.3: A boundary link.

$$\begin{aligned}
f_{-\sigma i}(\vec{x}_{FB}, t + dt) &= f_{\sigma i}(\vec{x}_{FB}, t^+) \\
f_{\sigma i}(\vec{x}_{SB}, t + dt) &= f_{-\sigma i}(\vec{x}_{SB}, t^+)
\end{aligned} \tag{2.12}$$

For a moving boundary, the solid surface velocity need to be considered in the bounce-back rule in order to ensure no-slip condition on the solid surface. This is achieved by using the modified bounce-back rule proposed by Ladd [136]:

$$\begin{aligned}
f_{-\sigma i}(\vec{x}_{FB}, t + dt) &= f_{\sigma i}(\vec{x}_{FB}, t^+) - 2\alpha_i \vec{u}_s \cdot \vec{e}_i \\
f_{\sigma i}(\vec{x}_{SB}, t + dt) &= f_{-\sigma i}(\vec{x}_{SB}, t^+) + 2\alpha_i \vec{u}_s \cdot \vec{e}_i
\end{aligned} \tag{2.13}$$

where $\vec{x}_{SB} = \vec{x}_{FB} + \vec{e}_{\sigma i} dt$, $\alpha_i = 3w_i \rho / C^2$. \vec{u}_s is the boundary velocity at the middle of the boundary link σi . It can be expressed as

$$\vec{u}_s = \vec{u}_p + \vec{\omega}_p \wedge \vec{r}_c \tag{2.14}$$

where \vec{u}_p and $\vec{\omega}_p$ are the translational and angular velocities respectively at the center of mass of the solid obstacle. \vec{r}_c is the vector joining the center of mass \vec{x}_c of the solid obstacle to the middle of the boundary link.

$$\vec{r}_c = \vec{x}_{FB} + \vec{e}_{\sigma i} \frac{dt}{2} - \vec{x}_c \tag{2.15}$$

2.2.2.2 Boundary conditions on systems

As presented in part 2.2.1, we use the distribution function f_i to deduce the pressure and velocity through Eqs 2.4 and 2.5. Thus the pressure or velocity condition on the boundary cannot be imposed directly. For the boundary condition on the system, we adopt the boundary conditions proposed by Zou and He [19] as it is specified below.

(a) Velocity boundary condition

The rectangular simulation domain presented in Fig.2.4 needs to define eight sets of distribution functions denoted from a) to g). The velocity boundary conditions $\vec{U}_0 = \begin{pmatrix} u_x \\ u_y \end{pmatrix}$ are specified to the inlet of the system (case a)). The key step is to determine all the distribution functions at the boundary nodes. After the propagation step, distribution functions f_2, f_3, f_4, f_6, f_7 are already known and f_1, f_5, f_8 are unknown. We need to solve

for ρ , f_1 , f_5 and f_8 , which means that four equations are needed. According to the Eqs 2.4 and 2.5, we can get the following form:

$$f_1 + f_5 + f_8 = \rho - (f_0 + f_2 + f_3 + f_4 + f_6 + f_7) \quad (2.16)$$

$$f_5 - f_8 = \rho u_y - f_2 + f_4 - f_6 + f_7 \quad (2.17)$$

$$f_1 + f_5 + f_8 = \rho u_x + f_3 + f_6 + f_7 \quad (2.18)$$

A fourth equation can be obtained from the non-equilibrium part of distribution functions normal to the boundary. We assume that the bounce-back rule is still correct for the non-equilibrium part of distribution functions. Then it follows that:

$$f_1 - f_1^{eq} = f_3 - f_3^{eq} \quad (2.19)$$

Then the unknown distribution functions f_1 , f_5 , f_8 and fluid density ρ can be obtained by solving Eqs 2.16 - 2.19

$$\rho = \frac{1}{1 - u_x} [f_0 + f_2 + f_4 + 2(f_3 + f_6 + f_7)] \quad (2.20)$$

$$f_1 = f_3 + \frac{2}{3}\rho u_x \quad (2.21)$$

$$f_5 = f_7 - \frac{1}{2}(f_2 - f_4) + \frac{1}{6}\rho u_x + \frac{1}{2}\rho u_y \quad (2.22)$$

$$f_8 = f_6 + \frac{1}{2}(f_2 - f_4) + \frac{1}{6}\rho u_x - \frac{1}{2}\rho u_y \quad (2.23)$$

The distribution functions and density in cases b), c), d) of Fig.2.4 can be solved in a similar procedure. However for the corner, the above formulations are not applicable due to different number of unknown distribution functions at the corner nodes (case e), f), g) and h)). A specific procedure is needed. Consider the bottom left corner node (case e)) as an example. After the propagation step the distribution functions f_3 , f_4 and f_7 are known, f_1 , f_2 , f_5 , f_6 and f_8 need to be solved. Again using the bounce-back rule of the non-equilibrium part, we can find that:

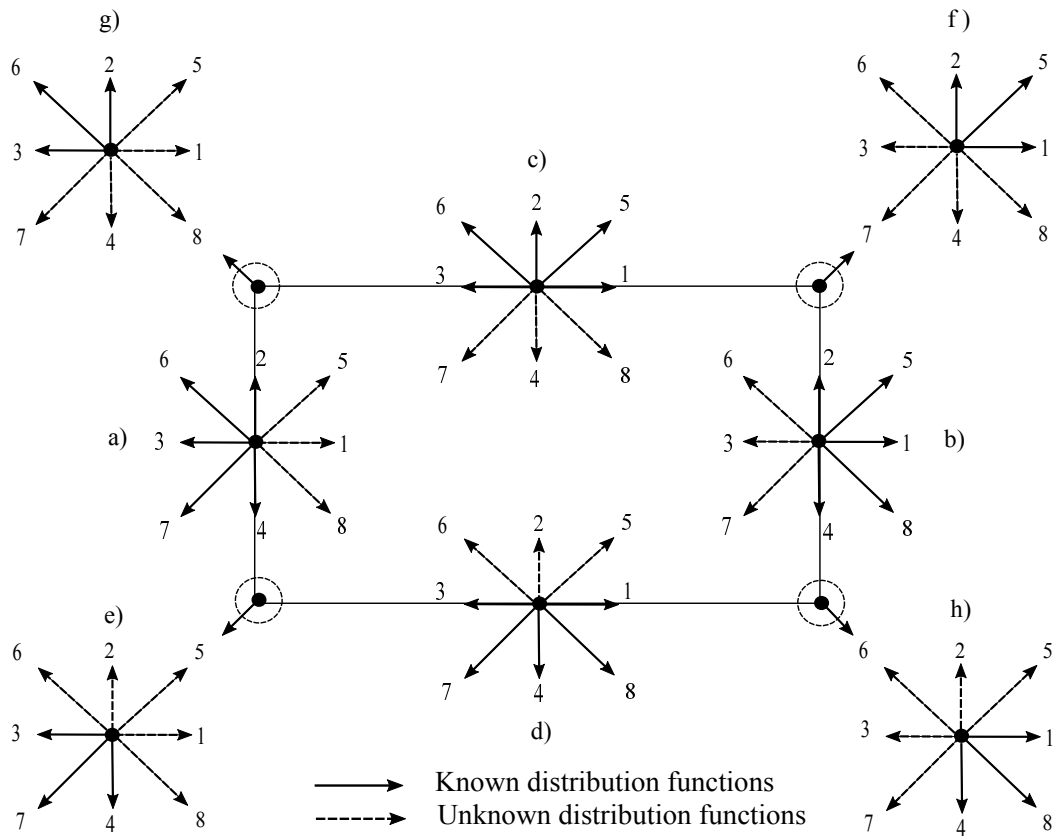


Figure 2.4: LBM boundary conditions.

$$f_1 = f_3 + \frac{2}{3}\rho u_x \quad (2.24)$$

$$f_2 = f_4 + \frac{2}{3}\rho u_y \quad (2.25)$$

In addition, by combining Eqs 2.22 and 2.23 which gives

$$f_5 - f_6 + f_8 = \rho u_x - (f_1 - f_3 - f_7) \quad (2.26)$$

$$f_5 + f_6 - f_8 = \rho u_y - (f_2 - f_4 - f_7) \quad (2.27)$$

Then based on the Eqs 2.5 and 2.24-2.27, f_5 , f_6 and f_8 are obtained as:

$$f_5 = f_7 + \frac{1}{6}\rho(u_x + u_y) \quad (2.28)$$

$$f_6 = \frac{1}{2}[\rho(1 - u_x - \frac{2}{3}u_y) - f_0 - 2(f_3 + f_4 + f_7)] \quad (2.29)$$

$$f_8 = \frac{1}{2}[\rho(1 - \frac{2}{3}u_x - u_y) - f_0 - 2(f_3 + f_4 + f_7)] \quad (2.30)$$

Finally, all the relationships between distribution functions, densities and velocities can be solved with the same procedure for case f), g) and h).

(b) Pressure boundary condition

If pressure condition p is imposed at the inlet of channel (case a)), we specify the fluid densities at the flow boundaries because density is deduced from the formula $p = c_s^2 \rho$. For convenience, we define the vertical velocity $u_y = 0$. ρ is fixed and velocity u_x needs to be determined first. Following the procedure for the velocity boundary conditions, the solutions are given by:

$$f_1 = f_3 + \frac{2}{3}\rho u_x \quad (2.31)$$

$$f_5 = f_7 - \frac{1}{2}(f_2 - f_4) + \frac{1}{6}\rho u_x \quad (2.32)$$

$$f_8 = f_6 + \frac{1}{2}(f_2 - f_4) + \frac{1}{6}\rho u_x \quad (2.33)$$

The similar way for treating the corner for the velocity flow boundaries can be used to deal with the pressure boundary condition as described in the above part.

(c) Periodic boundary condition

Periodic boundary condition is one of the mostly used boundary conditions. The system becomes closed by attaching the edges such as connecting the outlet and inlet. Fig.2.5 presents the schematic view of periodic boundary condition. The fluid particle distribution functions such as f_1, f_5, f_8 leaving from the outlet are assigned to the inlet. The distribution functions f_3, f_6, f_7 at the inlet will transfer to the outlet. If $(x_{max} + \vec{e}_i dt)$ or $(x_{min} + \vec{e}_{-i} dt)$ is out of system, then the periodic boundary condition is realized by:

$$f_i(\vec{x}_{min}, t + dt) = f_i(\vec{x}_{max}, t^+) \quad (2.34)$$

$$f_i(\vec{x}_{max}, t + dt) = f_{-i}(\vec{x}_{min}, t^+) \quad (2.35)$$

where $\vec{x}_{max} = (x_{max}, y)$ and $\vec{x}_{min} = (x_{min}, y)$

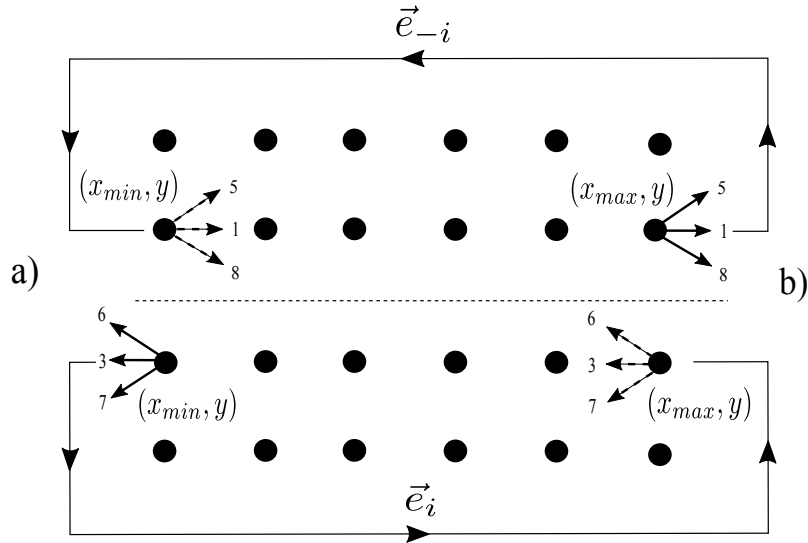


Figure 2.5: Schmeatic view of streaming step when using periodic boundary conditions.

(d) Neumann's boundary condition on velocity

Neumann's boundary condition on velocity is an effective approach to simulate problems with an infinitely fluid domain [137]. In some particle transport problems, a constant

velocity is imposed at the upstream and the flow field is considered to be fully developed at the outlet. Thus, Neumann's boundary condition is used without the need to exceed the computational domain.

The downstream of flow such as outlet is generally set to:

$$\frac{\partial u_x}{\partial x} = 0 \text{ at } x = x_{max} \quad (2.36)$$

In order to achieve zero velocity gradient, if \vec{j} is a unit vector normal to the boundary pointing outside, the distribution functions at the outlet should be defined as:

$$f_i(\vec{x}_{max}, t + dt) = f_i(\vec{x}_{max} - \vec{j}, t + dt) \quad (2.37)$$

where $\vec{x}_{max} = (x_{max}, y)$.

2.3 Discrete element method

2.3.1 Contact law

The discrete element method (DEM), introduced by Cundall and Strack [93], is a very popular numerical approach to deal with solid particle contact interactions. The interactions between particles respect contact law. In DE method, particles move according to Newton's law and their contact follows a "soft spheres" approach. Particles are allowed to slightly overlap amongst each other during contact. We consider two particles a and b located respectively at positions \vec{r}_a and \vec{r}_b with radius R_a and R_b as shown in Fig.2.6. Their velocities are \vec{V}_a and \vec{V}_b respectively. The angular velocities of particle a and b are $\vec{\omega}_a$ and $\vec{\omega}_b$. A collision between two particles causes a deformation, then the overlap χ_n is defined as

$$\chi_n = R_a + R_b - (\vec{r}_a - \vec{r}_b) \cdot \vec{n} \quad (2.38)$$

where \vec{n} is unit normal vector as seen in Fig.2.6 and calculated as

$$\vec{n} = \frac{\vec{r}_a - \vec{r}_b}{\|\vec{r}_a - \vec{r}_b\|} \quad (2.39)$$

The relative velocity \vec{V}_{rab} of the particle a relatively to the particle b at the contact point is written:

$$\vec{V}_{rab} = (\vec{V}_a - \vec{\omega}_a \wedge R_a \vec{n}) - (\vec{V}_b + \vec{\omega}_b \wedge R_b \vec{n}) \quad (2.40)$$

$$= \vec{V}_{ab} - (R_a \vec{\omega}_a + R_b \vec{\omega}_b) \wedge \vec{n} \quad (2.41)$$

with $\vec{V}_{ab} = \vec{V}_a - \vec{V}_b$. The relative velocities in the normal and tangential directions are equal to:

$$\vec{V}_{rab}^n = (\vec{V}_{ab} \cdot \vec{n}) \vec{n} \quad (2.42)$$

$$\vec{V}_{rab}^t = -\vec{n} \wedge (\vec{n} \wedge \vec{V}_{rab}) \quad (2.43)$$

According to the particle velocity, tangential vector \vec{t} is defined:

$$\vec{t} = \frac{\vec{V}_{rab}^t}{\|\vec{V}_{rab}^t\|} \quad (2.44)$$

The overlap during a contact is kept relatively small compared to the particle size, in addition, in order to keep valid the rigid body assumption of particles, this overlap has to stay negligible. In these conditions, the contact force can be divided into two components:

$$\vec{F}_{cab} = F_n \vec{n} + F_s \vec{t} \quad (2.45)$$

where F_n and F_s are normal contact force and shear force respectively.

2.3.2 Normal contact force

The calculation of the normal contact force F_n from particle a to particle b is directly linked to the value of χ_n . If the overlap $\chi_n < 0$ as illustrated in Fig.2.6, then an interaction force for the two colliding particles is computed:

$$\ddot{\chi}_n = -\frac{F_n^a}{m_a} + \frac{F_n^b}{m_b} \quad (2.46)$$

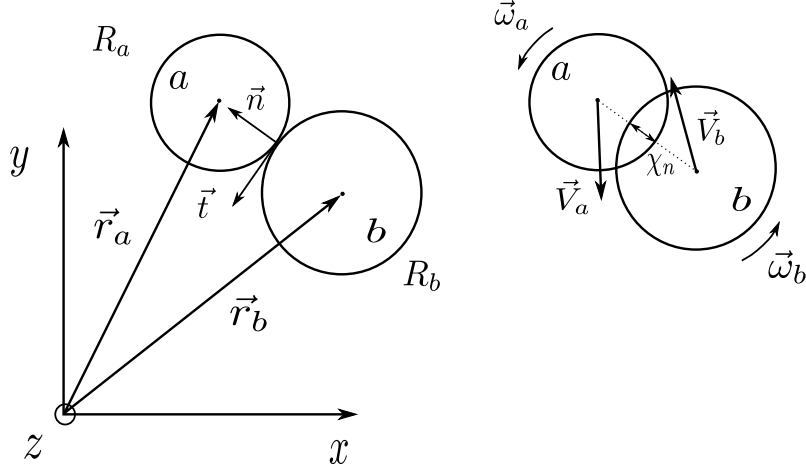


Figure 2.6: Illustration of a collision between two particles with overlap χ_n .

with Newton third law, $F_n^a = -F_n^b = F_n$, where m_a and m_b are particles mass. Then the following equation is given

$$\ddot{\chi}_n = -\frac{F_n}{m_p} \quad (2.47)$$

in which $m_p = \frac{m_a m_b}{m_a + m_b}$.

Several models of contact law exist in literature [138]. Here we will use the widely sprayed "linear spring dashpot" (LSD) model [139, 140, 141, 142] for the normal component of the contact force.

$$F_n = K_n \chi_n + \gamma_n \dot{\chi}_n \quad (2.48)$$

where K_n is the normal stiffness coefficient of the interaction and γ_n is a damping coefficient. $\dot{\chi}_n$ is the time derivative of χ_n . We can get the following equation by combining the Eqs. 2.47 and 2.48,

$$m_p \ddot{\chi}_n + \gamma_n \dot{\chi}_n + K_n \chi_n = 0 \quad (2.49)$$

With initial conditions $\chi_n(t=0) = 0$ and $\dot{\chi}_n(t=0) = u_p^0$, we can get the solution of the Eq.2.49:

$$\chi_n = u_p^0 \frac{t_c}{\pi} \exp\left(-\frac{\gamma_n}{2m_p} t\right) \sin\left(\frac{\pi}{t_c} t\right) \quad (2.50)$$

where t_c is the contact duration which can be expressed as [139, 94]

$$t_c = \pi \left(\frac{k_n}{m_p} - \left(\frac{\gamma_n}{2m_p} \right)^2 \right)^{-\frac{1}{2}} \quad (2.51)$$

The stability of the explicit scheme for the time integration holds if the time step of the DE method dt_{DE} has to be sufficiently small to describe the wave propagation in the mass-spring system constituted by the solid granular assembly. With the LSD model, equation 2.51 is of practical importance, since the integration of the motion equations is stable only if the integration time-step dt_{DE} is much smaller than t_c . A ratio of 10 between dt_{DE} and t_c is usual to avoid instability of the numerical method [8]. Collision inelasticity is taken into account through the damping γ_n previously introduced. The LSD force model leads to a constant restitution coefficient defined as:

$$\kappa = \frac{u_p^1}{u_p^0} = \exp\left(-\frac{\pi}{\sqrt{4k_n m / \gamma_n^2 - 1}}\right) \quad (2.52)$$

in which u_p^0 and u_p^1 are the velocities of the particles before and after collision, respectively.

2.3.3 Shear contact force

The shear force F_s is calculated using an extension of the method proposed by Cundall-Strack [93]. When the contact is formed, F_s is initialized to zero. F_s is computed incrementally with an increment ΔF_s calculated by accumulating the path of moving contact point between the two particles in contact [143].

$$F_s = F_s + \Delta F_s \quad (2.53)$$

$$\Delta F_s = -K_s \Delta u_s \quad (2.54)$$

K_s represents the interaction shear stiffness and Δu_s the increment of the tangential relative displacement of the contact point. Tangential sliding occurs if:

$$|F_s| > \mu F_n \quad (2.55)$$

with $\mu = \min(\mu_a, \mu_b)$ and μ_a and μ_b are particle friction coefficients. Contact parameters K_n and K_s can be derived from particle properties E , ν , which are respectively Young's

modulus and Poisson's coefficient [144]:

$$K_n = 2 \frac{E_a R_a E_b R_b}{E_a R_a + E_b R_b} \quad \text{and} \quad K_s = 2 \frac{E_a \nu_a R_a E_b \nu_b R_b}{E_a \nu_a R_a + E_b \nu_b R_b} \quad (2.56)$$

For each particle, total contact force F_c is computed with summation of contact force over all interacting partners.

2.3.4 Particle dynamics

The particle is subject to a contact force and external forces at the same time. Position and velocity of each solid particle are deduced from the explicit time integration of the Newton's second law:

$$m_p \frac{d\vec{u}_p}{dt} = \vec{F}_c + \vec{F}_{ext} \quad (2.57)$$

where m_p , \vec{x}_p and $\vec{u}_p = \frac{d\vec{x}_p}{dt}$ are respectively particle mass, position and velocity of particle. \vec{F}_c is contact force acted from other particles and \vec{F}_{ext} is the external force. Rotations of particles are computed in the same way by integrating the equation:

$$J \frac{d\vec{\omega}_p}{dt} = \vec{T}_c \quad (2.58)$$

where \vec{T}_c is the torque resulting from the inter-particle forces, J the moment of inertia of particles and $\vec{\omega}_p$ the angular velocity. Moment of inertia of particles can be expressed as:

$$J = \begin{cases} m_p r_p^2 & \text{for circle} \\ \frac{2m_p r_p^2}{5} & \text{for sphere} \end{cases} \quad (2.59)$$

where r_p is the particle radius. At each time step of the DEM, the time integration is performed by Verlet's algorithm [145]. The variation of the position of the particle subject to the force f can be derived from the Taylor development as:

$$x(t + dt) = x(t) + \frac{\partial x(t)}{\partial t} dt + \frac{f}{m_p} \frac{dt^2}{2} + \frac{\partial^3 x(t)}{\partial t^3} \frac{dt^3}{3!} + o(dt^4) \quad (2.60)$$

$$x(t - dt) = x(t) - \frac{\partial x(t)}{\partial t} dt + \frac{f}{m_p} \frac{dt^2}{2} - \frac{\partial^3 x(t)}{\partial t^3} \frac{dt^3}{3!} + o(dt^4) \quad (2.61)$$

We can express a new one by merging these two equations:

$$x(t + dt) = 2x(t) - x(t - dt) + \frac{f}{m_p} dt^2 \quad (2.62)$$

and then, we are able to calculate new positions at time $t + dt$ base on position at time t and $t - dt$ and force at time t . The particle velocity can be calculated:

$$u_x(t) = \frac{x(t + dt) - x(t - dt)}{2dt} \quad (2.63)$$

2.4 Coupling of LBM-DEM

The exchange of information is required when combining LBM with DEM to model the particle interactions. Hydrodynamic forces and torques are deduced from the LBM computation and used in the DEM cycle to compute new positions and velocities of solid particles, which in turn define the new boundary conditions for the fluid dynamic problem [8]. The achievement of the coupled LBM-DEM has to be done by considering the fact that each method is characterized by a different time discretization. Thus in the following, we will present the calculation of hydrodynamic force and numerical time step adjustment for the coupling.

2.4.1 Subcycling time integration

The basic idea for the coupling of the DEM and LBM is a subcycling scheme. An overview of flowchart of the coupled LBM-DEM is illustrated in Fig.2.7. Generally, the DEM time step dt_{DE} is smaller than the LBM time step dt . Consequently an integer number of DEM loops should be included in a single LBM cycle. In order to achieve the correspondence between the two time steps used by LBM and DEM, the DEM time step dt_{DE} is reduced to a new value.

$$dt'_{DE} = \frac{dt}{n} \quad (2.64)$$

where n is the nearest integer greater or equal to dt/dt_{DE} . Subcycling time integration is created between LBM and DEM. Eq 2.64 indicates that one computational time step of the LBM includes n substeps of time integration with the DEM.

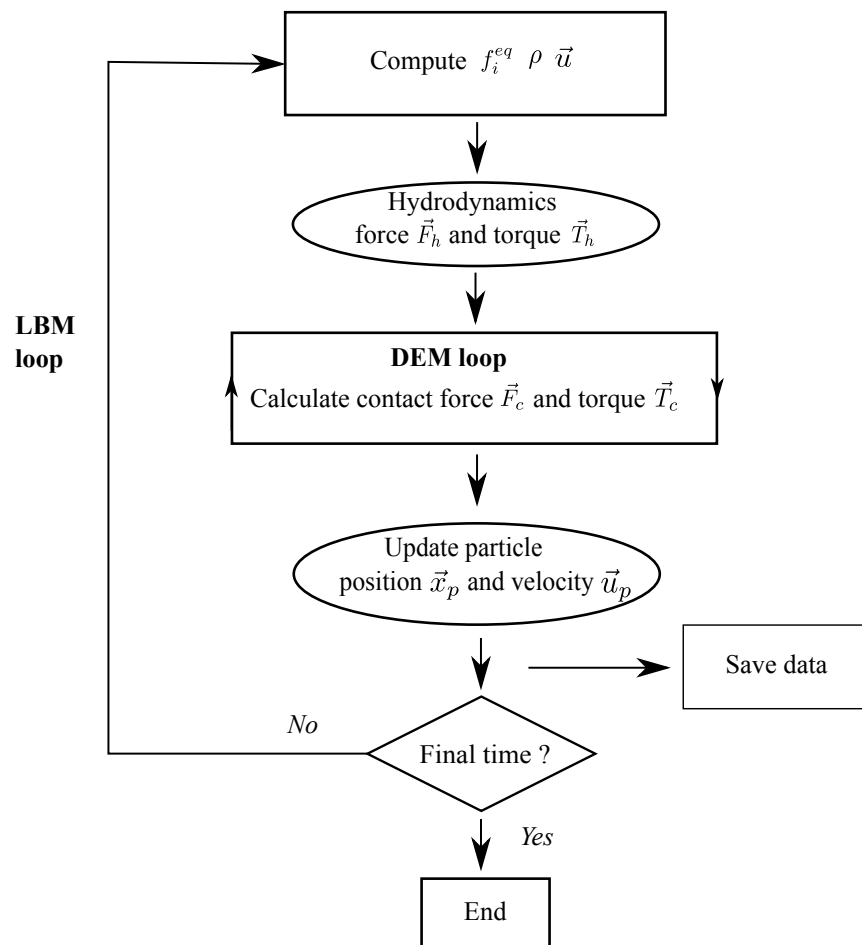


Figure 2.7: Flowchart of the coupled LBM and DEM.

2.4.2 Forces and torques acting on the particles

The fluid force and torque acting on an obstacle can be evaluated from the momentum exchange between fluid and solid particle surface over all boundary links of the obstacle [8]:

$$\vec{F}_h(t + \frac{1}{2}dt) = \sum_{\sigma i} 2 \frac{\Omega}{dt} [f_{\sigma i}(\vec{x}, t^+) - \alpha_i \vec{u}_s \cdot \vec{e}_i] \vec{e}_{\sigma i} \quad (2.65)$$

$$\vec{T}_h(t + \frac{1}{2}dt) = \sum_{\sigma i} \vec{T}_{\sigma}(\vec{x}, t + \frac{1}{2}dt) \quad (2.66)$$

where Ω is the cell lattice surface in 2D (cell lattice volume for 3D case). To be time consistent, hydrodynamic forces and torques applied on obstacles are obtained by an average over two consecutive LBM time-steps:

$$\vec{F}_h(t) = \frac{1}{2} \left[\vec{F}_h(t + \frac{1}{2}dt) + \vec{F}_h(t - \frac{1}{2}dt) \right] \quad (2.67)$$

$$\vec{T}_h(t) = \frac{1}{2} \left[\vec{T}_h(t + \frac{1}{2}dt) + \vec{T}_h(t - \frac{1}{2}dt) \right] \quad (2.68)$$

Hydrodynamic forces F_h and torques T_h , deduced from equations 2.67 and 2.68, are then added to contact forces obtained with the DEM. Therefore, Newton's equations (2.57) and (2.58) are replaced by:

$$m_p \frac{d\vec{u}_p}{dt} = \vec{F}_c + \vec{F}_h \quad (2.69)$$

$$\vec{T}_c + \vec{T}_h = J \frac{d\vec{\omega}_p}{dt} \quad (2.70)$$

Then, the DEM cycle computes new positions and velocities of solid particles, which in turn define the new boundaries for the fluid dynamic problem. During the subcycling, the hydrodynamic forces and torques remain unchanged, this is why n in Eq.(2.64) should stay small. Finally the coupling between LBM and DEM is established. The coupled LBM-DEM are implemented in a "house" code developed at Laboratoire de Génie Civil et Génie Mécanique (LGCGM) named "Albadec".

2.5 Validations of LBM-DEM

In this section, the study of classical fluid mechanics problems are presented in order to validate the 2D computation code based on the LBM algorithm and on the coupling of the LB-DE methods respectively.

2.5.1 2D Poiseuille flow

We use the steady 2D Poiseuille flow in this subsection to validate the LBM code. Incompressible fluid flows between stationary parallel infinite plates at $y = 0$ and $y = L_y$ as shown in Fig.2.8. A pressure drop $\Delta p = p_1 - p_2$ driving the Newtonian fluid is applied between the inlet and outlet of the system. The no-slip boundary condition is imposed at the top and bottom wall, respectively.

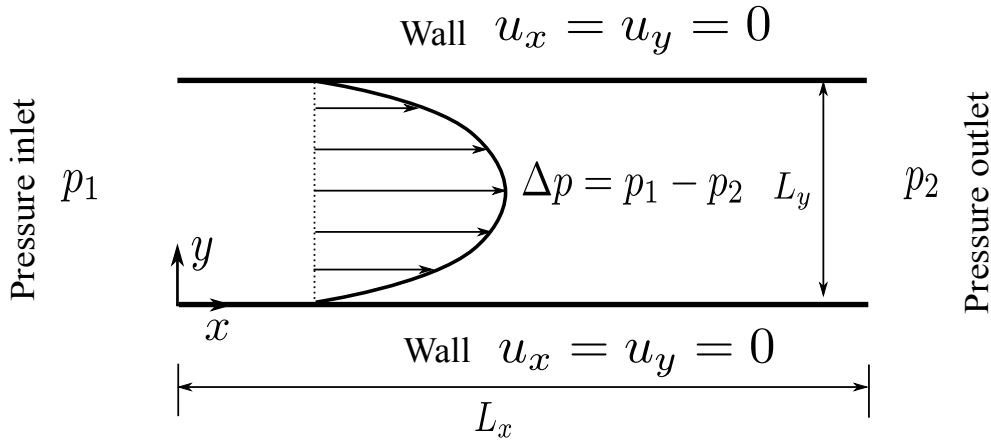


Figure 2.8: Schematic view of 2D Poiseuille flow and boundary condition.

Theoretical stationary solution of Poiseuille flow can be solved analytically. Velocity of Poiseuille flow reaches its maximum in the middle of the channel, the relationship between average velocity U_{aver} and maximum velocity is given as:

$$U_{aver} = \frac{2}{3}u_{max} \quad \text{with} \quad u_{max} = \frac{\Delta p L_y^2}{8\mu L_x} \quad (2.71)$$

Then Reynolds number of the Poiseuille flow is used here:

$$Re = \frac{U_{aver} L_y}{\nu} \quad (2.72)$$

where ν is kinematic viscosity.

The LBM is validated not only in stationary state by comparing with the series solution for the transient behavior of Poiseuille which is expressed as [82]

$$u_x(y, t) = \frac{\Delta p}{2L_x \nu \rho} (y(y - L_y)) + \sum_{n=0}^{\infty} \frac{4\Delta p L_y^2}{L_x \nu \rho \pi^3 (2n + 1)^3} \sin\left(\frac{\pi y (2n + 1)}{L_y}\right) \exp\left(\frac{-1(2n + 1)^2 \pi^2 \nu t}{L_y^2}\right) \quad (2.73)$$

A series of important parameters used in the simulation are given in Table 2.1. Fig.2.9 shows a comparison between numerical simulation results and series solution. The velocity profiles agree closely with series analytical solution at different time in Fig.2.9.

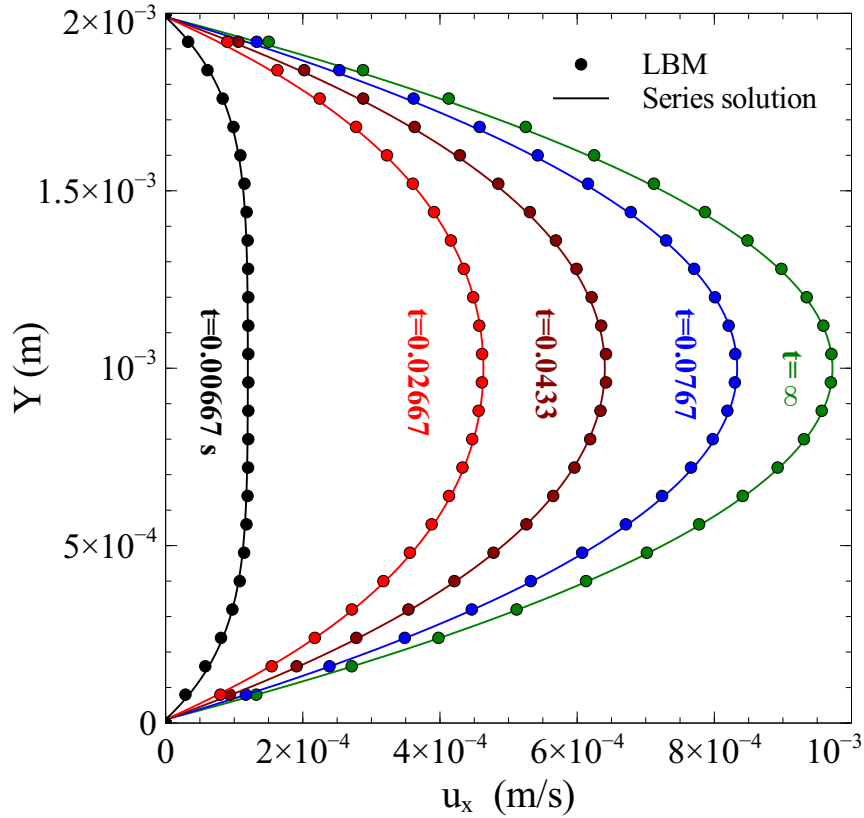


Figure 2.9: Comparison of velocity profile obtained with LBM and series solutions for Poiseuille flow at different times.

A peak velocity of Poiseuille flow is $u_{peak} = 9.8 \times 10^{-4} \text{m/s}$ for the steady state solution. The maximum velocity calculated from LBM is $u_{max} = 9.8307 \times 10^{-4} \text{m/s}$. The discrepancy between the maximum velocity can be calculated:

Table 2.1: Parameters used in the simulation of Poiseuille flow.

Channel length, L_x	0.01	[m]
Channel height, L_y	0.002	[m]
Pressure drop, Δp	0.2	[Pa]
Fluid kinetic viscosity, ν	10^{-5}	[m ² /s]
Fluid density, ρ	10^3	[kg/m ³]
Reynolds number, Re	0.13	[-]
Relaxation time, τ	1	[-]
Lattice spacing, h	2×10^{-5}	[m]

$$err_{peak} = \left| \frac{u_{peak} - u_{max}}{u_{peak}} \right| \times 100\% = 0.313\% \quad (2.74)$$

In order to obtain more precise results, the effect of relaxation time τ and lattice spacing h on numerical solution is studied. The discrepancy between LBM and analytical solution is computed:

$$err = \frac{\sum_{i,j} |u_{analy}(i,j) - u_{LBM}(i,j)|}{\sum_{i,j} |u_{analy}(i,j)|} \times 100\% \quad (2.75)$$

where $u_{LBM}(i,j)$ is the fluid velocity of a node indexed by i and j in LBM and $u_{analy}(i,j)$ is the analytical solution. The results of discrepancy between LBM and analytical solution of Poiseuille flow are shown in Table 2.2 and Table 2.3. Based on Eq 2.10, LBM comes with the definition of three parameters: h , τ and dt . It is noted that the relation time should $\tau > 0.5$. For a fixed lattice spacing and a given fluid viscosity, smaller τ implies smaller time step, as a result, the discrepancy between the LBM and analytical solution decreases as presented in Table 2.2. As discussed in Ref.[134], results are acceptable for $\tau < 1.5$.

Table 2.2: Discrepancy of velocity profile between LBM and series solution of Poiseuille flow for different τ .

Relaxation time, τ	0.6	0.8	1	1.2
Discrepancy, err	0.023%	0.07%	0.14%	0.15%

The lattice spacing h has a direct impact on the discrepancy. Smaller h lead to more precious results, however, it increases the computation cost. As shown in Table 2.3, the discrepancy between LBM and analytical solution decreases with the decrease of lattice spacing, where N_x is node number. Larger node number means smaller h . Thus, the

parameter h , τ and time step should be chosen in balance in LBM.

Table 2.3: Discrepancy of velocity profile between LBM and series solution of Poiseuille flow for different node numbers.

Node number, N_x	300	400	500	600
Discrepancy, err	0.14%	0.07%	0.03%	0.01%

2.5.2 Couette flow

Couette flow is usually used as a mean to study the suspension flow behavior in simple shear flow. It is another channel flow similar to the Poiseuille flow, but the flow is driven by a moving plate. The fluid is confined between two infinite walls at $y = 0$ and $y = L_y$. The schematic view of Couette flow and boundary condition are shown in Fig.2.10. The lower wall is fixed and the upper wall is moving with a constant velocity U_0 . Periodic boundary condition is applied on the left side and right side.

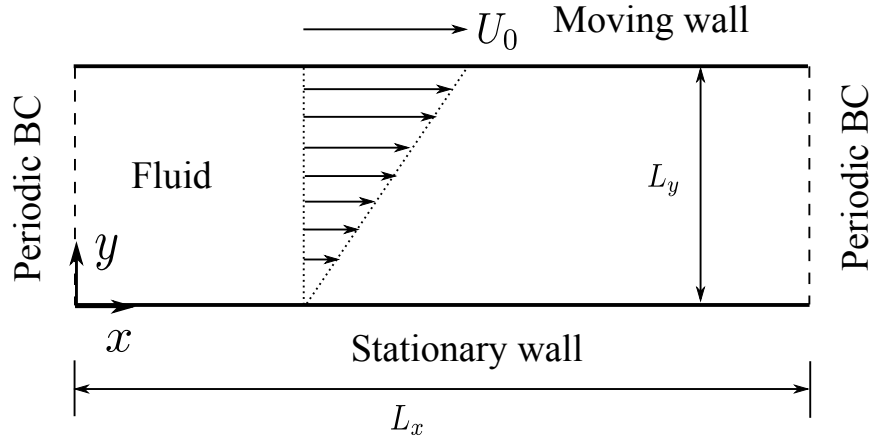


Figure 2.10: Schematic view of Couette flow in 2D and boundary condition.

The series solution for the time-dependent behavior of the Couette flow is [82]:

$$u_x(y, t) = \frac{U_0}{L_y}y + \sum_{n=1}^{\infty} \frac{2U_0}{n\pi} (-1)^n \sin\left(\frac{n\pi}{L_y}y\right) \exp\left(-\nu \frac{n^2\pi^2}{L_y^2}t\right) \quad (2.76)$$

Some simulation parameters are listed in Table 2.4 for the simulation. The velocity profiles across the flow obtained using LBM are compared with the series solution at several time steps including the steady state solution. The numerical results are presented in Fig.2.11. The predicted LBM results agree well with the analytical solution.

Table 2.4: Parameters used in the simulation of Couette flow.

Channel length, L_x	0.01	[m]
Channel height, L_y	0.002	[m]
Wall velocity U_0	0.0001	[m/s]
Fluid kinetic viscosity, ν	10^{-6}	[m ² /s]
Fluid density, ρ	10^3	[kg/m ³]
Reynolds number, $Re = \frac{U_0 L_y}{\nu}$	0.2	[-]
Relaxation time, τ	0.8	[-]
Lattice spacing, h	2×10^{-5}	[m]

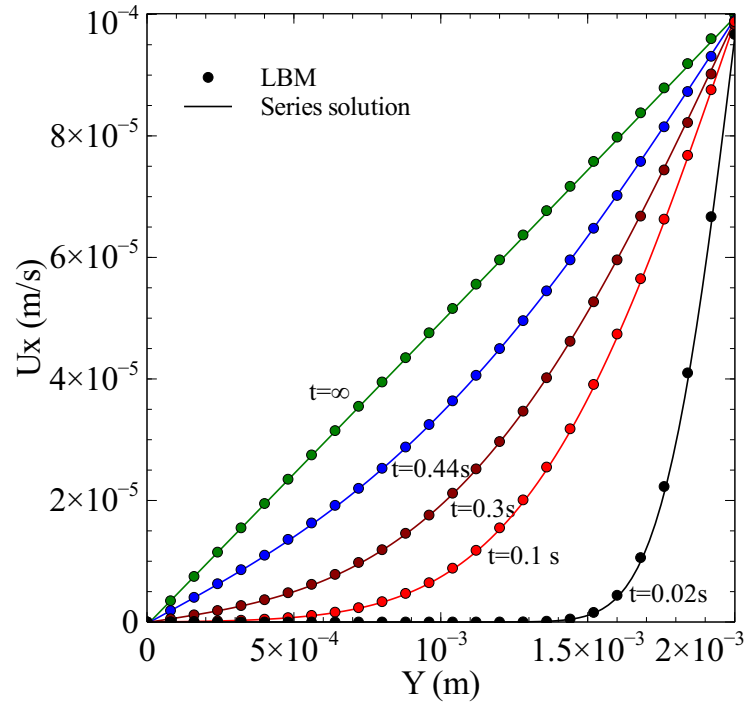


Figure 2.11: Comparison of velocity profile obtained with LBM and series solutions for Couette flow at different times.

The discrepancy between LBM and analytical solution of Couette flow is calculated. The results are presented in Table 2.5. From these results, we find that the impact of relaxation time τ and lattice spacing h on numerical solution of Couette flow have the same tendency as the one of Poiseuille flow. A small τ or small h can obtain more accurate solution and decrease the discrepancy compared to analytical solution. However, it leads to the increase of the computational cost.

Table 2.5: Discrepancy of velocity profile between LBM and series solution of Couette flow.

Relaxation time, τ	0.6	0.8	1
Discrepancy, <i>err</i>	0.4%	0.5%	0.7%
Node number, N_x	400	500	600
Discrepancy, <i>err</i>	0.71%	0.5%	0.3%

2.5.3 Flow around a fixed cylinder in 2D

The single obstacle flow case is mostly used as the validation example. The problem is shown in Fig.2.12. The circle obstacle is set in a rectangular channel on the middle place along y and asymmetrically along x . The channel length and height are L_x and L_y respectively. The obstacle represents a cylinder with diameter d . The computational domain and specified boundary conditions are shown in Fig.2.12.

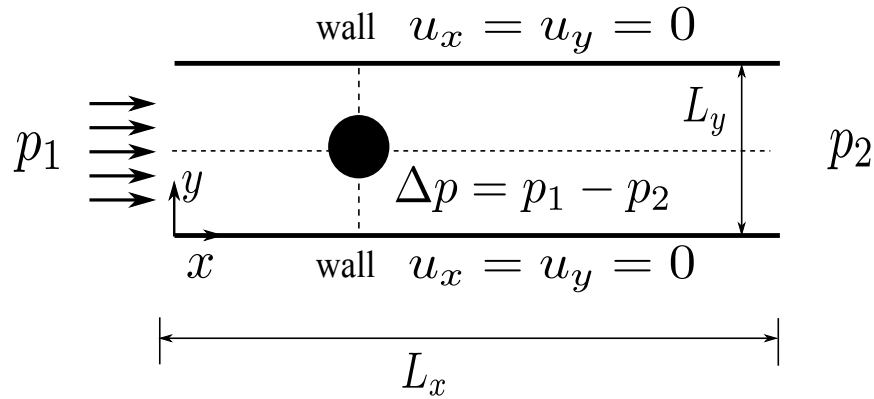


Figure 2.12: Schematic view of the problem of the flow around a circle between two parallel plats.

Table 2.6 presents the values used in the simulation. In order to determine the correct resolution, three different values of $d/h = 8, 10, 12$ are examined. The results of the velocity profiles across the cylinder along x and y directions obtained from LBM and CFD software respectively are shown in Fig.2.13. The discrepancy between the velocity profile obtained with LBM and Comsol are computed

$$err = \frac{\sum_{i,j} |u_{xCFD}(i, j) - u_{xLBM}(i, j)|}{\sum_{i,j} |u_{xCFD}(i, j)|} \times 100\% \quad (2.77)$$

where $u_{xLBM}(i, j)$ is the fluid velocity of a node indexed by i and j in LBM. $u_{xCFD}(i, j)$ is the fluid velocity obtained with Comsol and its position is the same the $u_{xLBM}(i, j)$. Then the discrepancy for $d/h = 8, 10, 12$ and CFD software is obtained. The computational

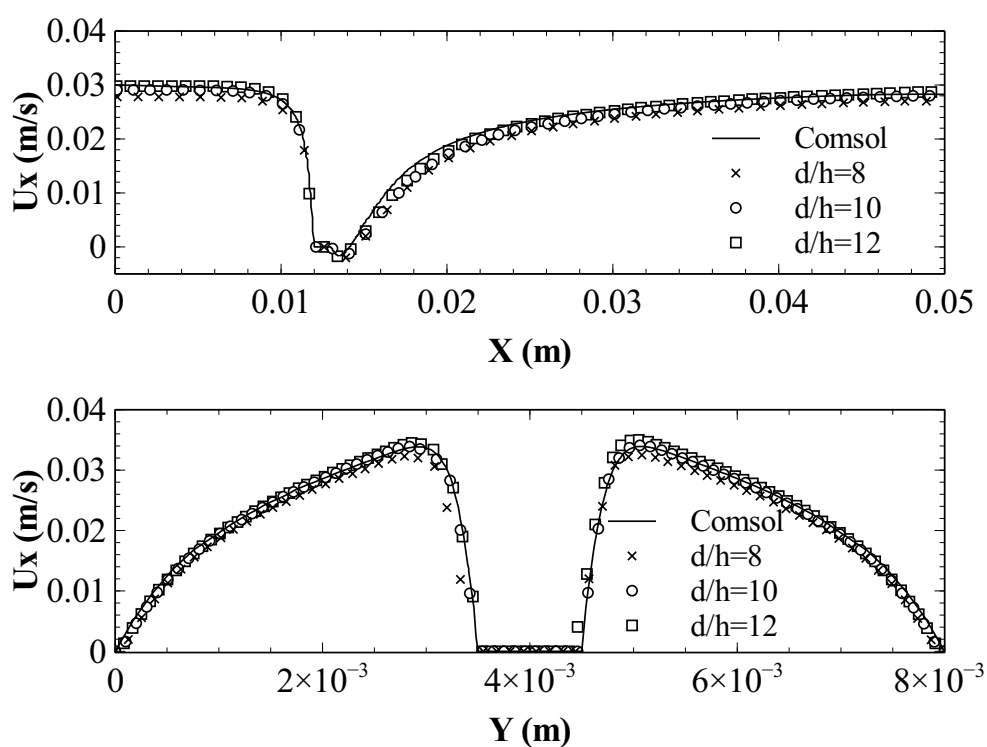


Figure 2.13: Velocity profiles obtained with LB methods and with CFD software for a fluid flowing around a circular cylinder, different values d/h of lattice are studied, where d is the cylinder diameter and h is the lattice spacing.

time t_{end} and time step are given in Table 2.7. The reason leads to this discrepancy is that the solid boundary in LBM is dealt with by half-way bounce-back rule and it is located between fluid boundary and solid boundary and just likes steps. For the resolutions of $d/h = 8$, the discrepancy reached as much as 7.26%, this accuracy is not sufficient whereas for $d/h = 12$ the resolution takes much computation time. Thus, a resolution of $d/h = 10$ is a good compromise between accuracy and computation time.

Table 2.6: Parameters used in the simulation of the fluid flowing around a cylinder

Channel length, L_x	0.05	[m]
Channel height, L_y	0.008	[m]
Cylinder diameter, d	0.001	[m]
Pressure drop, Δp	0.35469	[Pa]
Fluid kinetic viscosity, ν	10^{-6}	[m ² /s]
Fluid density, ρ	10^3	[kg/m ³]
Relaxation time, τ	0.8	[-]
Lattice spacing, h	1.25×10^{-4} , 1×10^{-4} , 8.3×10^{-5}	[m]
Time step, dt	0.000521, 0.000333, 0.000231	[s]

Table 2.7: Discrepancy of velocity between LBM and Comsol

d/h	8	10	12	[-]
err	7.26%	3.24%	1.56%	[-]
t_{end}	16.41	17.11	18.63	[s]

Table 2.8: Parameters used in the simulation of the fluid flowing around a cylinder

	$F_D \times 10^{-4}$ (N)	C_D
CFD	8.427	1.87
$d/h = 12$	8.395	1.88
$d/h = 10$	8.453	2
$d/h = 8$	8.171	2.11

The drag force F_D applied on the cylinder is also calculated. The drag coefficients C_D which depends on fluid density, cross-sectional area S and fluid average velocity U_0 is expressed as:

$$C_D = 2 \frac{F_D}{\rho U_0^2 S} \quad (2.78)$$

In 2D case, the cross-sectional area S is equal to d . Table 2.8 compares C_D obtained from LBM with different resolutions d/h of lattice and CFD software. The value of C_D can be accepted for $d/h \geq 10$.

2.5.4 Flow in porous media

In many engineering problems such as filtration [35], geotechnics problems [130], a fundamental understanding of the flow through porous media is of important interest. In the following, Darcy's law is used to test the program through simulating the fluid flow in the porous media. A series of parameters used in the simulations are shown in Table.2.9. Pressure drop is applied between the inlet and outlet of the channel. The velocity field in an example of porous media is shown in Fig.2.14.

Table 2.9: Parameters used in the simulation of the fluid through porous media

Channel length, L_x	0.05	[m]
Channel height, L_y	0.008	[m]
Porosity, ϕ	0.709	[-]
Pressure drop, Δp	0.05, 0.1, 0.3, 0.4, 0.5, 0.6	[Pa]
Fluid kinetic viscosity, ν	10^{-6}	[m ² /s]
Fluid density, ρ	10^3	[kg/m ³]
Relaxation time, τ	0.8	[-]
Lattice spacing, h	5×10^{-5}	[m]

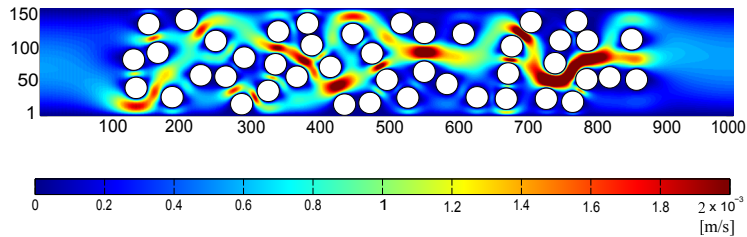


Figure 2.14: Velocity field in porous media for $\Delta p = 0.4$ Pa .

The flow rate Q can be computed at the outlet of the channel. According to the Eq.(1.10), the term $\frac{-\kappa}{\mu}$ is constant for fixed fluid and porous media. Fig.2.15 presents the relationship between Q and $A|\nabla p|$. $\frac{\kappa}{\mu}$ represents the slope of the line in Fig.2.15. As a consequence, the relationship of discharge and the product of cross-sectional area and the pressure gradient ($A \cdot \nabla p$) obtained with our code is tested to be linear $\frac{\kappa}{\mu} = \frac{Q}{A|\nabla p|} = 4.5625 \times 10^{-5}$. It is observed that the simulation results follows the Darcy's law.

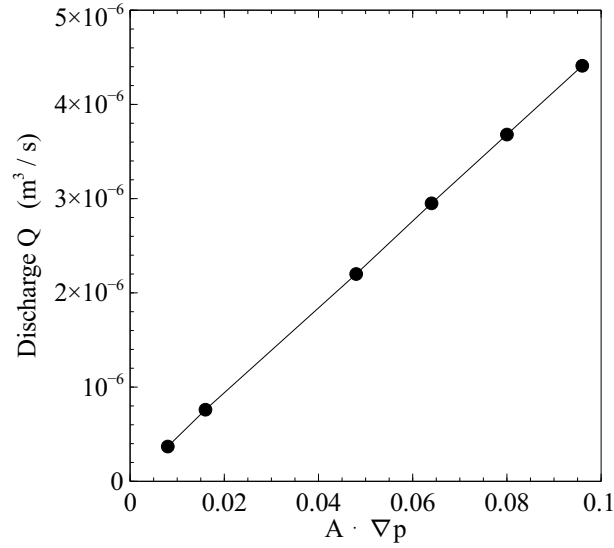


Figure 2.15: The relationship between discharge Q calculated at the outlet and the product of cross-sectional area and the pressure gradient ($A \cdot \nabla p$) follows Darcy's law.

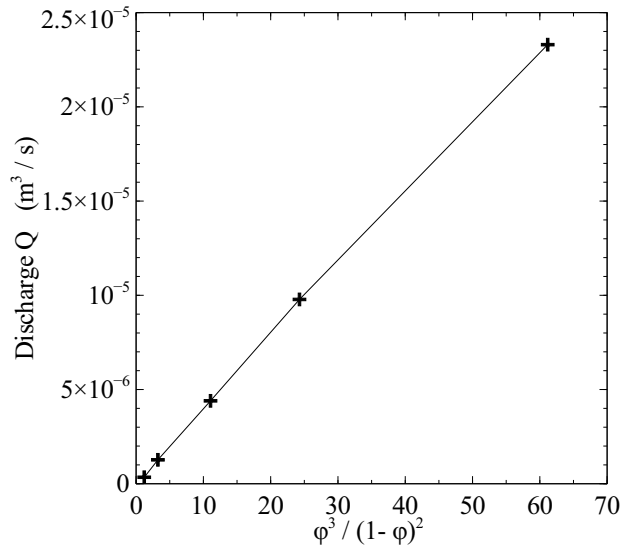


Figure 2.16: Discharge Q at the outlet is proportional to $\frac{\phi^3}{(1-\phi)^2}$ as in Kozeny-Carman relation.

Kozeny-Carmann equation, described in part 1.2.3.2 of chapter 1, is also used to test our code. Here we consider the porous media with porosity ϕ , constituted by circular obstacles of diameter d . Varying the number N of obstacle leads different porosity of media in each simulation. For the given fluid and porous media, $\frac{\Phi_s^2 D_s^2}{180\mu}$ is constant. Therefore relation between Q and $\frac{(\phi)^3}{(1-\phi)^2}$ should be linear. Fig. 2.16 presents dependancy of Q with $\frac{(\phi)^3}{(1-\phi)^2}$ obtained with our LB code. It can be clearly observed that the linear relation is retrieved which validates our program.

2.5.5 Moving cylinder in channel flow

In this section, we validate the coupled LBM-DEM. First case, we consider a fixed cylinder placed in a channel as Fig.2.12. A series of pressure drop is applied between the inlet and outlet respectively. The values of pressure drop is shown in Table 2.10. The same boundary conditions are used with Fig.2.12. Then the drag coefficient of cylinder is calculated with different Reynolds number. It is noted that the grid resolution used is equal to $d/h = 20$. This is because larger pressure drop leads to the increase of the maximum fluid velocity and Mach number. Mach number is related to lattice spacing. Then the decrease of the lattice spacing is to reduce the Mach number and to assure the fluid incompressible. The same simulations are also investigated with the CFD software. Second case, we impose a constant velocity on the cylinder as illustrated in Fig.2.17. The velocity condition is imposed on the wall $u_x = u_y = 0$. The system is initially at rest. Periodic condition for fluid and cylinder are used. At $t = 0$, cylinder moves with a constant velocity. Then drag coefficient with different velocities is computed.

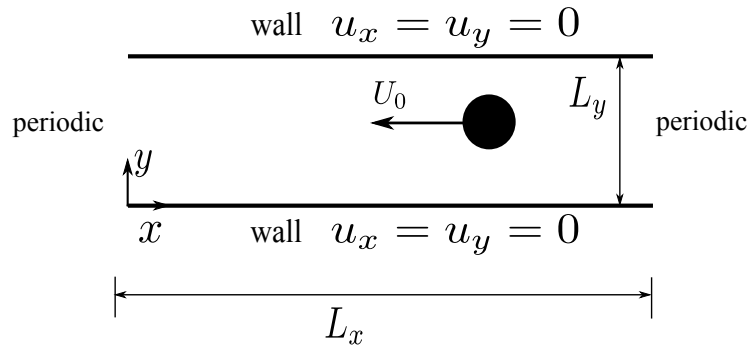


Figure 2.17: Schematic view of cylinder moving with a constant velocity applied and boundary condition.

The curve representing the evolution of the drag coefficient as a function of Reynolds

Table 2.10: Parameters used in the simulation of the cylinder moving with constant velocity

Channel length, L_x	0.05	[m]
Channel height, L_y	0.008	[m]
Cylinder diameter, d	0.001	[m]
Pressure drop, Δp	0.001, 0.01, 0.02, 0.03, 0.05, 0.1, 0.2, 0.3, 0.4, 0.5, 1	[Pa]
Fluid kinetic viscosity, ν	10^{-6}	[m ² /s]
Fluid density, ρ	10^3	[kg/m ³]
Relaxation time, τ	0.6	[-]
Lattice spacing, h	5×10^{-5}	[m]

number is used. The Fig.2.18 presents the numerical results obtained with LBM-DEM and CFD software respectively for $C_D = f(Re)$. It is observed that the drag coefficient of cylinder obtained using LBM-DEM agrees well with the CFD software for fixed cylinder. For the moving cylinder, the drag coefficient can be satisfied for LBM-DEM even though there exists small difference.

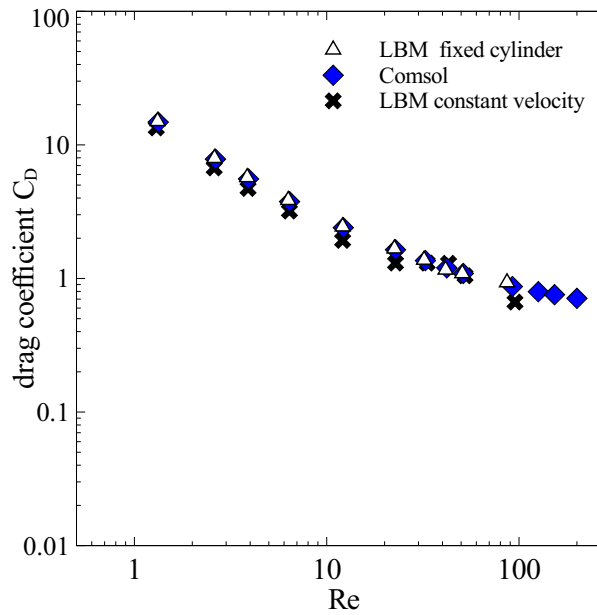


Figure 2.18: Drag coefficient as a function of Reynolds number of cylinder

2.6 Conclusion

This chapter presented the numerical method used in this work to simulate fluid and particle flow in porous media. The fluid flow is calculated using LBM and the particle transported by fluid is simulated by DEM. A series of classical fluid mechanics examples are presented to validate the computation code, such as Poiseuille flow, Couette flow, flow around a fixed cylinder in 2D and in porous media. These simulations results agree well with the analytical solutions. The validation of filtration problems will be presented in chapter 3 and 4. After validating the computation code, the particle transport and deposition in a filter is investigated using LBM-DEM in following chapter.

Chapter 3

Numerical simulation of particle capture on single fiber

3.1 Introduction

The knowledge of behavior of particles during their transport and deposition, on various fibers placed in a fluid flow, can provide important information for many environmental and industrial applications. The underlying physics of particle filtration process in filter is important [146]. Since single fiber is the basic element to constitute a filter, it is necessary to understand particle behavior in filter with single fiber during filtration process. Actually, single fiber can be made of a variety of shapes such as circular, diamond and square etc. The shape of fiber considerably affects the distribution of fluid field. The velocity and position of solid particle in filter rely evidently on the fluid velocity field. Thus, it is essential to acquire an accurate velocity field for particle trajectory analysis which is appropriately described by the Lagrangian approach. Conventional CFD model, based on the incompressible Navier-Stokes equation, combined with Lagrangian approach are usually used to simulate the fluid-solid flow within porous media such as filters [38, 147, 148]. For dilute suspension, the solid particle is viewed as mass point without volume (point-like approach), therefore the trajectory and velocity of the particle are calculated from the equation of the motion using Lagrangian approach by consideration of the different external forces such as drag force and Brownian force [47]. As presented in part 1.4 of chapter 1, it is reasonable to neglect the effect of particle on the fluid flow when the particle-laden flow are dilute enough ($\Phi_p \leq 10^{-6}$) [74], the error caused by this assumption is believed to be limited since the results in the validation are acceptable [149]. Based on these information, obviously,

point-like approach can estimate the actual displacement of particle within a time step. However, particle with large size ($d_p \geq 10 \mu\text{m}$) injected in fluid channel can change and affect significantly the flow field. In this case the volume of the particle and its influence on the flow field should be considered.

In this chapter, in a first part, we investigate the effect of particle size d_p and Stokes number St on the particle capture efficiency using two methods. The first one is one-way coupling combining lattice Boltzmann method (LBM) with Lagrangian point-like approach. The second one is two-way coupling based on the coupling between lattice Boltzmann method and discrete element method (DEM), which consider the particle influence on the fluid. Due to this consideration, the two-way coupling approach may be more suitable to study the transport problems for relative large particle. Therefore, we focus on the study to find the critical particle size between one-way and two-way coupling methods. In a second part, the single fiber capture efficiency characterized by Stokes number (St) and quality factor defined in chapter 1 part 1.3.2 are simulated by LBM-DEM. The effect of geometries of fiber on the filtration performance is also considered such as diamond, square and rectangular.

3.2 One particle injection

In this part of the work, the particles are injected one by one into the system, which means that the particle can be injected as soon as the previous one captured by the fiber or flows out from the filter. Particles are removed out from the flow field once they are captured by the fiber or flow out from the filter. Therefore, each particle moves alone, there is no inter-particle interaction in the fluid flow and the fiber stays clean .

3.2.1 Model description

The schematic view of computational domain of simulation is illustrated in Fig.3.1. A circular fiber of diameter D_f is introduced in computational domain. The fluid flows in x direction from left (inlet) to right (outlet). A constant velocity $\vec{U}_0 = \begin{pmatrix} u_{0x} \\ 0 \end{pmatrix}$ is imposed at inlet and outlet. When steady state of fluid velocity field is reached, small particles with diameter d_p are injected at the inlet. Eq.(3.1) is used to calculated the error of the fluid

velocity field. We considered that a steady state is established when $err < 10^{-5}$.

$$err = \frac{\sum_{i,j} |u_{i,j}(t + dt) - u_{i,j}(t)|}{\sum_{i,j} |u_{i,j}(t + dt)|} \quad (3.1)$$

where $u_{i,j}$ is the fluid velocity of node. We investigate particle capture efficiency with first a one-way coupling method, that will be described hereafter.

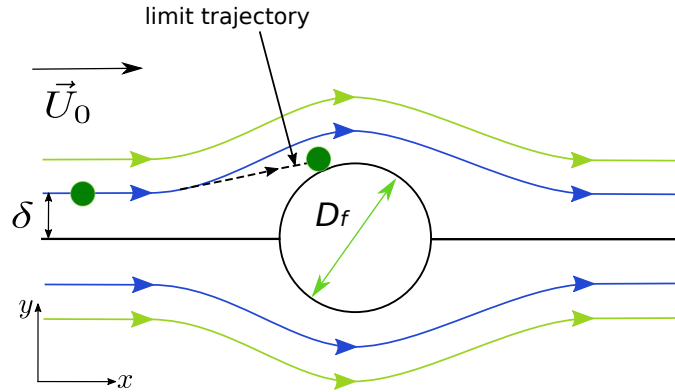


Figure 3.1: Particle trajectory and deposition on a single fiber.

The limit trajectory of the particle deposited on the fiber surface is sketched as mentioned in Fig.3.1. The particle released distance to the lattice axis is called δ . Thus, since the flow is symmetric, we define the fiber capture efficiency according to definition given in part 1.3.5 of chapter 1 as:

$$\eta_s = \frac{2\delta}{D_f} \quad (3.2)$$

3.2.2 One-way coupling

With one-way coupling method a solid particle is simply viewed as a point. In other words, the fluid does not see the particle and is therefore not affected by its presence. For this reason, when the fluid velocity field reaches a steady state, it remains unchanged until the end of the simulation. The velocity and trajectory of a particle is directly calculated by the traditional point-like approach tracing individual particle in the Lagrangian frame [149, 75]. Moreover, with this method there is no particle-particle interaction. Each particle is treated as if it were an isolated one. This assumption is reasonable when the volume fraction of solid particles is less than 10^{-6} [74, 150] as presented in Fig.1.17 in Chapter 1.

The one-way coupling algorithm can be described as follows. Firstly, the stationary

solution of fluid flow velocity field is computed. Then, each solid particle is injected at the inlet of the domain. Its initial velocity along the flow direction is set to be equal to the fluid velocity at that position. In this subsection, the fluid velocity field is computed with the LBM presented in chapter 2 and streamfunction presented in part 1.2.3.3 of chapter 1 respectively, and coupled with the particle motion dynamics.

3.2.2.1 Particle motion of equation

Inertial impaction is one of the major mechanisms in the particle-laden flow. The inertial effect in particle capture, shown in Fig.3.1, can be quantified by the dimensionless Stokes number [148, 47]. Stokes number has crucial effects on inertial-interception-dominated capture efficiency which has been described in chapter 1. Generally speaking, the particle with large size have a larger St number, (i.e., $dp > 10 \mu\text{m}$ [47, 112] and the inertial impaction dominates).

When a spherical particle moves with velocity u_p in a fluid stream moving with the velocity u , in the absence of any other external force, just by considering the drag force, given by the Stokes law, the equation of particle motion is expressed as:

$$\frac{4}{3}\pi\rho_p R_p^3 \frac{d\vec{u}_p}{dt} = 6\pi\mu R_p (\vec{u} - \vec{u}_p) \quad (3.3)$$

We use the dimensionless form by using U_0 :

$$\vec{u}_p^* = \frac{\vec{u}_p}{U_0} \quad (3.4)$$

$$\vec{u}^* = \frac{\vec{u}}{U_0} \quad (3.5)$$

$$t^* = \frac{t}{\frac{D_f}{U_0}} \quad (3.6)$$

where the superscript $*$ denotes the dimensionless quantity. Using these dimensionless quantities lead to following equations [14]:

$$St \frac{d\vec{u}_p^*}{dt^*} = \vec{u}^* - \vec{u}_p^* \quad (3.7)$$

$$\frac{d\vec{x}_p^*}{dt^*} = \vec{u}_p^* \quad (3.8)$$

A fourth order Runge-Kutta (RK) has been used to numerically solve the equations

(3.7) and (3.8). When new particle position is found, we compute the fluid velocity \vec{u}^* at this new position and again we solve equations (3.7) and (3.8). Therefore, it is possible to compute all injected particle trajectories.

3.2.2.2 Particle trajectory analysis

The transport of particle in fluid and its trajectory are analyzed. In 2D case, particles that come closer than distance $(D_f + d_p)/2$ from the fiber center are considered as trapped by the fiber and are then removed from the simulation. With this consideration, we estimated particle capture efficiency using equation (3.2).

The first one-way coupling method coupled the analytical solution (Kuwabara solution) for fluid velocity field and particle motion of equation (3.7) and (3.8) solved by Runge-Kutta, we call it Kuwabara-RK, whereas the second one is the LB-RK, in which the fluid velocity field is obtained with LBM. The results obtained by the Kuwabara-RK and LB-RK are compared each other. When the flow field is solved using LBM, it is worth to note that the solid particle is not constrained to locate only at the same lattice nodes as the fluid particles of the LBM. Because the velocity field of fluid in LBM is discrete, only the lattice nodes have the value information of the fluid velocity. Thus the fluid velocity \vec{u}^* at the location of the solid particle $r_p^{\vec{}}$ is solved using bilinear interpolation among the four closest nodes of the lattice. As seen in Fig.3.2, the blue and red circles represent the positions of fluid particles and the solid particle, respectively. The expression of the fluid velocity inside the lattice is given by:

$$\vec{u}^*(x_p, y_p) = \frac{y_{j+1} - y_p}{y_{j+1} - y_j} \vec{u}^*(x_p, y_j) + \frac{y_p - y_j}{y_{j+1} - y_j} \vec{u}^*(x_p, y_{j+1}) \quad (3.9)$$

where $\vec{u}^*(x_p, y_j)$ and $\vec{u}^*(x_p, y_{j+1})$ are:

$$\vec{u}^*(x_p, y_j) = \frac{x_{k+1} - x_p}{x_{k+1} - x_k} \vec{u}^*(x_k, y_j) + \frac{x_p - x_k}{x_{k+1} - x_k} \vec{u}^*(x_{k+1}, y_j) \quad (3.10)$$

$$\vec{u}^*(x_p, y_{j+1}) = \frac{x_{k+1} - x_p}{x_{k+1} - x_k} \vec{u}^*(x_k, y_{j+1}) + \frac{x_p - x_k}{x_{k+1} - x_k} \vec{u}^*(x_{k+1}, y_{j+1}) \quad (3.11)$$

The trajectory of particle during their transport in fluid are calculated. Fig.3.3 presents the trajectory of particle and the corresponding streamlines for different Stokes numbers. For $St = 0.001$, since the inertia of particle is weak, the trajectories of the dispersed particles basically correspond to the fluid streamlines and almost follow the fluid streamlines

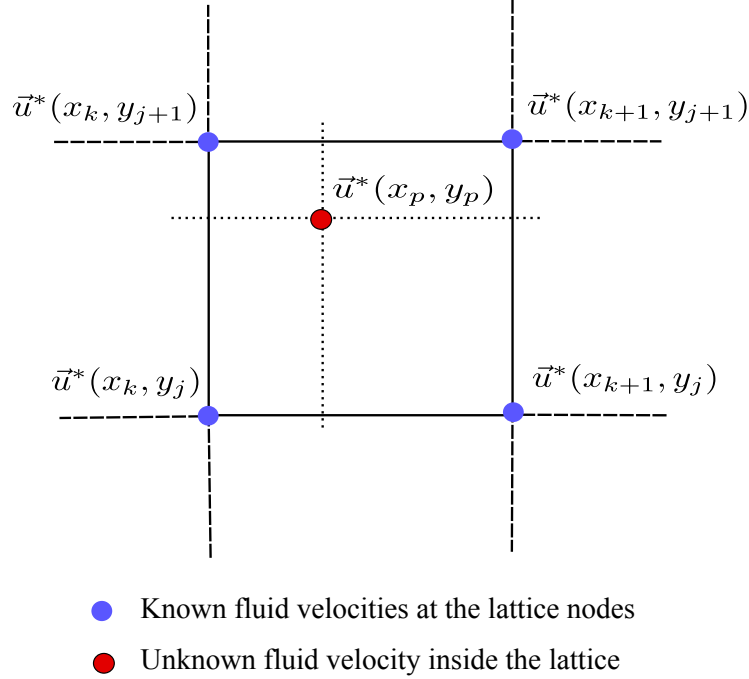


Figure 3.2: Schematic drawing of fluid velocities at one lattice in LBM.

closely. As a consequence, particle is not captured by the fiber. For $St = 0.03$, the trajectories of particle still follow the streamlines at upstream of fiber. However, the particle starts to deviate from streamlines after passing the fiber. This is because the inertia of particle increased at top of fiber as shown in Fig.3.3b. When St increases to 0.3, particle transports near to the fiber, but it cannot be captured by the fiber. As St increases ($St = 0.5$), particle follows slightly the fluid streamlines at several time steps and then deviates from it. The reason is that the inertia of particle with $St = 0.5$ is not intense enough at initial, but it is strong enough to be captured by fiber. When St is sufficiently large (i.e. $St = 1, 1.5$), inertial impaction mechanism becomes more and more stronger. Particle deviates from the corresponding streamlines during they approach the fiber and finally deposits on the surface of the fiber.

The numerical results are compared with the work of Araujo et al. [148] who obtained these results using the Kuwabara-RK. The fiber capture efficiency obtained by LB-RK and Kuwabara-RK is presented in Fig.3.4. From Fig.3.4 we can conclude that fluid velocity field obtained using LBM combined with bilinear interpolation is good enough to reproduce previous results presented in literature. These series of simulations validate our LBM code and the one-way coupling approach.

Obviously, as stated in references [151, 152, 2] and presented in section 1.4, the use

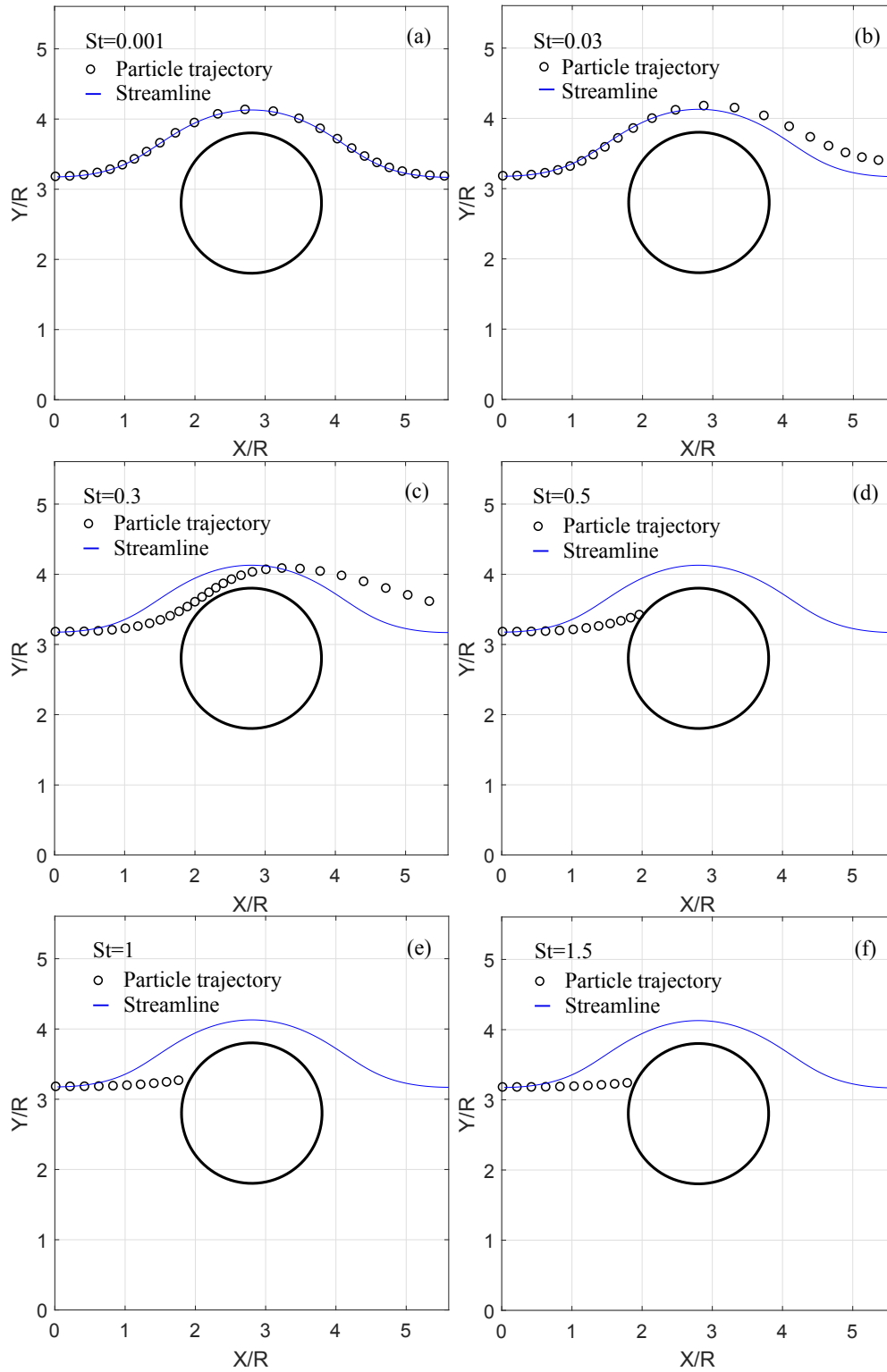


Figure 3.3: Particle trajectories with the corresponding streamlines around the fiber for (a) $St = 0.001$, (b) $St = 0.03$ (c) $St = 0.3$, (d) $St = 0.5$, (e) $St = 1$, (f) $St = 1.5$.

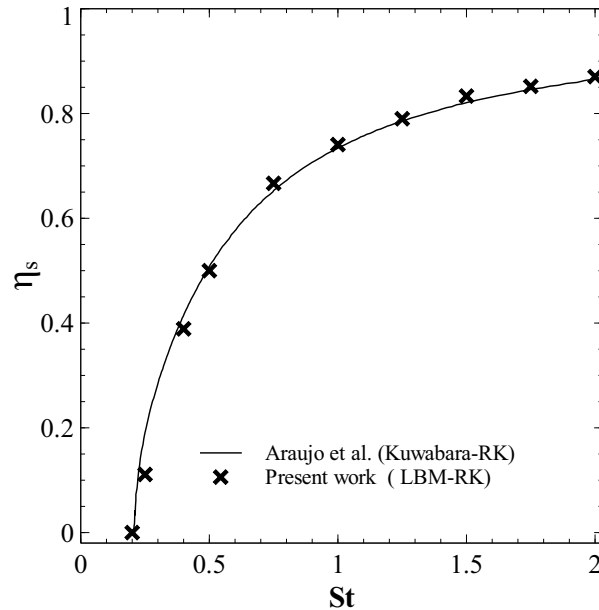


Figure 3.4: Particle capture efficiency on fiber as a function of the Stokes number St . The result is compared with the work of Araujo et al [148].

of one-way coupling method to investigate particle capture efficiency is reasonable only if particle effect on fluid flow can be neglected.

3.2.3 Two-way coupling

In this part, we use the two-way coupling method (LBM-DEM) to examine the particle transport and deposition. The idea is to investigate if the effect of the particle on fluid flow can still be neglected for relatively large particle. In this method, the particle is viewed as an object with its own boundary, which is seen by the fluid as a no-slip boundary condition. The fluid force and torque acting on the particle are directly computed through summation of momentum transfer over the particle surface (equations 2.65 and 2.66) and applied on it with equations 2.67 and 2.69.

3.2.3.1 The effect of particle size

To investigate particle size on particle capture efficiency, various simulations with different particle diameters ($8 \mu\text{m}$, $10 \mu\text{m}$, $12 \mu\text{m}$, $14 \mu\text{m}$, $16 \mu\text{m}$ and $18 \mu\text{m}$,) are performed. The results of particle capture efficiency are compared with those obtained with one-way coupling method (Fig.3.5).

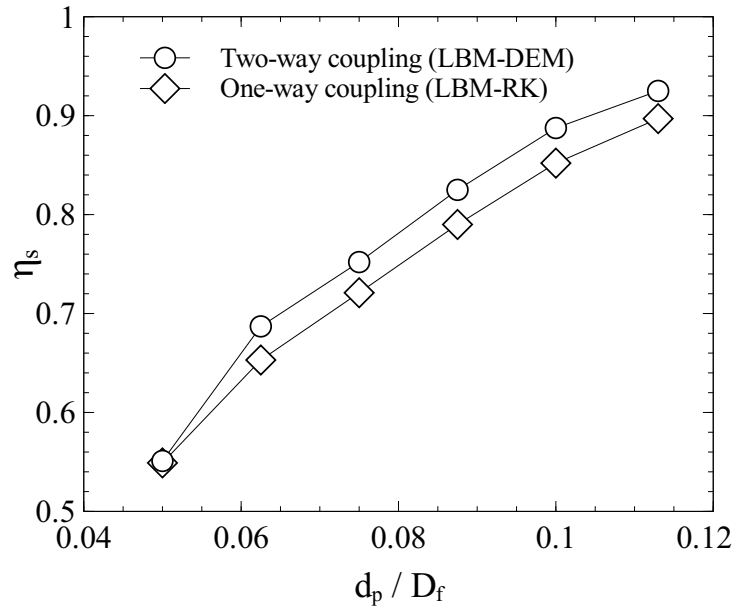


Figure 3.5: Single fiber capture efficiency as a function of ratio between the particle diameters d_p and fiber diameter D_f obtained from one-way and two-way coupling methods, respectively.

When the solid particle size is small ($d_p < 8 \mu\text{m}$ for our model), volume of particles have little effect on single fiber capture efficiency. However as the particle size increases, the effect of particle volume on the capture efficiency becomes much more obvious. Therefore, it can be stated that one-way coupling method is not appropriate in our case for $d_p > 8 \mu\text{m}$, and corresponding Stokes number of the particle is $St = 0.9$.

3.2.3.2 The effect of fiber shape

Three types of fiber with different cross-section, circular, diamond and square, are considered to study the capture efficiency for one particle injection. The solid particle size used in the simulation is $d_p = 10 \mu\text{m}$. In order to compare the capture efficiency for circular, diamond and square fiber respectively, the projected area of three fibers perpendicular to the flow direction are selected as characteristic length which are all equal to $D_f = 1.6 \times 10^{-4}\text{m}$. They keep constant during the simulation. For diamond fiber, it is a square rotated by $\pi/4$ with a diagonal D_f . The circular, diamond and square fiber are located at the middle of the computational domain with length L and width H as shown in Fig.3.6. A periodic boundary condition is imposed on the left and right sides. A constant velocity $\vec{U}_0 = \begin{pmatrix} 0 \\ u_0 \end{pmatrix}$ ($u_0 = 0.67\text{m/s}$) is applied at the inlet and outlet. The fluid density and kinematic viscosity are 1.2 kg/m^3 and $1.57 \times 10^{-5}\text{m}^2/\text{s}$ respectively. The Reynolds number is $Re = \frac{U_0 D_f}{\nu} = 6.8$.

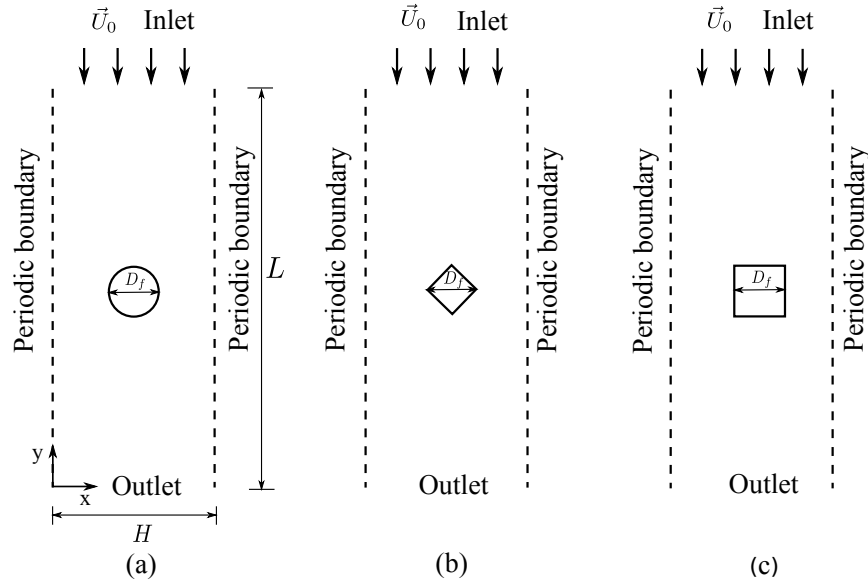


Figure 3.6: Schematic view of structure of (a) circular fibers (b) diamond fibers (c) square fibers.

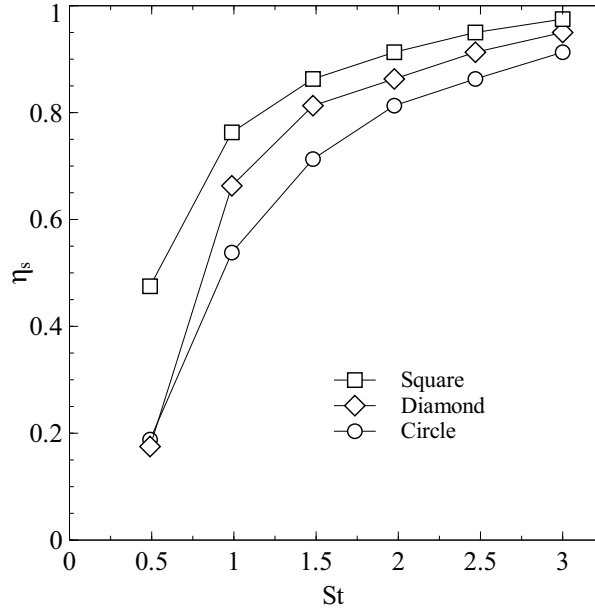


Figure 3.7: Single fiber capture efficiency of isolated particle for fiber with three different shapes.

The capture efficiency of circular, diamond and square fiber as a function of St is calculated with Eq.(3.2) and results are plotted in Fig.3.7 for isolated particle injection. We vary the particle density to change Stokes number in simulation. Fig.3.7 displays that the capture efficiency of diamond is closer to that of circle for $St = 0.5$. As St increases, the difference varies obviously. However, the capture efficiency of square fiber is more important than those of circular and diamond fiber for $0.5 \leq St \leq 3$. This is because the streamline close to the square are more curved as shown in Fig.3.8. The trajectories of the particle with corresponding streamlines around the three shapes of fiber are also presented for $St = 1$. The streamlines approach to the fiber are different for circular, diamond and square cases, which shows that the flow field is affected by fiber shape. Generally speaking, we can conclude that the square case have more chance to capture the particle.

3.2.3.3 Quality factor of filter

The capture efficiency of circular, diamond and square fiber have been analyzed. In order to judge the performance of filter with single fiber, we use the quality factor (or the figure of merit) which is presented in chapter 1:

$$QF = \frac{-\ln(1 - \eta)}{\Delta p} \quad (3.12)$$

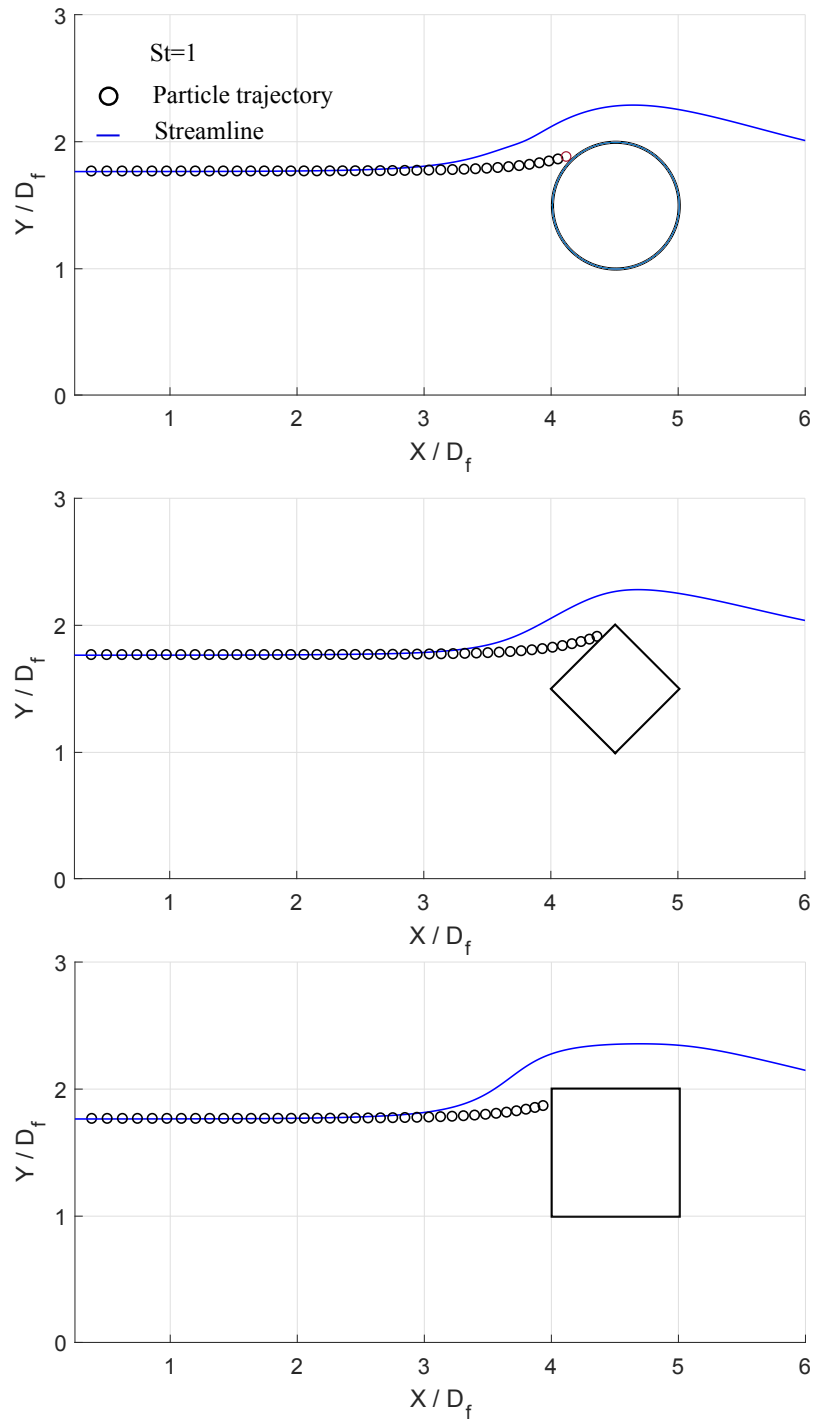


Figure 3.8: Trajectories of particle with streamlines for circular, diamond and square fiber

According to references [11, 153], it could be derived as follows:

$$QF = \frac{\eta_s}{(1 - \beta) \cdot (F^*/Re) \cdot (\rho U_0^2)} \quad (3.13)$$

β is fiber volume fraction which is calculated as the ratio of volume occupied by fiber to the volume of total computational region. F^* is dimensionless drag force applied on the fiber, the value is presented in Table 3.1.

Table 3.1: Dimensionless force applied on the fiber

F^*	Circular	Diamond	Square
	29.2	24.9	38.5

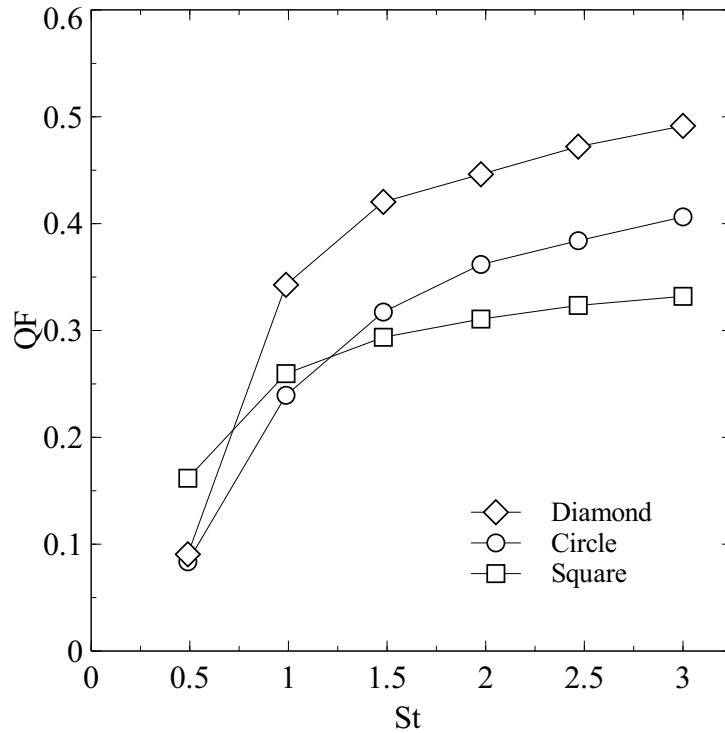


Figure 3.9: Quality factor as function of St for isolated particle injected.

Fig.3.9 presents the quality factor of filter with circular, diamond and square fiber with various Stokes number for isolated particle injected. It demonstrates that St affect the quality factor. Quality factor for circular, diamond and square fiber increases with St . Square fiber has better performance than the cases of circular and diamond fiber for $St < 1$. As St increases, the diamond fiber display higher quality factor for $St > 1$. Obviously,

although the square fiber exhibits the advantages in capture efficiency, a larger pressure drop for square fiber leads to its lower quality factor.

In the next section, we are interested in the study of single fiber capture efficiency and filtration efficiency of filter when several particles are present simultaneously in the fluid flow. The single fiber capture efficiency has been widely studied using one-way coupling method, even when relatively large number of particles were injected [151, 152, 113]. Since results presented in Fig. 3.5 illustrate that the effect of an isolated particle on fluid flow cannot be neglected for $d_p > 8 \mu\text{m}$ in our case, we can assume that it cannot be neglected when several particles are transported at the same time with such particle diameter. For this reason, LBM-DEM will be used to study the capture efficiency with $d_p > 8 \mu\text{m}$ in the rest of this chapter. Nevertheless, even if our coupled method can deal with inter-particle interaction, solid volume fraction used here is less than 10^{-3} . Therefore inter-particle interactions do not play an important role in this case.

3.3 Several particles injection

In this section we focus on the study of the capture efficiency with a number of solid particles injected ($d_p \geq 10 \mu\text{m}$) into the system. First, we consider single fiber capture efficiency. The injected particles are located in the projected area of single fiber at inlet. Then we investigate the filtration efficiency of filter which particles are injected at inlet of computational domain. Since the particle size used here is $d_p \geq 10 \mu\text{m}$, the Brownian diffusion is relatively weak, and the Brownian force on a particle is far less than the drag force exerted by the fluid [47]. For this reason, the Brownian diffusion is not considered in the simulation.

3.3.1 Particles injected at projected area of fiber

3.3.1.1 Model description

The two-dimensional computational domain, shown in Fig.3.10, is a rectangular one of length L and width H in which a circular fiber of diameter D_f is set on the center. The grid resolution for LBM, fixed here as $d_p/h = 10$, has been proved to be good enough to compute a reliable flow field and hydrodynamic force in chapter 2. A periodic boundary condition is applied on the left and right sides, both the fluid and solid particles flowing out from one side will enter into the domain from the other side. No-slip boundary condition

is imposed at the surface of the fiber. The condition for fluid is given by Eq (3.14). The constant velocity $\vec{U}_0 = \begin{pmatrix} 0 \\ u_0 \end{pmatrix}$ ($u_0 = 0.67\text{m/s}$) is applied at the inlet and outlet.

$$\begin{aligned} u_y(x, 0) &= u_0 \\ u_y(x, L) &= u_0 \end{aligned} \quad (3.14)$$

The fluid density and kinematic viscosity used here are 1.2 kg/m^3 and $1.57 \times 10^{-5} \text{ m}^2/\text{s}$ respectively. After the flow achieves a steady state (velocity vectors are shown in Fig.3.10), 500 particles are injected randomly in the projected area of fiber at the inlet of computational domain. The initial velocity of the injected particle is assumed to be equal to fluid velocity.

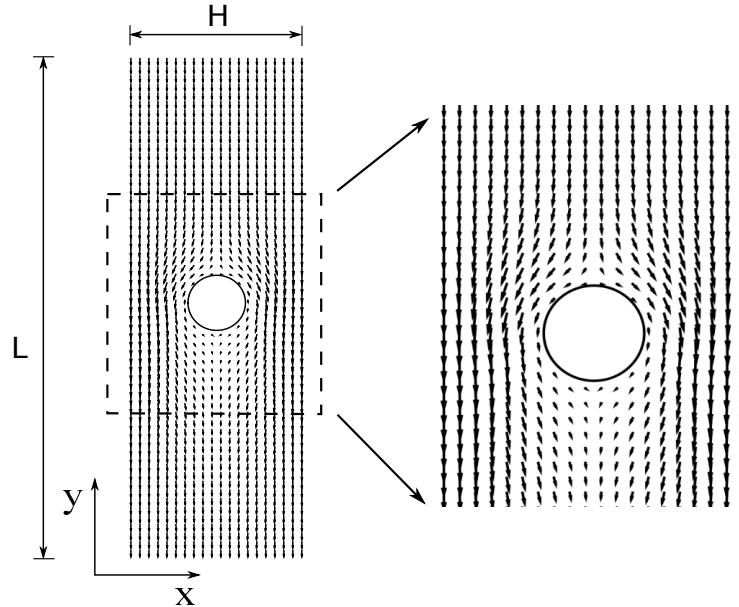


Figure 3.10: A steady state velocity vector of flow around a circular fiber calculated with LB method

3.3.1.2 Capture efficiency of circular fiber

As in section 3.2, the particles in the flow are assumed to be captured once they collide on the surface of the circular fiber. Then, collided particles are removed from the flow. The single fiber capture efficiency is defined as [69]:

$$\eta_s = \frac{N_{inject} - N_{escape}}{N_{total}} \quad (3.15)$$

where N_{inject} and N_{escape} represent the total number of solid particles injected in the projected area of the surface and removed from the outlet respectively.

Series of snapshots from one simulation of particle transport and deposition with coupled LBM-DEM are shown in Fig.3.11. It is seen that after injection of particles, the velocity field of fluid changes remarkably which, in turn, leads to the variation of the particle velocity and trajectory.

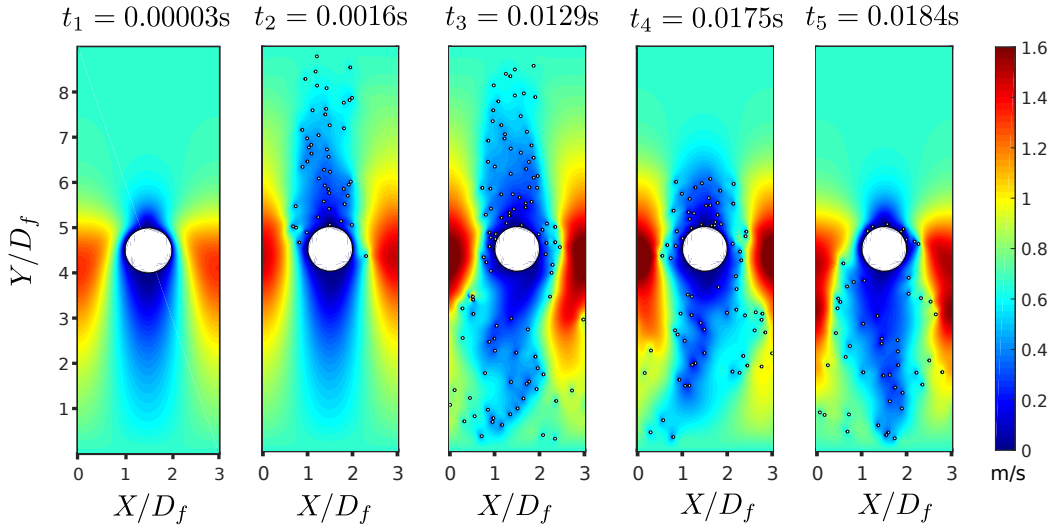


Figure 3.11: Velocity field of fluid and particle distribution for $St=0.5$.

Single fiber capture efficiency is also influenced significantly by the Stokes number. Several studies have been performed to predict single fiber efficiency resulting from the inertial impaction. Israel and Rosner [61] investigated the aerodynamic capture efficiency of non-Stokesian particles and determined the following expression for $St_{eff} > 0.14$:

$$\eta_s = [1 + 1.25(St_{eff} - 0.125)^{-1} - 1.4 \times 10^{-2}(St_{eff} - 0.125)^{-2} + 0.508 \times 10^{-4}(St_{eff} - 0.125)^{-3}]^{-1} \quad (3.16)$$

where $St_{eff} = G(Re_p)St$, Re_p is particle Reynolds number defined as $Re_p = \frac{U_0 d_p}{\nu}$, G is a function of Re_p . In our simulation, $Re_p = 0.425$ and $G(Re_p) = 0.95$. Eq (1.59) for single fiber efficiency which has been described in chapter 1 is also used here.

In order to examine the effect of St on the single fiber capture efficiency, we add another two cases for injecting 1000 and 1500 particles respectively to calculate the single fiber capture efficiency. A comparison between the single fiber capture efficiency obtained with LBM-DEM and the one obtained from the empirical relationships calculated according to

Eqs (3.16) and (1.59) has been made and presented in Fig.3.12. In our model, since the particle diameter is $d_p = 10 \mu\text{m}$, the fiber Reynolds number and intercept coefficient are $Re = \frac{U_0 D_f}{\nu} = 6.8$ and $R = \frac{d_p}{D_f} = 0.0625$ respectively. The single fiber capture efficiency is plotted as a function of St ranging from $0.5 < St < 3$. The results obtained with 500, 1000 and 1500 particles are nearly the same. Thus number of particle for 500 is enough to repeat the simulation results. Agreement between the simulation results and empirical formula Eq (1.59) is observed. However, with respect to Eq (3.16), we use $G(Re_p)St$ instead of St_{eff} in Fig.3.12, a small difference is found for $St > 1$ and significant difference is observed for $St < 1$.

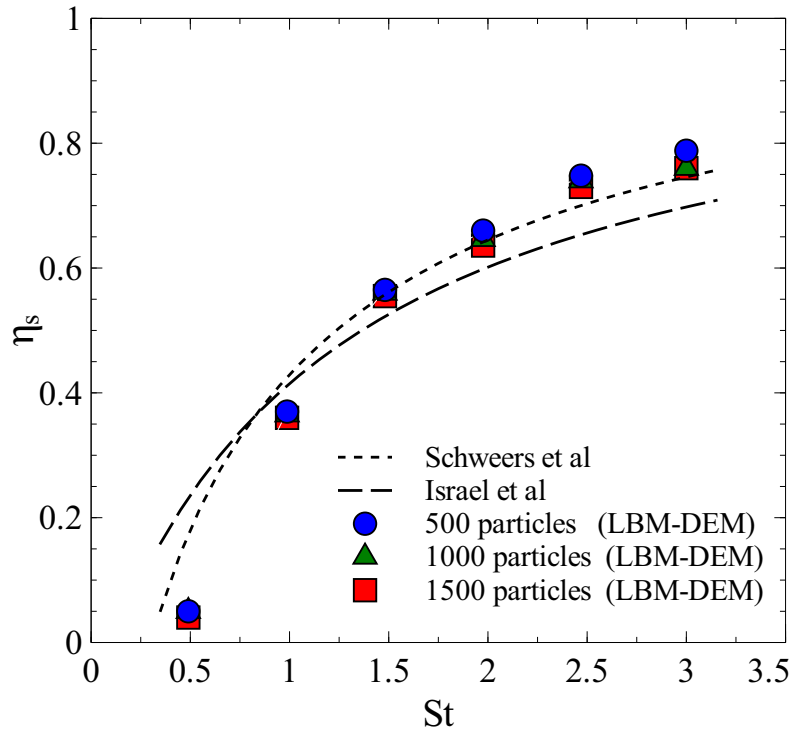


Figure 3.12: Comparison between capture efficiency of single circular fiber obtained from numerical method (LBM-DEM) and from the empirical correlations. $Re = 6.8$, $R = 0.0625$.

3.3.1.3 Capture efficiency of diamond and square fiber

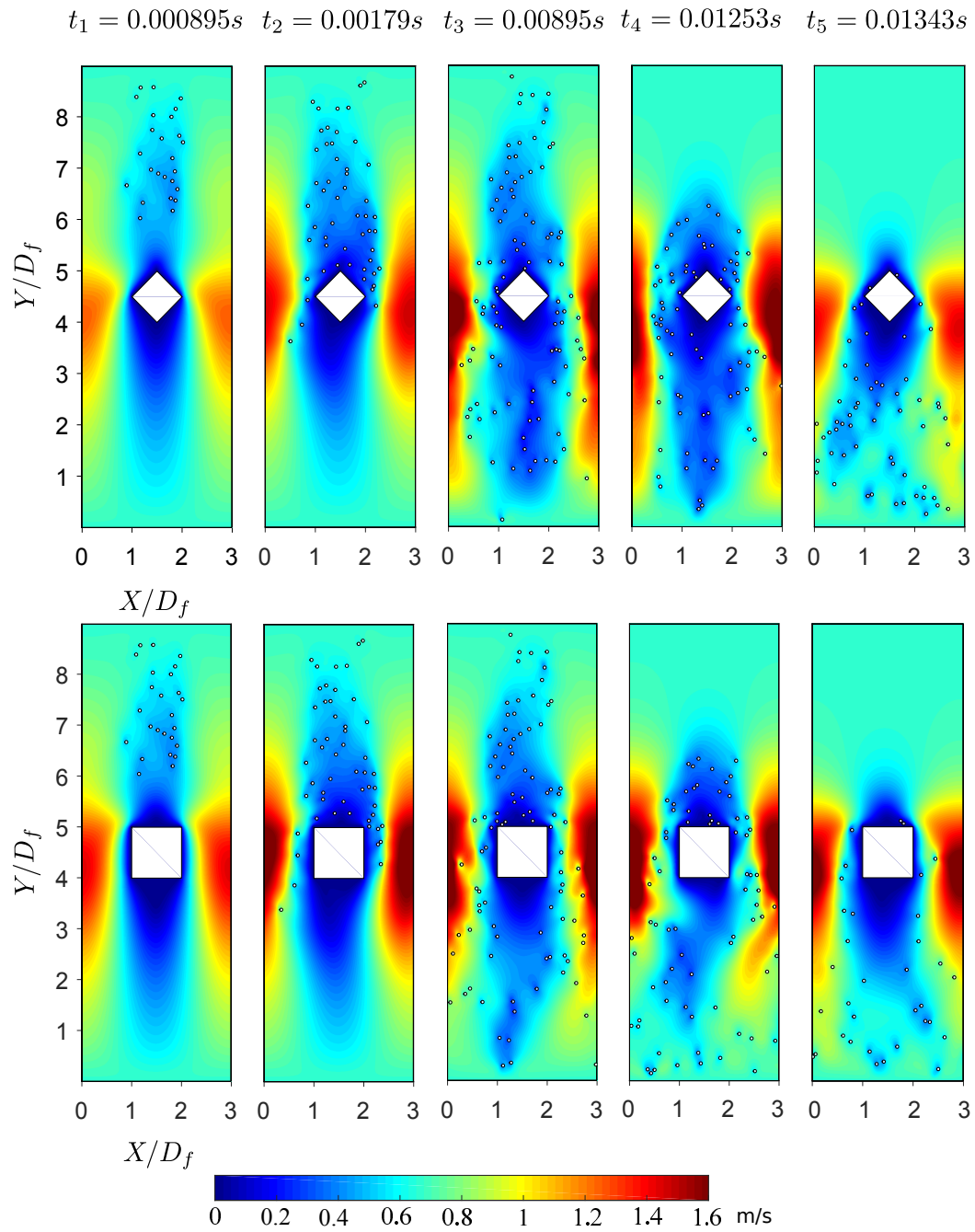
We investigate now the influence of the fiber shape on the single fiber capture efficiency. The simulations are conducted with two types of fibers, square and diamond respectively. In order to compare the capture efficiency with the circular fiber results, characteristic

length is selected as in section 3.2.3.2 (projected area perpendicularly to the flow direction). Except for the variation in fiber shapes, we use exactly the same operating conditions and values that the ones used in the circular case described in section 3.3.1.2. The projected area of diamond and square fiber is equal to that of the circular fiber.

Fig.3.13 presents the velocity field of fluid and particle distribution with diamond and square fibers. Particles are almost impacted on the front side of the fiber during their transport. This is because fiber Reynolds number $Re = 6.8$ is not large enough and the flow remains smooth with very little vortices observed behind the fiber. For the intermediate Stokes number ($0.5 < St < 1$), solid particles do not behave like the fluid particles any more. They are dominated by both the interception and inertial impaction mechanisms. On the other hand, particles with large Stokes number ($St > 1$) exhibit a strong inertial behavior, they are essentially unaffected by the flow. As a consequence, a large number of particles are collected on the front side of the fiber.

To investigate the distribution of captured particles on the surface of fiber. The front side of fiber is divided by 9 zones (1-9) shown in Fig.3.14, since the projected area of circular, diamond and square fiber are the same, here we take the diamond as example. Then the number of particles captured on the front side of fiber is counted. Fig.3.15 displays the results of single fiber capture efficiency in each zone for $St = 1.97$. For these three types of fibers, the single fiber capture efficiency at the middle of the fiber is nearly the same (part 5). The number of captured particles are approximately symmetrically distributed on the front side of the fiber.

We also examine the single fiber capture efficiency for different fiber shapes. A comparison among circle, diamond and square is presented in Fig.3.16. For the single fiber capture efficiency, there is no significant differences among these three fiber shapes when $St = 0.5$. This is because the single fiber capture efficiency is very weak. Araujo et al. [148] showed this existence of critical Stokes number, below which particles cannot be captured. The capture efficiency of diamond fiber is close to that of circular fiber as St is near to unity. As Stokes number increases, the square fiber has predominant preferences in particle collection. Generally, the number of collected particles on the front surface of square is greater than those of circle and diamond for different Stokes number. We also plot the single fiber capture efficiency for isolated particle in Fig.3.16 to compare with the one for several particles. The two cases are different as shown in Fig.3.16. For the same fiber shape and fixed St , the single fiber capture efficiency for several particles are smaller than the one for isolated particle. This is due to the fact that when several particles are injected,

Figure 3.13: Particles distribution with square and diamond fiber for $St = 0.5$.

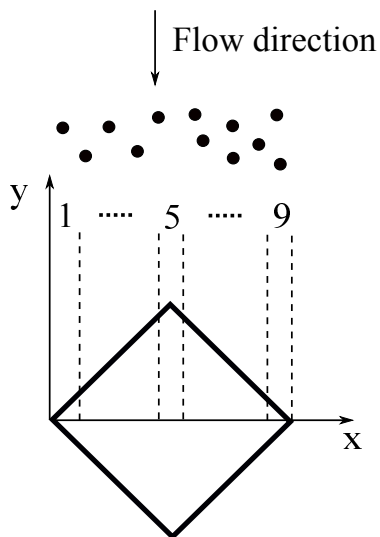


Figure 3.14: Front side of fiber is divided by 9 parts from 1 to 9.

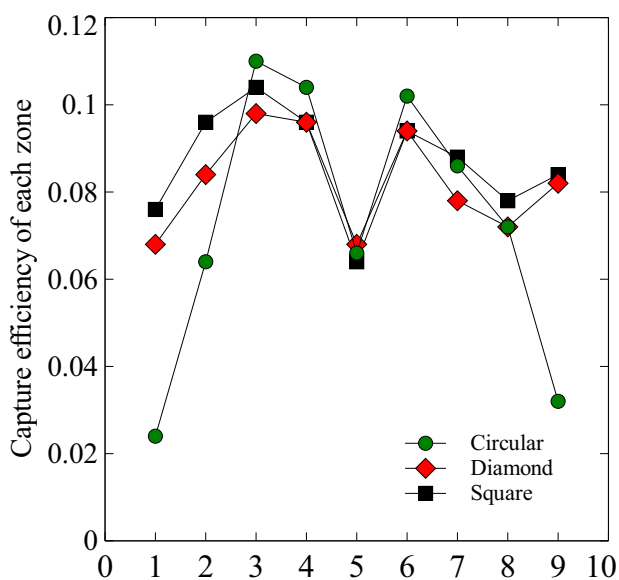


Figure 3.15: Particles distribution on the front side of circular, diamond and square fiber for $St = 1.97$.

the local Stokes is smaller due to the presence of other particles that greatly modify the fluid velocity field around the fiber.

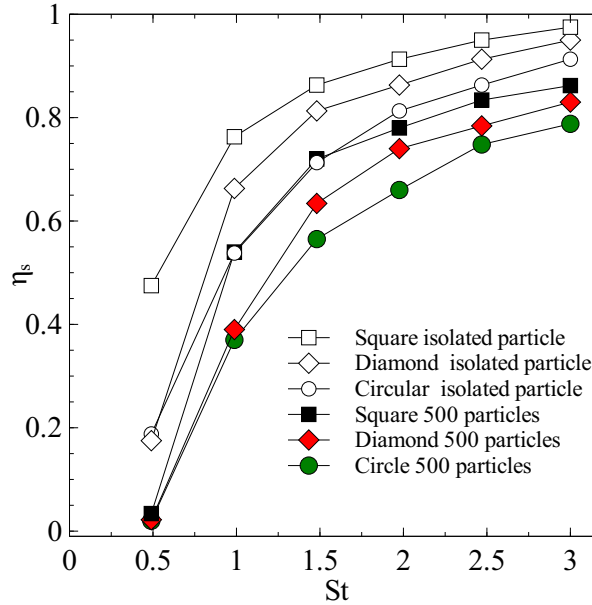


Figure 3.16: Single fiber capture efficiency as a function of Stokes number St with different fiber shapes.

3.3.1.4 Quality factor of filter for several particles injected

The quality factor is calculated for several particles injected. Fig.3.17 presents the performance of circular, diamond and square fiber with different Stokes number values. It demonstrates that the St affects the quality factor of these three fibers. Although the square fiber has a high capture efficiency, the pressure drop of circular and diamond fiber is lower than square case for $St > 1.5$. When considering these two parameters together, diamond fiber is at advantage of quality factor over the square and circular fiber. The quality factor for isolated particle injected is also presented in Fig.3.17. For the same fiber shape, the case of isolated particle generally keeps higher quality factor than the case of several particles for a fixed St . This is due to higher capture efficiency for the case of isolated particle while the same pressure drop.

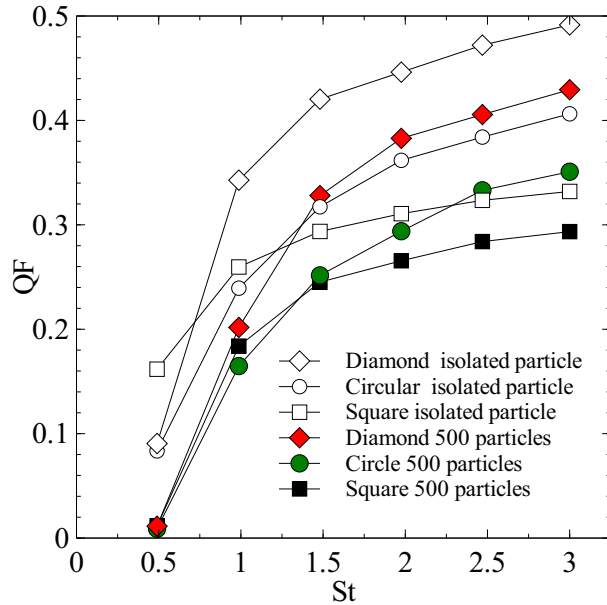


Figure 3.17: Quality factor as a function of Stokes number St with different fiber shapes.

3.3.2 Particles injected along whole inlet

In this section, the filtration efficiency of filter is considered, thus the particles are injected at whole inlet of computational domain. From the simulations presented above, we know that the geometries of fiber have considerable influence on the filtration performance. More specifically, diamond cross-section shape displays a better performance by comparison of square fiber, which promote us to investigate how the orientation angle and aspect ratio of rectangular fiber affect the filtration performance. Thus, in this section, we focus on the study of the effect of orientation angle and aspect ratio of rectangular fiber on pressure drop, filtration efficiency of filter and quality factor for various Reynolds numbers.

3.3.2.1 Model description

A schematic view of a periodic cell of the filter is illustrated in Fig.3.18. It also represents the computational domain of width H and length L . The block located at the center of the unite cell represents the cross-section of a rectangular fiber with orientation angle θ relatively to x axis. w and b are the width and length of fiber respectively.

A constant velocity $\vec{U}_0 = \begin{pmatrix} u_{0x} \\ u_{0y} \end{pmatrix}$ is applied at the inlet. At the outlet, we have imposed $\partial u_{0x}(x, 0)/\partial y = 0$ and $\partial u_{0y}(x, 0)/\partial y = 0$, where u_{0x} and u_{0y} are components of velocity

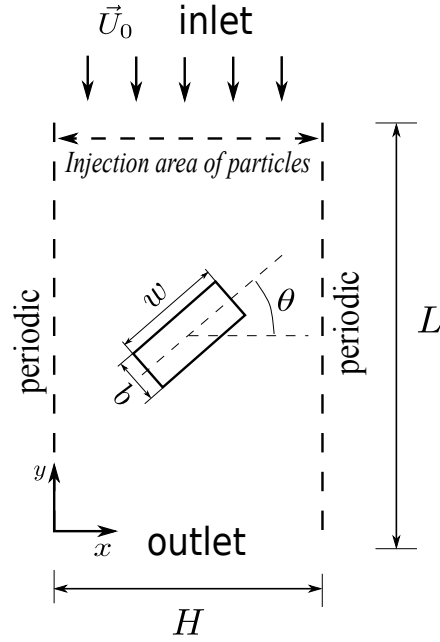


Figure 3.18: Schematic view of computational domain for simulating flow field around rectangular fiber.

vector \vec{U}_0 respectively along x and y direction. Both left and right sides of computational domain are periodic boundary conditions for both fluid and particles. Eq.(3.1) is used again to calculate the *err* of the fluid velocity field. We consider that a steady state is established when $err < 10^{-5}$. Then, a number of particles are randomly injected into the domain at the whole inlet (see Fig.3.18). The initial velocity of each injected particle is equal to the fluid velocity at this location.

As in section 3.3.1.2, particles that are not captured are removed when they escape from the outlet. As defined previously in section 1.3.3 of chapter 1, the filtration efficiency of filter can be obtained as follows:

$$\eta = \frac{N_{total} - N_{escape}}{N_{total}} \quad (3.17)$$

where N_{total} and N_{escape} represent the number of solid particles injected at the inlet and removed from the outlet.

Reynolds number is defined as $Re = U_0 D_h / \nu$, where ν is the fluid kinematic viscosity $1.57 \times 10^{-5} \text{m}^2/\text{s}$, D_h is the hydraulic diameter of the fiber equal to $2wb/(w+b) = 2 \times 10^{-4}$. Four different values of aspect ratio ($w/b = 1, 2, 3, 4$) are used in the simulations while keeping D_h constant. Five orientation angles ($\theta = 0, \pi/8, \pi/4, 3\pi/8, \pi/2$) are studied for

each aspect ratio. The solid volume fraction of the fibers is computed as $\beta = bw/(LH)$.

3.3.2.2 Pressure drop of clean filter

As expressed in chapter 1 part 1.3.7, pressure drop Δp between inlet and outlet of the periodic cell, which is related to drag force F_D on a unit length of single fiber, is a key parameter to evaluate filtration performance [58]. The determination of the dimensionless drag force $F^* = F_D/(\mu U_0)$ permits to calculate pressure drop, where μ is the dynamic viscosity, with the following relation:

$$\frac{\Delta p}{L} = \frac{F_D \beta}{bw} \quad (3.18)$$

Ouyang and Liu [154] determined dimensionless drag force for rectangular fiber with $\theta = 0$ in Stokes flow regime. It is worth noting that the volume fraction has also influence on the dimensionless drag force for rectangular fiber [114]. In order to compare with these results and to validate our model, we have plotted in Fig.3.19 the dependency of dimensionless drag force, obtained with our program, on volume fraction of fiber for different aspect ratios w/b and $Re = 0.2$ and more generally $Re < 1$ [154]. Fig.3.19 shows a good agreement that demonstrates that our model can be used to simulate the pressure drop of filter with rectangular fiber for low Reynolds number.

In previous works, many researchers choose generally the fiber Reynolds number less than 1 for fluid flow [152, 109]. As $Re < 1$, Liu and Wang [58] found that the dimensionless drag force is independent of Reynolds number for circular fiber. Furthermore, Fardi and Liu [114] concluded also that dimensionless drag force is relatively independent of Re for rectangular fiber. In this section, we focus on the study of the relationship between dimensionless force and Reynolds number for the case of $Re > 1$. To vary the Reynolds number, we have chosen to vary the fluid velocity at the inlet.

Fig.3.20 shows the dimensionless drag force F^* as a function of Reynolds number, varying from 2 to 10, with four typical aspect ratios and $\theta = 0$. As presented in Fig.3.20, F^* is influenced by Reynolds number and increased with it in the region of $2 \leq Re \leq 10$. When Re increases, the growth rate of F^* gradually enhanced for aspect ratio (w/b) from 1 to 4. Thus, Reynolds number has significant effect on the pressure drop for large value of aspect ratio. We know that a lower pressure drop across a filter is more favorable. Here at a fixed Reynolds number, it is obtained for rectangular fiber with a small aspect ratio (i.e., $w/b = 1$).

The streamlines around rectangular fiber with aspect ratio of $w/b = 2$ and different

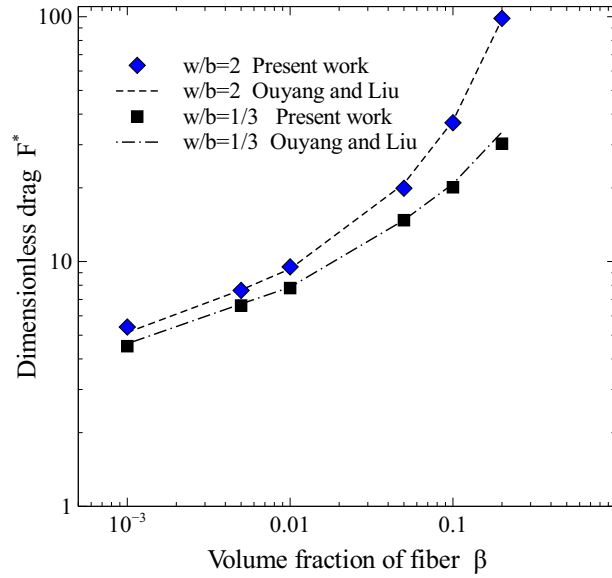


Figure 3.19: Dimensionless drag force as a function of volume fraction, LB simulation results are presented and compared with the work of Ouyang and Liu [154].

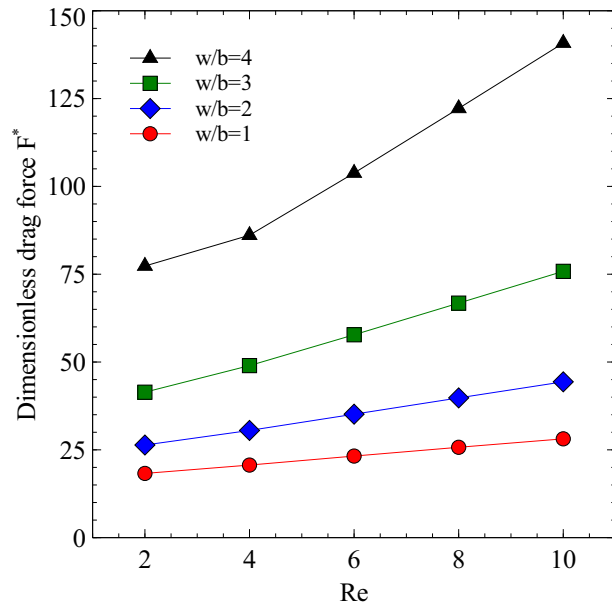


Figure 3.20: Dimensionless drag force as a function of fiber Reynolds number for $\theta = 0$.

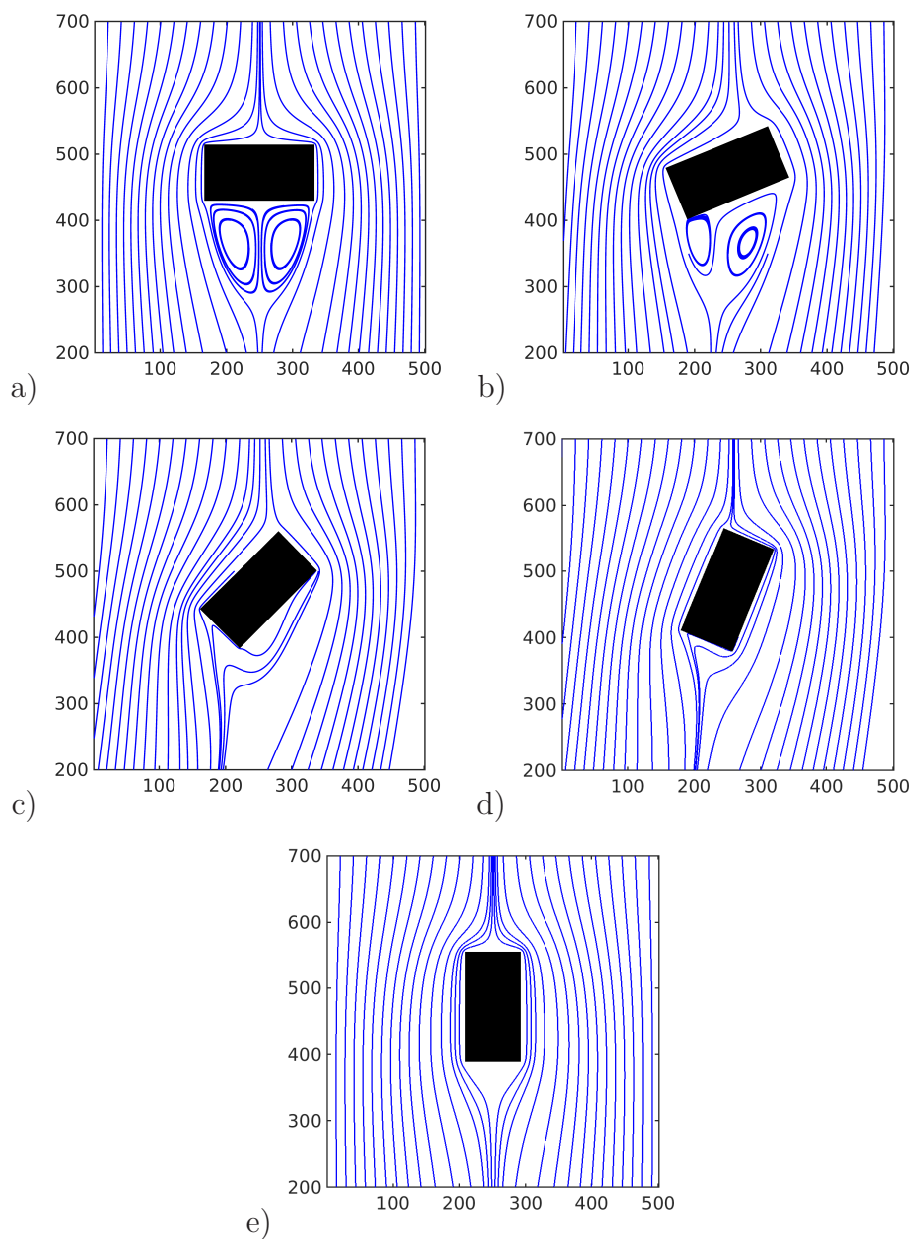
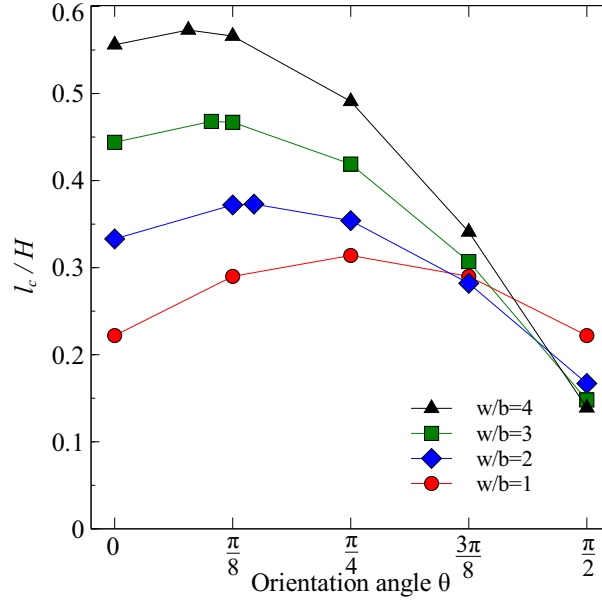


Figure 3.21: Streamlines around rectangular fiber with an aspect ratio of $w/b = 2$ and orientation angles (a) $\theta = 0$, (b) $\theta = \pi/8$, (c) $\theta = \pi/4$, (d) $\theta = 3\pi/8$, (e) $\theta = \pi/2$, $Re = 8$

Figure 3.22: Windward area with orientation angle θ

orientation angles are presented in Fig.3.21. It is obviously observed that the orientation angle of fiber modifies the flow field, which furthermore influences the pressure drop. The streamlines near the fiber change remarkably as the orientation angle decreases. Fig.3.22 shows evolution of windward area l_c , defined as:

$$l_c = w \cos \theta + b \sin \theta \quad (3.19)$$

which is represented in Fig.3.23. The maximum value of l_c for each aspect ratio is also plotted. Figures 3.24 shows the relationship between dimensionless drag force and orientation angle with different aspect ratios. It illustrates that when aspect ratio $w/b = 1$ (i.e., square), F^* is larger for $\theta = \pi/4$ than those of other angles due to the largest windward area in comparison with other angle values.

The maximum windward area l_c is $\arctan b/w$. However, F^* decreases with θ for other aspect ratios $w/b = 2, 3, 4$. The larger w/b is, the faster F^* decreases. It can also be noted that F^* at $\theta = \pi/2$ is lower than that at $\theta = 0$ for $w/b = 2, 3, 4$. The reason is that windward area of $\theta = \pi/2$ is much smaller than that of $\theta = 0$ as observed in Fig.3.22. Therefore, as θ increases, the windward area of rectangular fiber decreases, which allows the fluid to pass through filter more easily. It can also be noted, in Fig. 3.22 that values of l_c are quite similar for $\theta = 3\pi/8$ and $\pi/2$ leading to quite similar values of drag force as observed in Fig. 3.22. Based on this analysis, it is concluded that a larger θ with a smaller

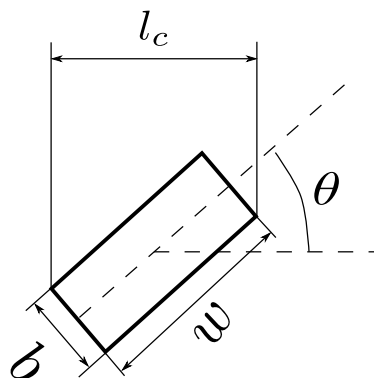


Figure 3.23: The cross-section area of rectangular fiber

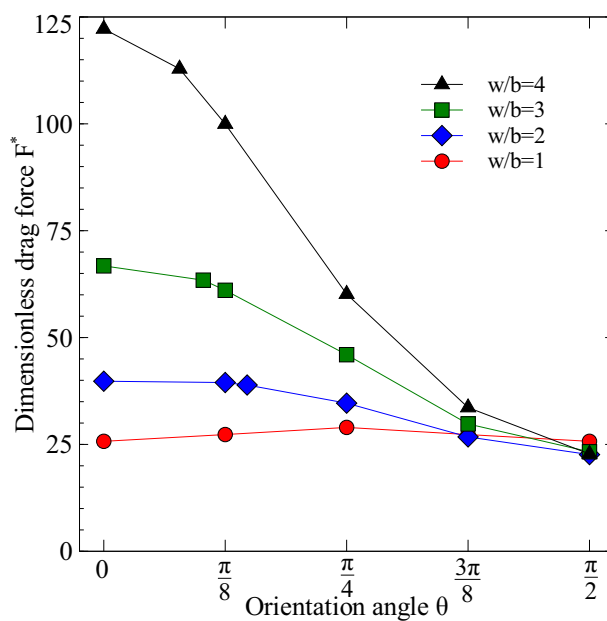


Figure 3.24: Dimensionless drag force as a function of orientation angle, $Re = 8$.

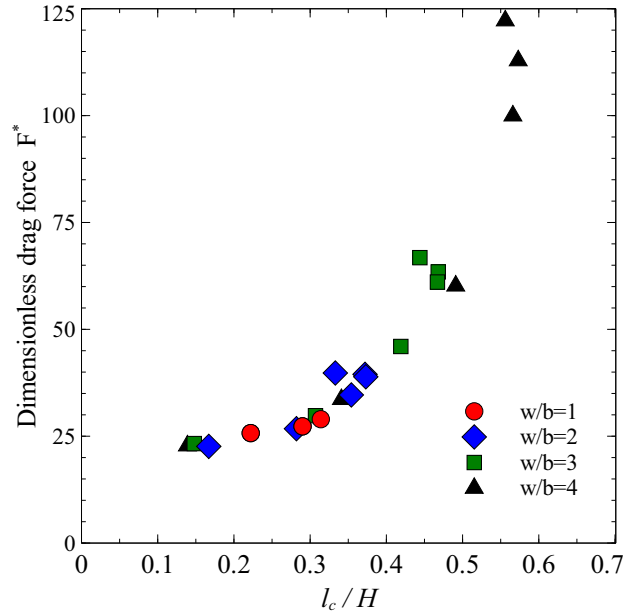


Figure 3.25: Dimensionless drag force as a function of cross section l_c , $Re = 8$.

windward area of rectangular fiber is more stable to obtain a lower pressure drop.

Figure 3.25 presents the same simulations results of Fig. 3.24 in terms of cross section l_c for all aspect ratios investigated. For l_c , we vary w and b in order to keep D_h fixed in the simulation. Figure 3.25 illustrates that drag force increase with l_c . In this analysis, we present the relationship between F^* and θ (or l_c) in the case where $b \leq w$. However, for the case of $b > w$ (i.e. $w/b = 1/2, 1/3, 1/4$), symmetrical results about $\theta = \pi/4$ with those of Fig.3.24 can be obtained, which are not demonstrated in this work.

3.3.2.3 Filtration efficiency of filter

Filtration efficiency, defined in Eq.3.17, is another important parameter used to assess the filter performance. As presented in 3.3.2.1, in the present simulations, 500 particles are randomly injected at the inlet, as illustrated in Fig.3.18, once the flow field reaches a steady state. The velocity and trajectory of solid particles depend obviously on the fluid velocity field, whose the regime is characterized by the Reynolds number. Thus, the relationship between filtration efficiency and Reynolds number is sought in Fig.3.26. It is shown that filtration efficiency varies slightly with the Reynolds number from 2 to 10 for a fixed aspect ratio and orientation $\theta = 0$.

The reason is that particles are mainly dominated by the inertial impaction, the particle Stokes number is $St = \rho_p d_p^2 U_0 / (18\mu D_h)$, where ρ_p is particle density. With our data, the

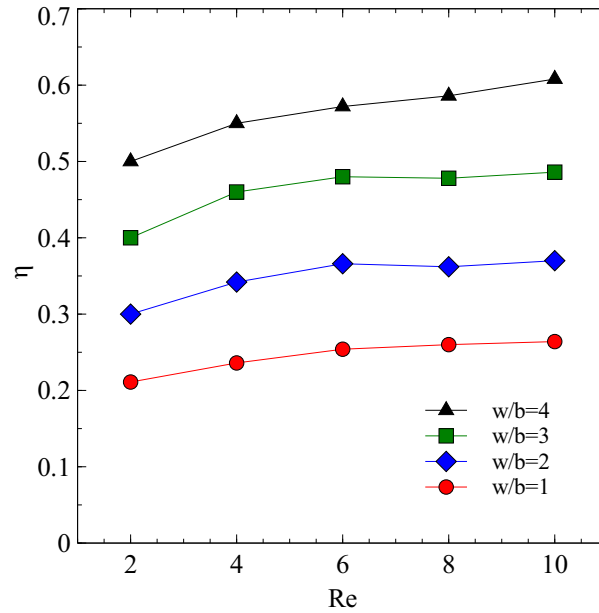


Figure 3.26: Filtration efficiency of filter as a function of Reynolds number for $\theta = 0$.

Stokes number is $2.08 \leq St \leq 10.4$. The injected particles at the upstream of the system exhibit large St behavior and are essentially uninfluenced by the flow. The injected particles deviate from the flow streamlines at first and after several time steps they do not follow them any more. For $Re = 10$, particles move straight ahead from inlet to outlet since they have a strong inertial force. For this case, Reynolds number does not have a significant effect on filtration efficiency. In the region of $2 \leq Re \leq 10$, rectangular fiber with a large aspect ratio (i.e large w) is more convenient to obtain a high filtration efficiency due to its large windward area.

The effect of orientation angle on the filtration efficiency is analyzed. Fig.3.27 depicts instantaneous image of velocity field of fluid and particle position for $St = 8.33$ with different orientation angles θ . It illustrates an obvious evidence that the particle transport affects the flow field. The link between fluid streamlines presented in Fig.3.21 and particle positions presented in Fig.3.27 shows that the particles do not follow the streamlines downstream of the fiber. As explained previously, this is due to the inertial regime characterized by large Stokes number used in our simulations.

Different orientation angles corresponding to the different cross-section area of fiber have significant influence on the filtration efficiency. In Fig.3.28, filtration efficiency of filter as a function of orientation angle is presented for $Re = 8$. We can easily recognize that the filtration efficiency of filter for square fiber ($w/b = 1$) at $\theta = \pi/4$ is higher than

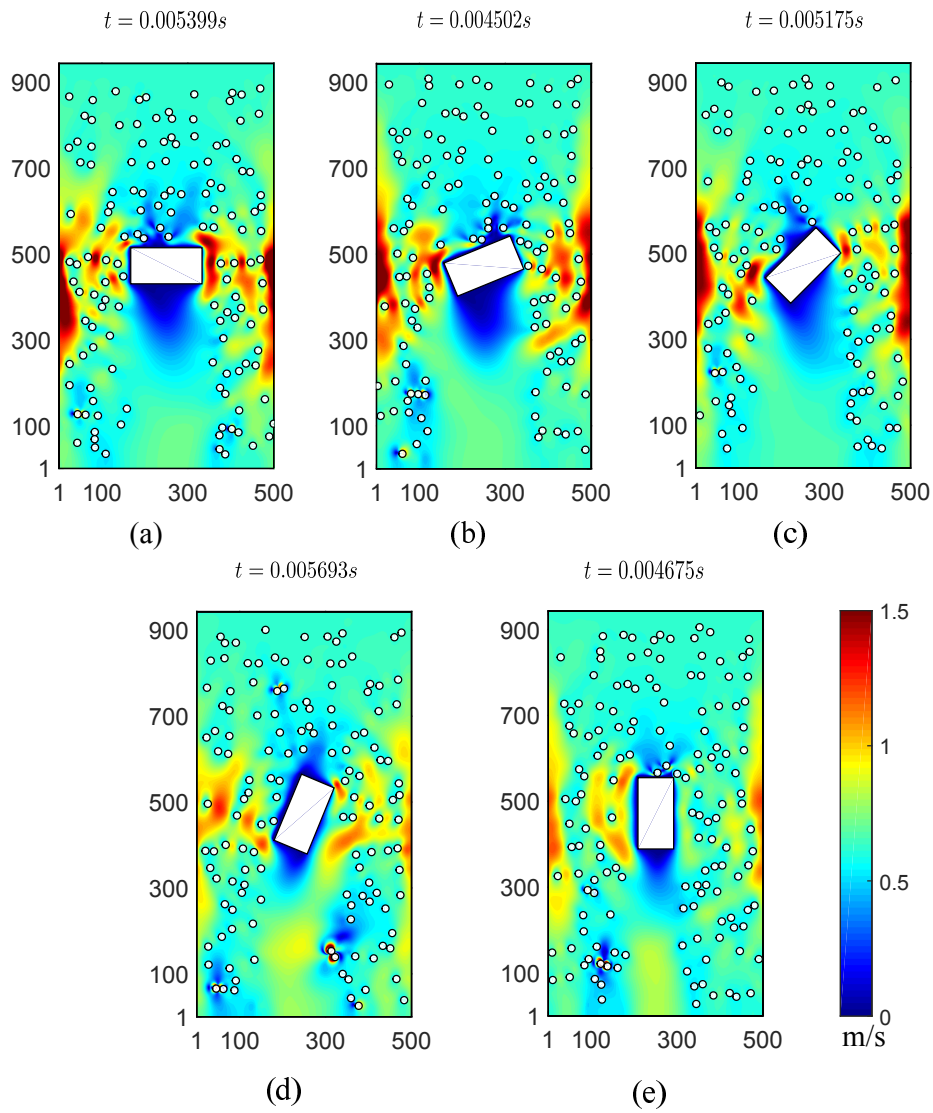


Figure 3.27: Velocity field of fluid and particle positions for $St = 8.33$, $Re = 8$, (a) $\theta = 0$, (b) $\theta = 1/8\pi$, (c) $\theta = 1/4\pi$, (d) $\theta = 3/8\pi$, (e) $\theta = 1/2\pi$.

that of other orientation angles, since l_c is maximum for this orientation angle. In addition, the value of filtration efficiency of filter for square fiber is symmetrical about $\theta = \pi/4$. For the aspect ratio of $w/b = 2, 3, 4$, the highest filtration efficiency is obtained for $\theta = \arctan b/w$. It is also observed that the filtration efficiency for different aspect ratios are very close when orientation angle is $3\pi/8$ due to similar values of l_c for this orientation angle, as observed in Fig.3.22. More generally, the similarity between Figs 3.22 and 3.28 implies that filtration efficiency is mainly governed by the cross section l_c .

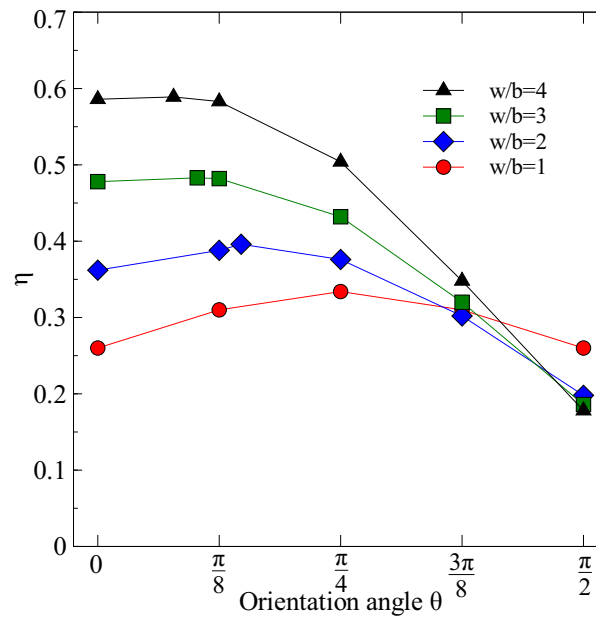


Figure 3.28: Filtration efficiency as a function of orientation angle for $Re = 8$.

Fig.3.29 shows, for $Re = 8$, filtration efficiency η versus windward area l_c for all aspect ratio w/b investigated in this paper and for different values of orientation angle. Fig.3.29 illustrates that the larger cross-section area is, the higher filtration efficiency can be obtained. The filtration efficiency almost linearly increased with the cross-section area, which results from the strong inertial force.

Fig.3.30 presents the same results for different Reynolds number. Same behavior can be observed, with a small dependency on Re , also indicating clearly that filtration efficiency is mainly governed by the windward area l_c in this flow regime.

3.3.2.4 Quality factor of filter with rectangular fiber

The quality factor of rectangular fiber are calculated. Fig.3.31 depicts the relationship between quality factor and Reynolds number with different aspect ratios. It can be observed

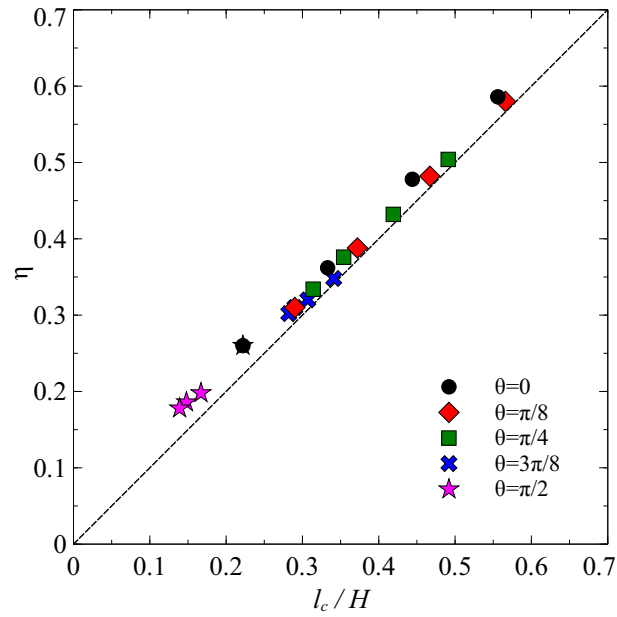


Figure 3.29: Filtration efficiency as a function of cross-section area of rectangular fiber for $Re=8$ and different orientation angles, $w/b = 1, 2, 3, 4$.

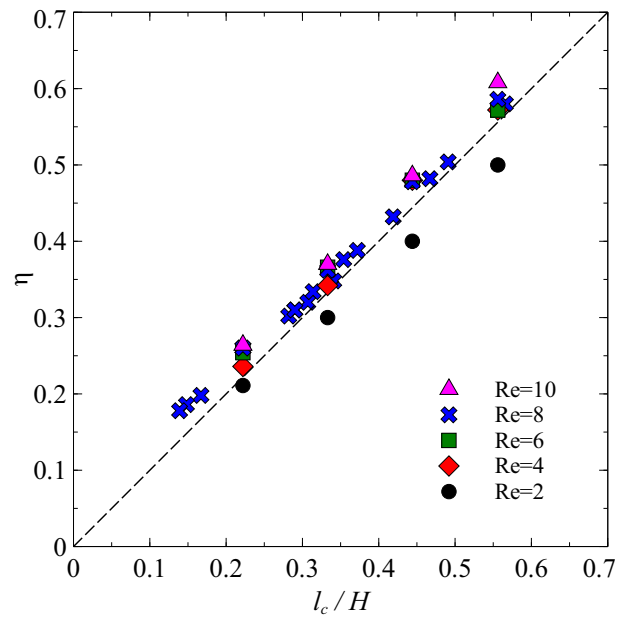


Figure 3.30: Filtration efficiency as a function of cross-section area of rectangular fiber for different Re and different orientation angles, $w/b = 1, 2, 3, 4$.

that the quality factor decreases rapidly when Re varies from 2 to 4. Then it gradually changes as Re varies from 4 to 10. Indeed, the pressure drop increases faster than η , which leads to a decline in the quality factor. As a reference, simulation results for filter made of circular fiber with diameter $D_f = D_h$ are also presented in Fig.3.31. The performance of filter for $w/b = 1$ and $w/b = 2$ is approximately equal in the region of $2 \leq Re \leq 10$. They have better quality than filters made of fiber with the aspect ratio of $w/b = 3$ and circular fiber. They also show great advantages by comparing with the case of $w/b = 4$.

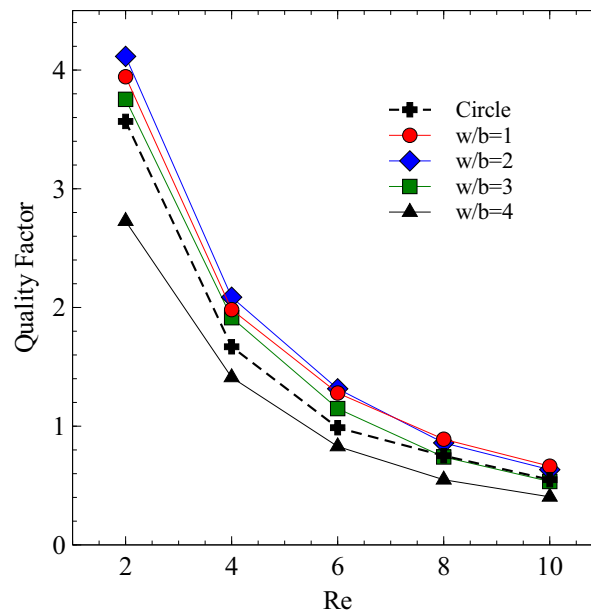


Figure 3.31: Quality factor of filter as a function of Re for $\theta = 0$.

Finally, for fixed $Re = 8$, we investigate which orientation angle and aspect ratio are favourable for a better performance of filter. Fig.3.32 shows the effect of orientation angle on the quality factor for $Re = 8$. As Fig.3.32 illustrates, quality factor for rectangular fiber increases with the orientation angle at first and then decreases. The quality factor is dependent on the ratio of η to F^* . Due to this value, we find that a higher quality factor can be obtained when $\theta = \pi/4$ for aspect ratio $w/b = 1$. According to these analysis, the rectangular fiber with aspect ratio $w/b = 1$ and $\theta = \pi/4$ (or diamond fiber) exhibits a better performance than the rectangular fiber and circular fiber, which agrees well with the result in section 3.2.3.3.

Moreover for $\theta = 3\pi/8$, values of quality factors are quite similar for the different aspect ratio investigated due to the fact that dimensionless drag force and filtration efficiency are not very dependent on w/b for this value of θ . The previous analysis of dependency of drag

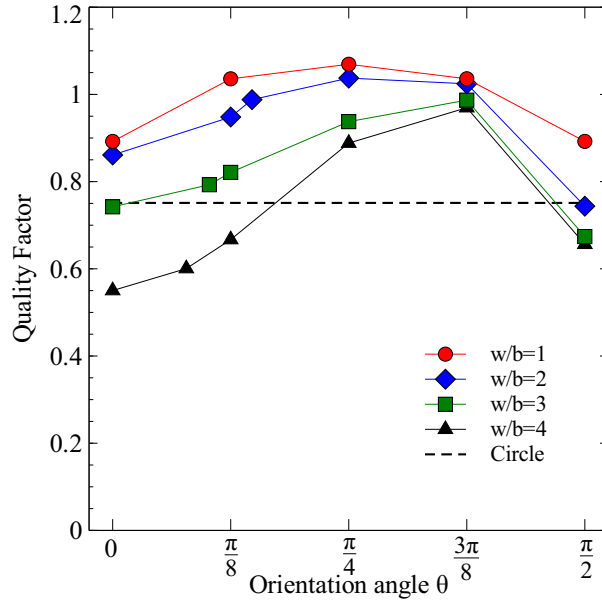


Figure 3.32: Quality factor as a function of orientation angle.

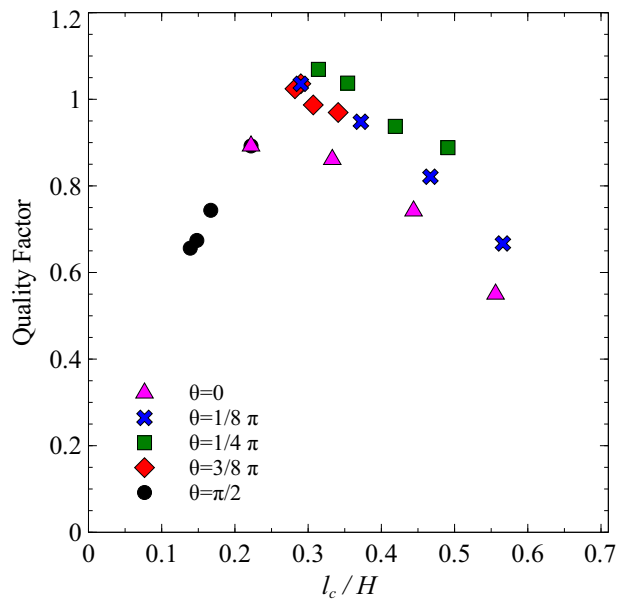


Figure 3.33: Quality factor as a function of l_c for $Re = 8$.

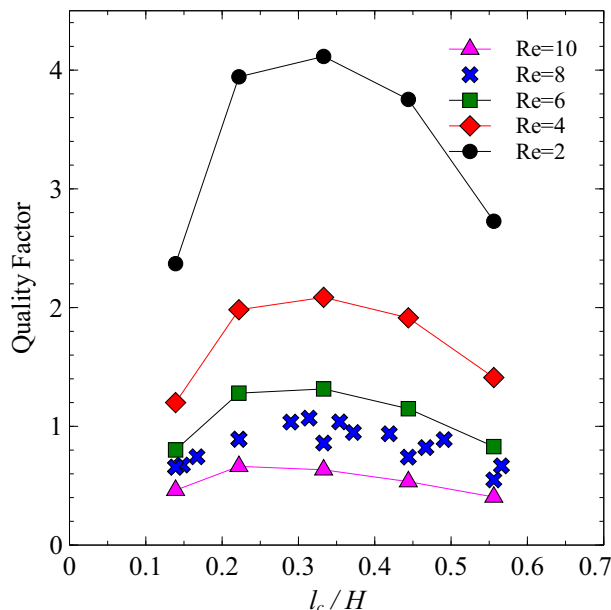


Figure 3.34: Quality factor as a function of l_c for different Re . For $Re = 8$, the orientation angles $\theta = 0, \pi/8, \pi/4, 3\pi/8, \pi/2$, for $Re = 2, 4, 6, 10$, $\theta = 0$.

force of filtration efficiency on cross section l_c show clearly that both of them increase with l_c . In term of quality factor, it exists an optimal value of l_c/H (around 0.3), as illustrated in Fig. 3.33, that maximize quality factor QF . In Fig. 3.34, we have plotted the QF as a function of l_c/H . QF is strongly influenced by the variation of l_c . It is good for low Reynolds number. Although increasing Reynolds number induces performance drop, a more uniform performance with l_c can be obtained.

3.4 Conclusion

In this chapter, we studied the effect of the particle size on the capture efficiency obtained with one-way coupling and two-way coupling respectively. For these small particles ($d_p \leq 8 \mu\text{m}$), one-way coupling in our model is sufficiently accurate to estimate the particle transport and deposition. The capture efficiency from our simulation agrees well with the results of Araujo et al. [148]. However, with respect to the larger particles, two-way coupling is much more practical owing to consideration of the influence of particle motion on the flow.

Single fiber capture efficiency is also investigated with two-way coupling for isolated particle and several particles cases. The influence of fiber shape on the single fiber capture

efficiency is analyzed for different Stokes number. The particle deposition on the fiber surface is essentially characterized by the particle Stokes number and intercept coefficient. It is found that the rate of increase of capture efficiency for single fiber is rapid at small Stokes number and then gradually becomes smaller at large Stokes number. For several particles case, a good agreement with empirical correlation of Schweers et al. [44] is observed. The impaction of particles on the front side of square-shaped fiber is more favorable than those on circular and diamond cases. With the same fiber shape, capture efficiency for isolated particle case is higher than the one for several particles case. The quality factor has been used to characterize the filtration performance in order to obtain a high filtration efficiency and low pressure drop. It is found that a filter with diamond fiber exhibits a better performance in terms of the quality factor for both isolated particle and several particles cases.

Based on these simulations, the diamond fiber has a good performance. It is one of types of rectangular shape and can be viewed as the rotation of the rectangular fiber. Thus, The effect of aspect ratio and orientation angle on filtration performance parameters, pressure drop and filtration efficiency of filter, have been investigated for rectangular fiber. The following conclusions can be drawn based on the simulation results obtained in this work.

Firstly, the dimensionless drag force is dependent on not only the orientation angle but also on Reynolds number when $2 \leq Re \leq 10$. For $\theta = 0$ and large value of aspect ratio (i.e., $w/b = 4$), the dimensionless drag force increases rapidly with Re . Due to the decrease of windward area of rectangular fiber, the dimensionless drag force decreased greatly with the orientation angle at this aspect ratio. Indeed, it has been illustrate that drag force increase greatly with l_c .

Secondly, the filtration efficiency is dependent on both orientation angle and aspect ratio during the filtration process. A larger aspect ratio (i.e., $w/b = 2, 3, 4$) at $\theta = 0, \pi/8$ generally lead to a higher filtration efficiency. For square fiber ($w/b = 1$) at $\theta = \pi/4$, filtration efficiency is higher than that of other orientation angles due to its larger cross-section area. Indeed, we found that for $Re > 1$, the filtration efficiency increases almost linearly with windward area. However, it can be noted that filtration efficiency increases slightly with Re .

Finally, in terms of quality factor, it is valuable to measure the filtration performance concerning the filtration efficiency and pressure drop of filter. For these different aspect ratios, the quality factor increases with orientation angle and reaches its maximum at a certain value, then decreases. For example, the largest quality factor is obtained for square

fiber at $\theta = \pi/4$. Filter performance, through quality factor, has also been analysed in term of windward area. This study shows that it exists an optimal value l_c that guarantee the minimization of pressure drop and maximization of filtration efficiency.

Generally, through the analysis of pressure drop, filtration efficiency and quality factor, the current study provide a theoretical indication for filter design and optimization with single fiber. Since the filtration performance such as quality factor corresponds to filter made of several identical fibers separated by a distance, in the next chapter, we will focus on the investigation of the filtration performance of filter with staggered fiber.

Chapter 4

Numerical simulation of filtration process for filter with staggered fibers

4.1 Introduction

The particle capture process in filter depends on particle and fiber diameters, particle and fluid densities as well as fiber arrangement. Since fiber arrangement, such as parallel and staggered configurations, influences significantly the filtration performance including filtration efficiency and pressure drop of filter [112], thus more studies on modeling the particle process in filter with different fiber arrangement are needed. Wang et al. [112] consider a series of circular fibers with parallel and staggered models to investigate the pressure drop and filtration efficiency. They found that the staggered model is better than the parallel model in terms of quality factor at the same conditions, because the staggered model exhibits higher filtration efficiency while nearly same pressure drop. Rabiee et al. [152] study the particulate flows through filter with three different circular fiber arrangements (parallel, staggered and random). By comparing the filtration efficiency, it is found that the staggered configuration is more efficient to capture particles. Ansari et al. [90] realized numerical study of solid particles motion and deposition in a filter with parallel and staggered arrangement of square fibers. They obtained that the first column fiber has a more importance in the particle deposition for both arrangements. Most particle deposition occurs on the first fiber for large St and other fibers have a negligible effect. Other researchers also investigated the effect of fiber arrangement on filtration efficiency including Tehrani et al. [2], Schweers et al.[44], Hosseini and Tafreshi [51], Li et al. [155]. Since the staggered arrangement is much more effective compared with parallel model, the

filtration performance of filter with staggered configurations should be focused and studied.

In chapter 3, the filtration performance of filter with a row of fibers in a laminar flow to their axes is investigated. Thus, in this chapter, we use the coupled LBM-DEM to simulate the filtration process of filter with staggered arrays of circular, diamond and square fibers. The effects of Reynolds number Re , intercept coefficient R and ratio of particle density to fluid density ε on pressure drop and filtration efficiency are investigated. Then the simulation results are used to explore the fiber's cross-sectional shape effect on filtration factors.

4.2 Circular fiber arrangements

Different fiber configuration can lead to the variation of the single fiber capture efficiency. Here we present three types of fiber arrangements, one beside the other, one underneath the other and staggered as shown in Fig.4.1.

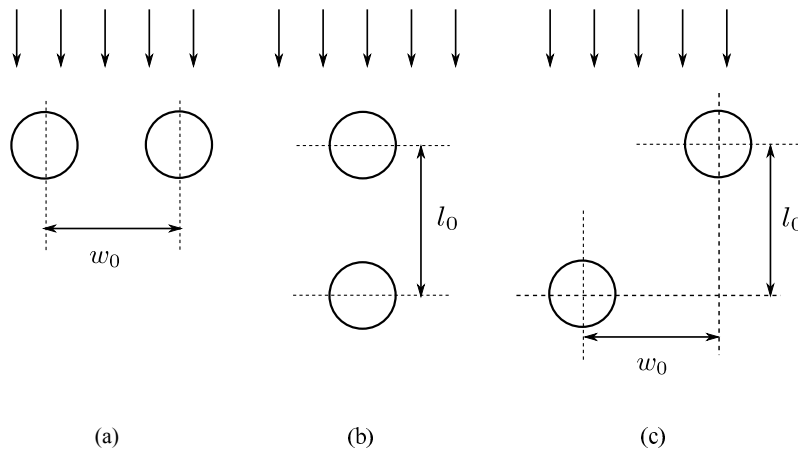


Figure 4.1: Fiber arrangements (a) one beside the other, (b) one underneath the other, (c) staggered.

Our fiber arrangement in part 3.3.1 of chapter 3 can be viewed as one beside the other due to the using of periodic boundary conditions (Fig.4.1a). To investigate the effect of fiber arrangement on single fiber capture efficiency, we compare our simulation results with the experimental work of Schweers et al. [44], although the fiber size used in chapter 3 is not the same with the literature, where the fiber size in literature is equal to $40 \mu\text{m}$. For several fibers existing in filter, the single fiber capture efficiency is obtained by calculating the mean particle fluxes in section upstream and downstream of fiber and the fiber projection area.

Single fiber capture efficiency as a function of St for different fiber arrangements is presented in Fig.4.2. Our simulation results obtained in chapter 3 for 500 particles injected are plotted in Fig.4.2 for the configuration one beside the other. For two fibers one beside the other, single fiber capture efficiency increases with the Stokes number for results obtained by both LBM-DEM and experiment. The differences between simulation and experiment is due to the different fiber sizes used in the two cases. Another reason is that the rebound effect of particle is not considered in the simulation. For fibers one underneath the other, the shading effects reduces the number of captured particles. With decreasing distance between fibers w_0 , the first fiber plays an important role concerning capture efficiency and no particles contact with the second fiber. For the case of staggered fibers, since the displacement of left fiber in Fig.4.1c exerts a substantial effect, the single fiber capture efficiency is higher in contrast to other two cases. From Fig.4.2, it is found that the single capture efficiency for fibers one underneath the other is generally lower than the staggered fibers and fibers one behind the other.

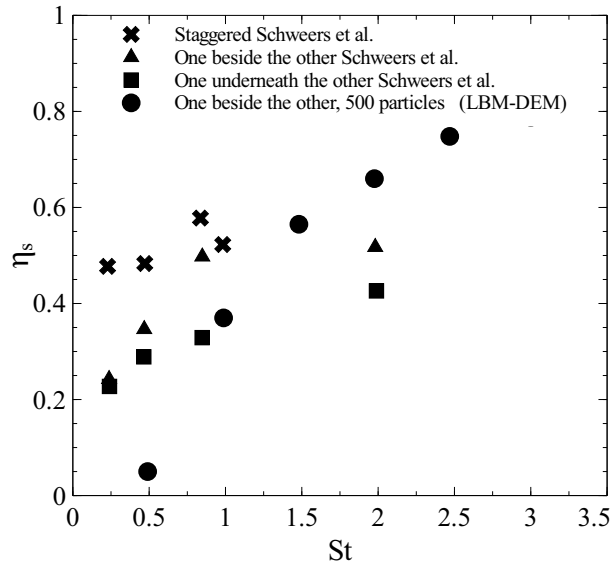


Figure 4.2: Single fiber capture efficiency as a function of Stokes number with different fiber arrangements.

As staggered configurations are more efficient to capture particles, in the following, we focus on the study of these configurations. To valid our code, we first performed the simulations of the flow through the staggered circular fibers as depicted in Fig.4.3, where we only consider a strip of domain between two lines. Then the simulation results are compared

with previous work published in the literature. A series of staggered arranged circular fibers of diameter D_f are placed in a rectangular domain with length L and width H . w_0 and l_0 are the horizontal and vertical separation distance between two neighboring fibers, where $H = 2w_0$. A constant velocity $\vec{U}_0 = \begin{pmatrix} 0 \\ u_{0y} \end{pmatrix}$ is applied at the inlet. $\partial u_{0x}(x, 0)/\partial y = 0$ and $\partial u_{0y}(x, 0)/\partial y = 0$ are imposed at the outlet. We use the periodic boundary at both left side and right sides.

The numerical results for the staggered configuration (Fig.4.3) are compared with those of Liu and Wang [58] and Wang et al. [112], and also compared with the dimensionless drag force expression for the staggered model proposed by Kuwabara [37]. The analytical expression of dimensionless drag force resulted from Kuwabara flow is expressed as:

$$F^* = \frac{4\pi}{-0.5 \ln \beta - 0.75 - 0.25\beta^2 + \beta} \quad (4.1)$$

where $\beta = \frac{\pi D_f^2}{8l_0 w_0}$ is the fiber volume fraction. According to this expression, the value of drag force applied on fibers is only dependent of fiber volume fraction.

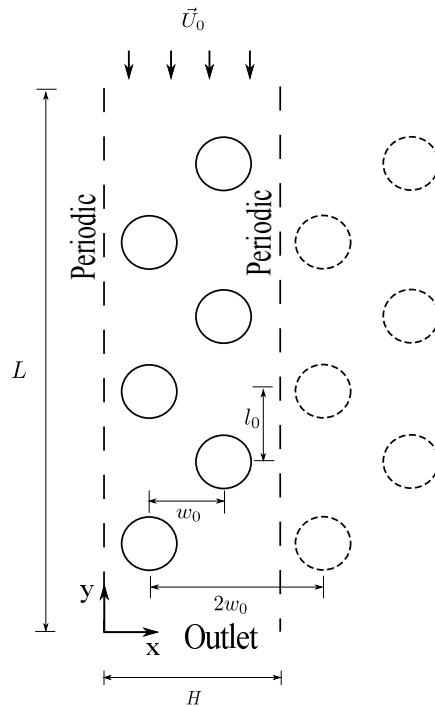


Figure 4.3: A schematic diagram of the staggered structure of circular fibers

The Fig.4.4(a) demonstrates the relationship between the dimensionless drag force and

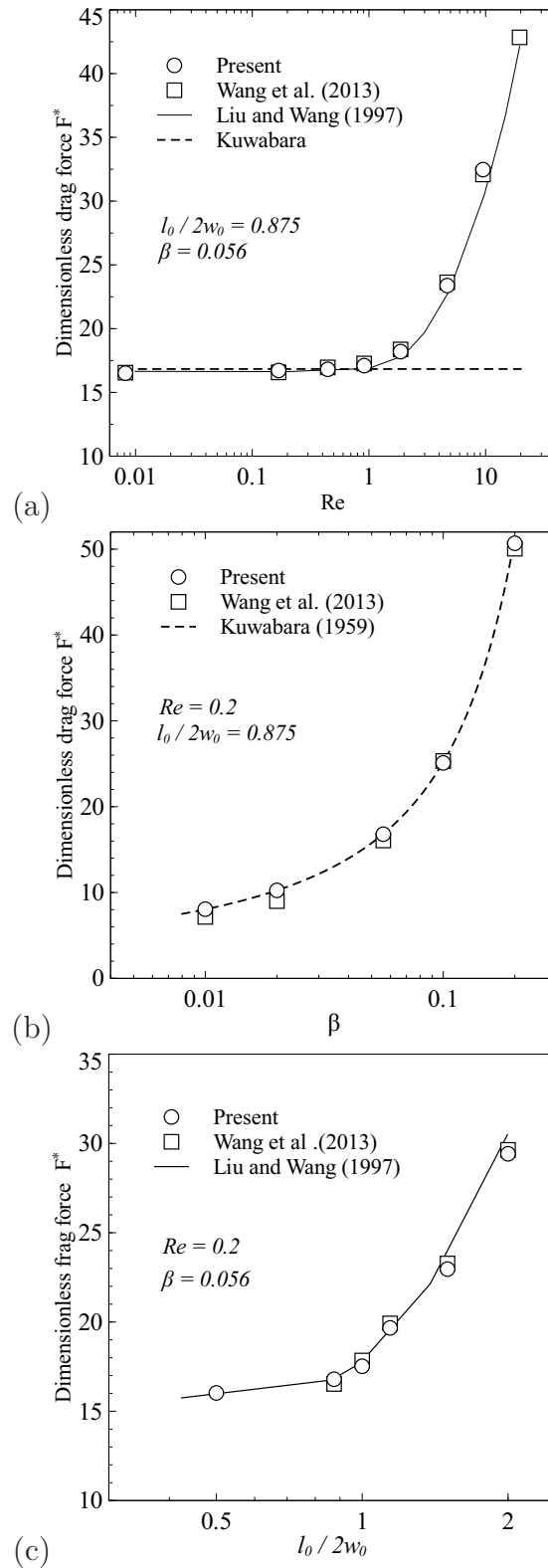


Figure 4.4: Dimensionless drag force as a function of (a) Reynolds number Re , (b) volume fraction β and (c) separation ratio $l_0/2w_0$ for circular fibers.

Re in the case of $\beta = 0.056$ and $l_0/2w_0 = 0.875$. Here we use the $l_0/2w_0 = 0.875$ in order to be consistent with the literature. It is found that the drag force obtained in the literature [58, 112] is nearly constant for $Re < 1$. However, the value of drag force increased with Reynolds number for $1 < Re < 20$. Our simulation results obtained by LBM are in good agreement with the literature [58, 112] in Fig.4.4(a). Compared with Kuwabara model, it should be noted that $Re = 1$ is the turning point for the pressure, which indicates that expression (4.1) is not valid for $Re > 1$.

Dimensionless drag force as a function of fiber volume fraction is also studied. The Reynolds number and separation ratio are fixed, F^* is calculated for several values of volume fraction. The value of dimensionless drag force corresponding to $Re = 0.2$ and $l_0/2w_0 = 0.875$ are obtained with different β , as shown in Fig.4.4(b). It is obvious that the value of dimensionless force increases rapidly as β increases. Our numerical results are in very good agreement with Kuwabara's expression and with the prediction of Wang et al. [112] at $Re = 0.2$ and $l_0/2w_0 = 0.875$.

The effect of aspect ratio of the array on the dimensionless drag force is determined at $Re = 0.2$ and $\beta = 0.056$, the results are shown in Fig. 4.4(c). This validation also approves the results of Liu and Wang [58] and Wang et al. [112].

4.3 Numerical study of particles motion and deposition on staggered arrayed fibers with various shapes

In this section, we consider the effect of the vertical neighboring fiber on the filtration performance. The filter for fibers arranged with staggered configurations is presented in Fig.4.5. Since the fiber arrangement is not regular, the particles are injected along the whole inlet, here we still focus on the filtration efficiency, pressure drop and quality factor of filter.

4.3.1 Model description and filtration parameters

A schematic view of a periodic cell of the filter is illustrated in Fig.4.5. Our simulations are conducted for two rows of fibers staggered in a rectangular domain, of width $H = 0.001$ m and length $L = 0.0017$ m, bounded by velocity inlet and periodic sides. Fibers with three cross-sectional shapes which are circular, diamond and square are considered respectively.

The horizontal and vertical separation distance between two neighboring fibers are w_0 and l_0 respectively, where $H = 2w_0$. The projected area of each fiber perpendicular to the flow direction is $D_f/H = 1/2.5$. For diamond fiber, it is a square rotated by $\pi/4$ with a diagonal D_f . A constant velocity $\vec{U}_0 = \begin{pmatrix} 0 \\ u_{0y} \end{pmatrix}$ is applied at the inlet. At the outlet, we have imposed $\partial u_{0x}(x, 0)/\partial y = 0$ and $\partial u_{0y}(x, 0)/\partial y = 0$. Both left side and right side boundaries are periodic for fluid and solid particles. The fluid density and kinematic viscosity are 1.2 kg/m^3 and $4.4 \times 10^{-5} \text{ m}^2/\text{s}$ respectively. As for the case of previous simulations, once the flow field reaches a steady state, particles are randomly injected on a line at the inlet of the channel (see Fig.4.5a). The initial velocity of injected particles is the same as the fluid velocity.

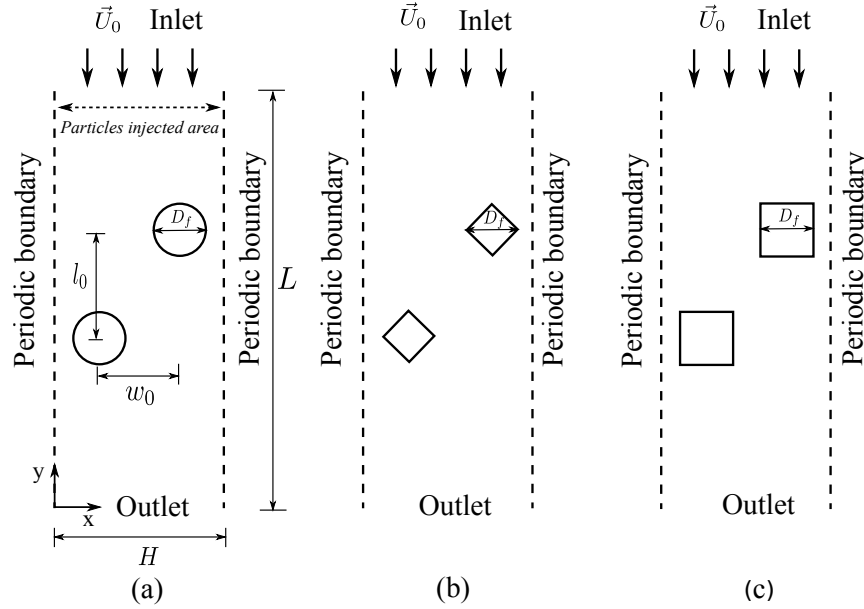


Figure 4.5: Schematic view of structure of staggered model of filters with (a) circular fibers (b) diamond fibers (c) square fibers.

Following previous study presented in part 3.3.2.2, pressure drop Δp is related to drag force F_D per unit length of a single fiber oriented transverse to the flow as [58]:

$$\Delta p = \frac{F_D L}{2A} \quad (4.2)$$

where the cross-section is here equal to $A = l_0 w_0$. Dimensionless drag force F^* is:

$$F^* = \frac{F_D}{\mu U_0} \quad (4.3)$$

where μ is fluid dynamic viscosity and U_0 is the inlet velocity.

The filtration process investigated in this chapter is an initial stage of the process, in a sense that the fiber shape does not change with time and the filter is regarded as a clean one, because the deposition of particles inside the filter is relatively small in the initial stage and its effect on the filter is negligible [156]. Thus, it is reasonable to assume that particles are removed from the flow if they deposit on the surface of fibers or escape from the channel outlet [113]. We recall that the definition of the filtration efficiency of filter is given by Eq (3.17) of chapter 3.

In the following parts, we use the staggered configurations in Fig.4.5 to investigate the effect of Reynolds number Re , intercept coefficient $R = \frac{d_p}{D_f}$ and density ratio $\varepsilon = \frac{\rho_p}{\rho}$ on pressure drop and filtration efficiency of filter with circular, diamond and square cross-sectional shapes. For R , various particle diameters are used in the simulations (20 μm , 30 μm , 40 μm , 50 μm , 60 μm). For ε , the particle densities are 720 kg/m^3 , 1200 kg/m^3 , 1680 kg/m^3 , 2160 kg/m^3 , and 2430 kg/m^3 . The volume fraction of circular, diamond and square are respectively $\beta_c = \frac{\pi D_f^2}{8l_0w_0} = 0.157$, $\beta_d = \frac{D_f^2}{4l_0w_0} = 0.1$ and $\beta_s = \frac{D_f^2}{2l_0w_0} = 0.2$. The projected area of fiber $D_f = 0.0004$ m, fiber volume fraction and separation ratio $l_0/w_0 = 1.6$ are kept fixed for all the simulations.

4.3.2 Pressure drop of clean filter with staggered fibers

When $Re \leq 1$, Huang et al. [109] found that the dimensionless drag force is independent on the Reynolds number for both circular and noncircular fiber. In order to complete the study, in this section we investigate the relationship between dimensionless drag force and Reynolds number for circular, diamond and square fiber for $Re > 1$ with Fig.4.5. We vary the Reynolds number by changing the fluid velocity in the following simulations.

Fig.4.6 presents the flow field around the fiber with different shapes for $Re = 5$. We focus on the streamlines near to the fiber, part of the streamlines in the computational domain are showed. It is noticed that the streamlines close to circular, diamond and square fiber are different. Obviously, the cross-sectional shape of fiber modifies the structure of fluid field which leads to the variation of the pressure drop across the filter. Fig.4.7 shows the dimensionless drag force versus the Reynolds number for circular, diamond and square fiber. As illustrated in Fig.4.7, F^* is influenced by Re and linearly increased with it in the region of $2 \leq Re \leq 10$. The dimensionless drag force for the diamond fiber is smaller than the cases of circular and square fiber. It indicates that filter with diamond fiber has a lower pressure drop. This can be ascribed to a better streamlined shape of diamond fiber.

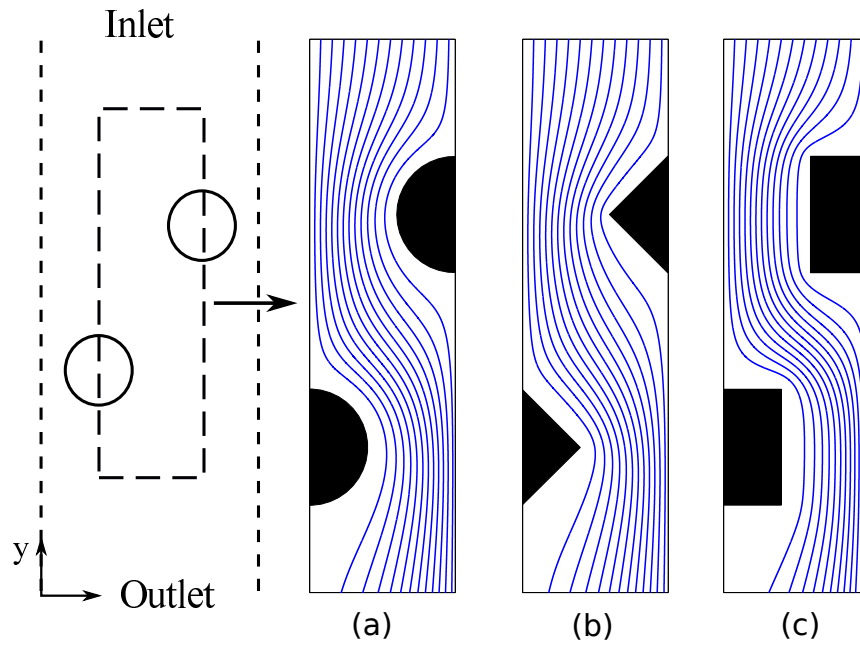


Figure 4.6: Streamlines around fibers with (a) circular (b) diamond and (c) square cross-sectional shape for $Re = 5$, $l_0 = 0.0008$ m, $w_0 = 0.0005$ m, $D_f = 0.0004$ m.

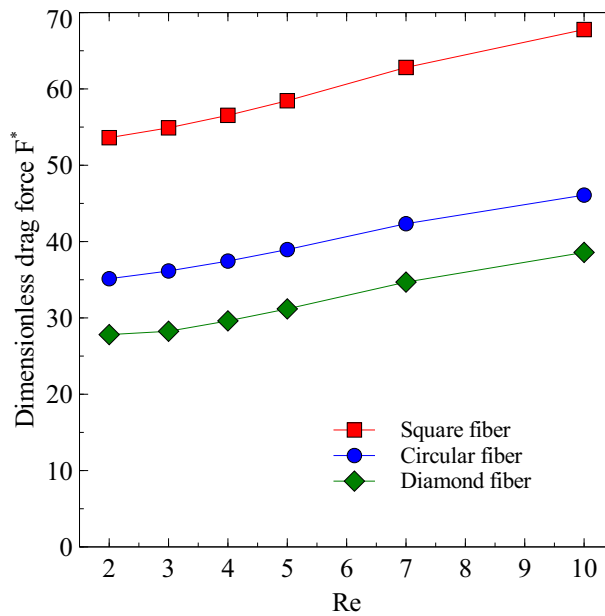


Figure 4.7: Dimensionless drag force versus Re applied on the circular, diamond and square fibers.

A better streamlined shape can reduce the fiber's drag force [153].

4.3.3 Filtration efficiency of filter with staggered fibers

The filtration efficiency of filter with circular, diamond and square fiber is calculated by Eq.(3.17). In present simulations, 500 particles are randomly injected at the inlet (see Fig.4.5a) once the flow field reaches the steady state. The velocities and trajectories of solid particles depend on the fluid velocity field, whose the regime is characterized by the Reynolds number. Therefore, the relationship between filtration efficiency and Reynolds number is investigated and the numerical results are plotted for small particle size ($R = 0.05$) in Fig.4.8 and for large particle size ($R = 0.15$) in Fig.4.9. Fig.4.8 demonstrates that the filtration efficiency η increases with an increase in Re for small R (i.e. $R = 0.05$). Then η reaches a certain value and does not change with Re anymore for $Re < 10$. As seen in Fig.4.9 for large particle size, the filtration efficiency of filter with three cross-sectional fibers reaches their maximum value at $Re = 2$ and then slightly varied with Re for large intercept coefficient ($R = 0.15$). By comparison of Figs.4.8 and 4.9, Reynolds number has an obvious effect on filtration efficiency for small R . When the Reynolds number increases, particle performs strong inertia and deviate from the streamlines. As particles approach the fiber, they do not change their trajectories and finally deposit on the surface of the fiber. The effect of Reynolds number can be negligible as the inertia of particle increases to the value that most particles at the upstream of the system deviate from streamlines and move straightforward. The filtration efficiency of filter with square fiber has a higher value than that of circular and diamond fiber for both small and large R .

In order to understand the particle behavior in fluids more clearly, Fig.4.10 presents instantaneous velocity field of fluid and particle distribution for filter with circular, diamond and square fiber for $Re = 5$. Particle process including particles injected, particle transport and deposition on the fiber is shown at different time steps. We can recognize that particles move toward the front of fiber which is due to the inertia effect. As seen in Fig.4.10, particles transport affects the fluid velocity field compared with fluid streamlines presented in Fig.4.6.

As mentioned above, R is also an important parameter that determines the filtration efficiency. The effect of this parameter on the filtration efficiency is presented for low density ratio ($\varepsilon = 600$) in Fig.4.11 and for high density ratio $\varepsilon = 2025$ in Fig.4.12. For Fig.4.11, it is observed that the filtration efficiency for circular and diamond fiber is more sensitive to R than square case. As R is increased, the number of particles captured by

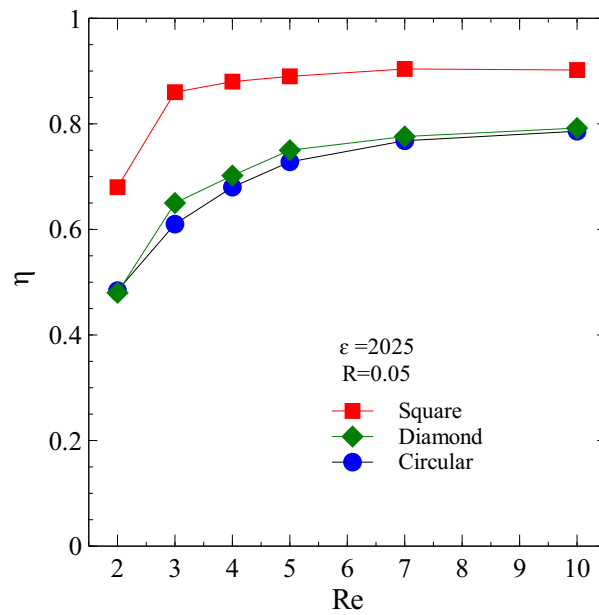


Figure 4.8: Filtration efficiency versus Reynolds number for $R = 0.05$ and density ratio $\varepsilon = 2025$.

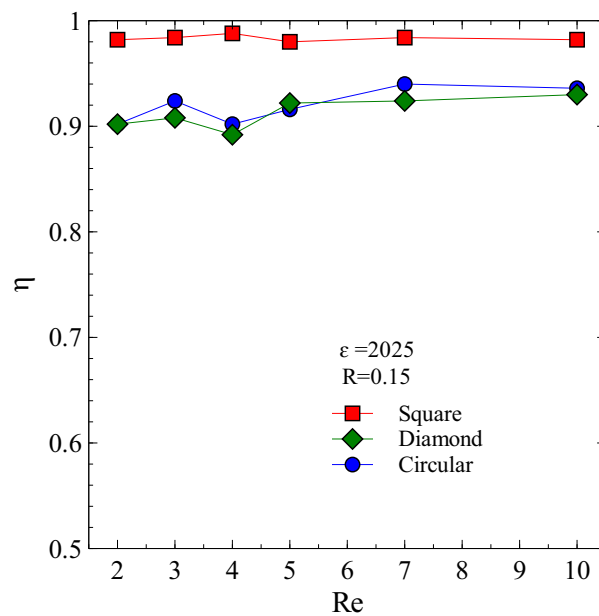


Figure 4.9: Filtration efficiency versus Reynolds number for $R = 0.15$ and density ratio $\varepsilon = 2025$.

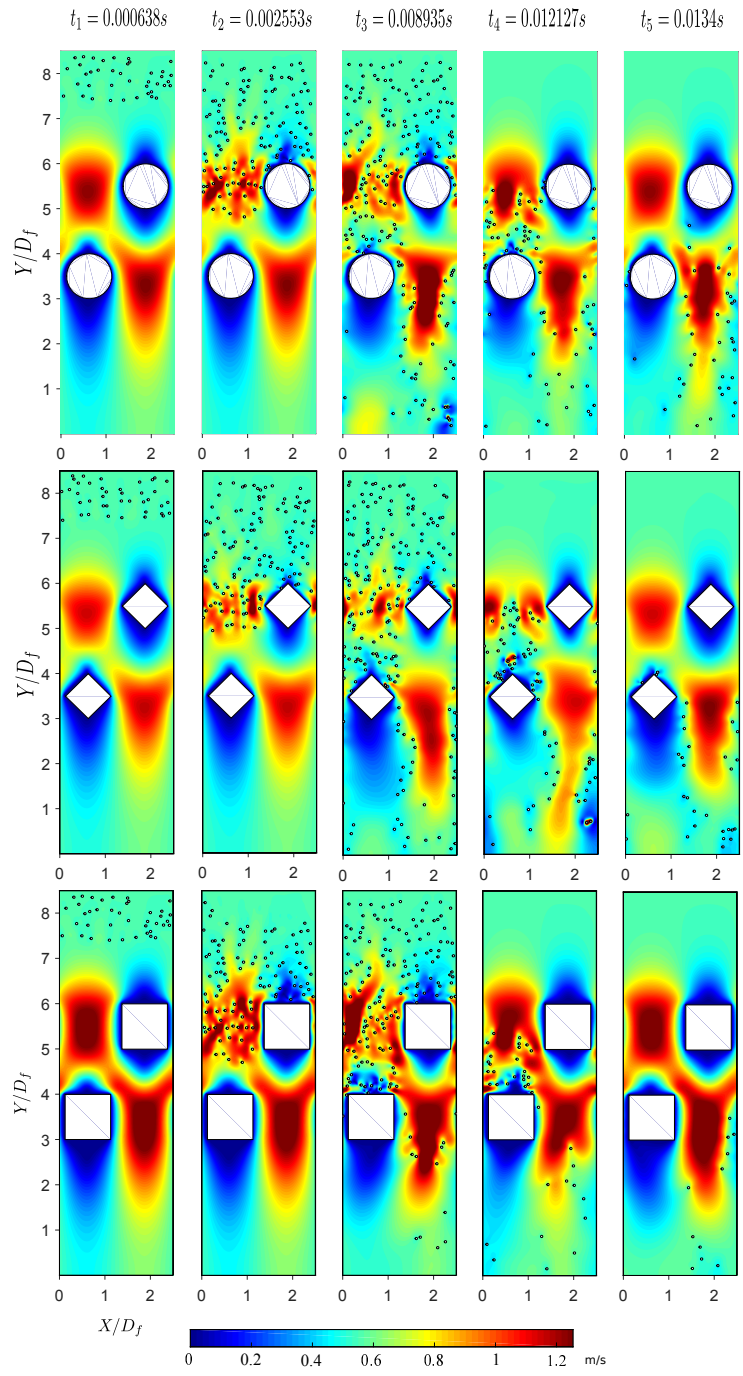


Figure 4.10: Instantaneous velocity field and particle distribution for filter with circular, diamond and square fibers for $Re = 5$, $R = 0.05$ and $\varepsilon = 2025$.

three types of fibers improves. For Fig.4.12, large particles with high density are easier to deposit on the surface of fiber than small particles. The gap of filtration efficiency for large and small particles is gradually reduced. This is because particles with high density have a higher inertia. From Fig.4.11 and Fig.4.12, we can see that square fiber is more favorable to capture the particles compared with the circular and diamond fiber, which accords with the previously results presented in chapter 3.

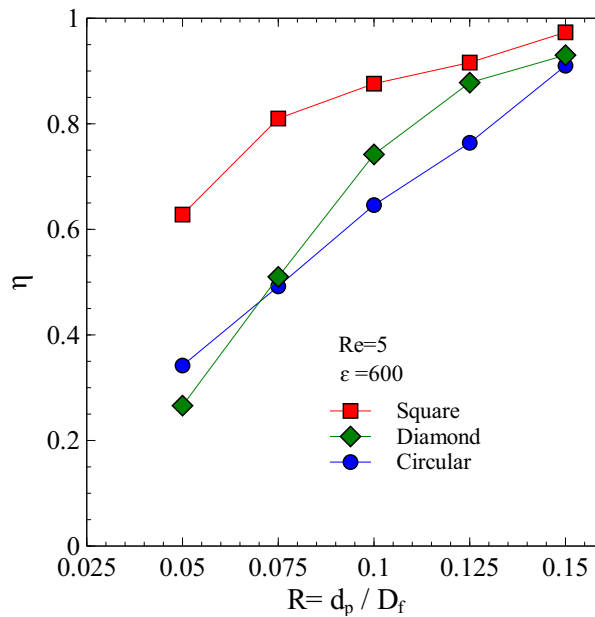


Figure 4.11: Filtration efficiency versus intercept coefficient R , density ratio $\varepsilon = 600$ and $Re = 5$.

The filtration efficiency of filter as a function of density ratio is depicted in Fig.4.13 for small $R = 0.05$ and in Fig.4.14 for large $R = 0.15$. In the simulations, a series of particle densities are used to change the density ratio ε . Fig.4.13 indicates that for small particles the number of deposited particles on the surface of fiber first increases rapidly with ε , then increases at a relatively lower slope for three cases. It is because the particle deposition is characterized by the Stokes number (St) and the fact that the inertia for small particles in the region of density ratio $600 \leq \varepsilon \leq 2200$ grows as the St increases from a low value to a large one. This effect is gradually reduced with the increases in St . Fig.4.14 for large particles illustrates that the filtration efficiency for circular, diamond and square fiber is independent on the density ratio. The inertia of large particle is intense enough and the fluid field has little effect on the particle deposition. As a consequence, the majority of particles are captured on the front surface of the fiber. The number of captured particle

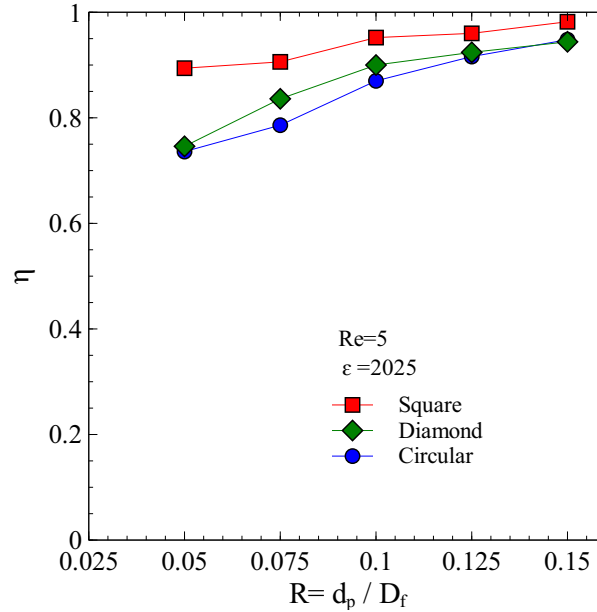


Figure 4.12: Filtration efficiency versus intercept coefficient R , density ratio $\varepsilon = 2025$ and $Re = 5$.

by the square fibers is still larger than the circular and diamond cases.

Since the Stokes number is related to the Reynolds number Re , intercept coefficient R , density ratio ε by $St = \frac{1}{18} Re \cdot \varepsilon \cdot R^2$. All these parameters influence the filtration efficiency. However, Stokes number can be considered as a whole parameter comprising Re , R^2 and ε . Fig.4.15 demonstrates the filtration efficiency of filter with circular fibers as a function of St . The filtration efficiency first increases rapidly with St for small value, then increases at a relatively slower rate. For $St > 10$, the filtration efficiency becomes essentially independent of St . Fig.4.16 presents the filtration efficiency as a function of St for diamond fibers. It is found that the effect of St on filtration efficiency is similar to the circular case. This is because the the filtration efficiency of filter with diamond fiber approaches to the one of circular case as shown from Fig.4.8 to Fig.4.14. Fig.4.17 shows the variation of filtration efficiency of filter with square fibers with Stokes number. The filtration efficiency for square fibers increases rapidly with St for $St < 5$. This trend is expected, because the inertial impaction increases with the increase in St . In order to compare the filtration efficiency for circular, diamond and square fiber, we plot the results together as seen in Fig.4.18. When the filtration efficiency is not dependent on St , η for square fiber can reach a constant value which is larger than the one for circular and diamond cases.

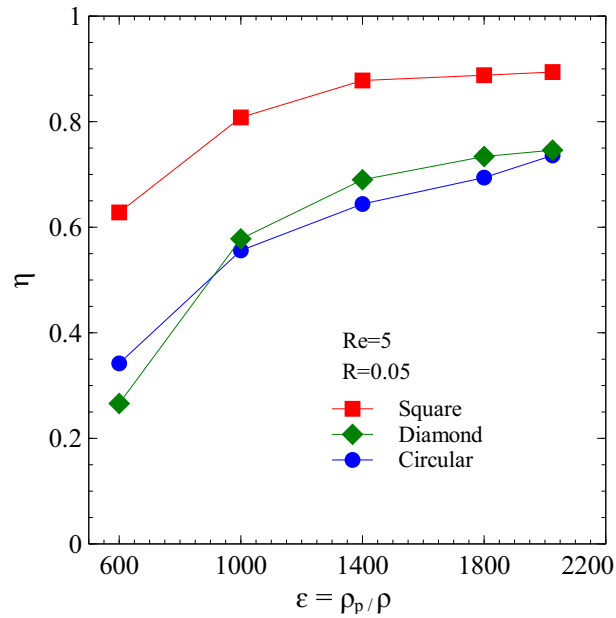


Figure 4.13: Filtration efficiency versus density ratio $\varepsilon = \rho_p/\rho$ for $R = 0.05$ and $Re = 5$.

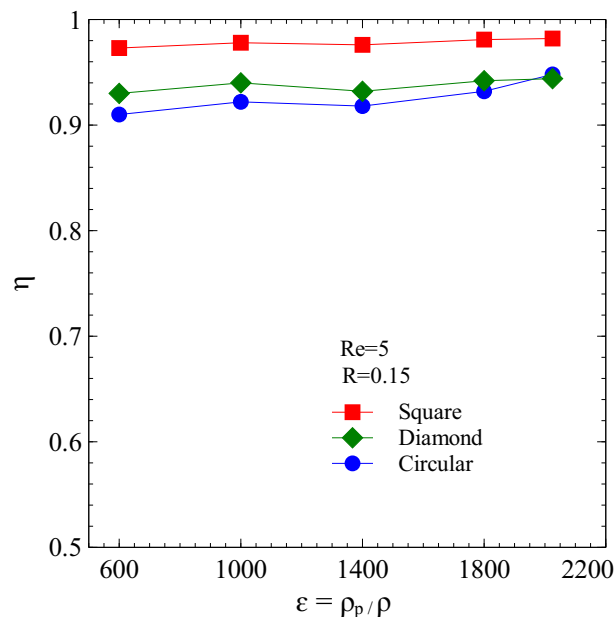


Figure 4.14: Filtration efficiency versus density ratio $\varepsilon = \rho_p/\rho$ for $R = 0.15$ and $Re = 5$.

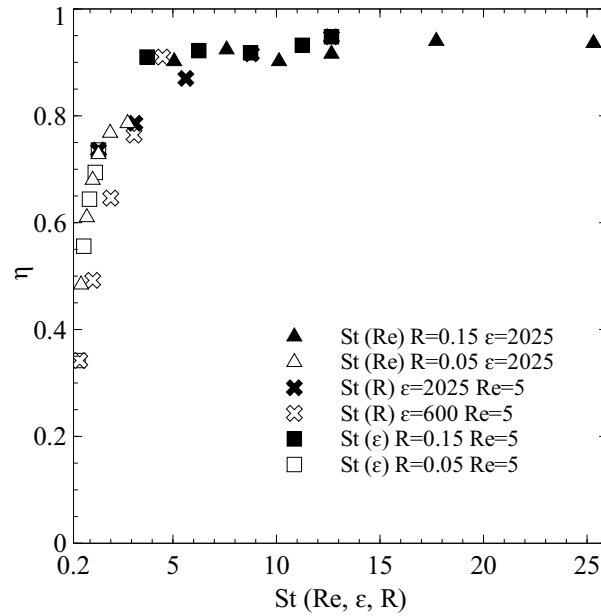


Figure 4.15: Filtration efficiency of filter with circular fiber as a function of St .

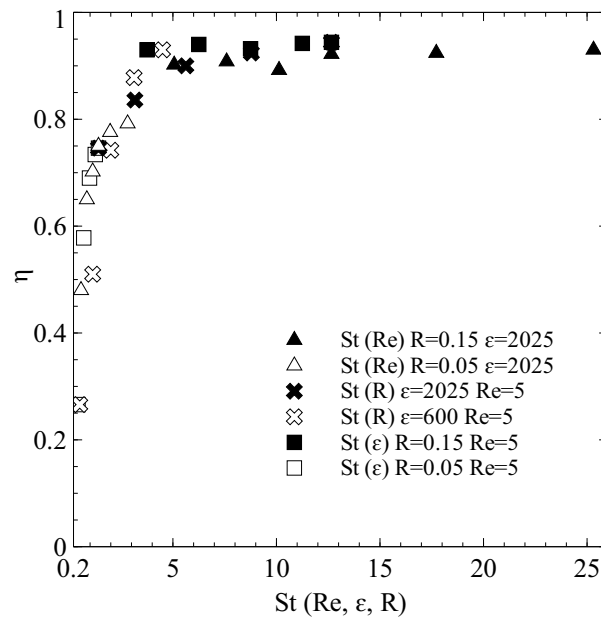


Figure 4.16: Filtration efficiency of filter with diamond fiber as a function of St .

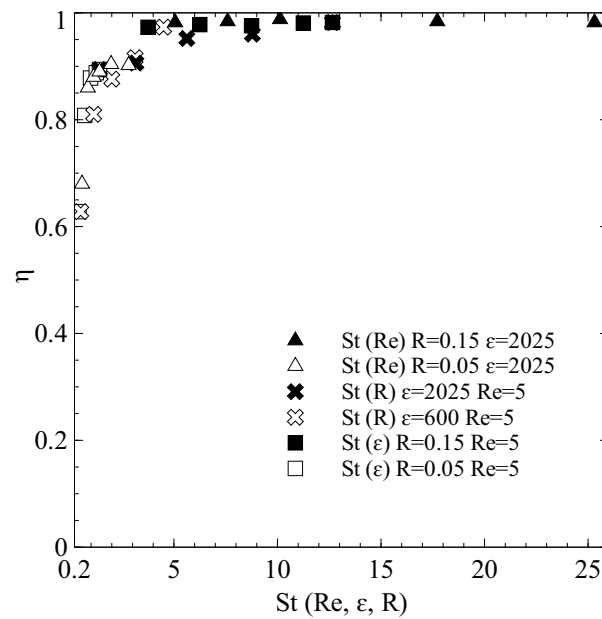


Figure 4.17: Filtration efficiency of filter with square fiber as a function of St .

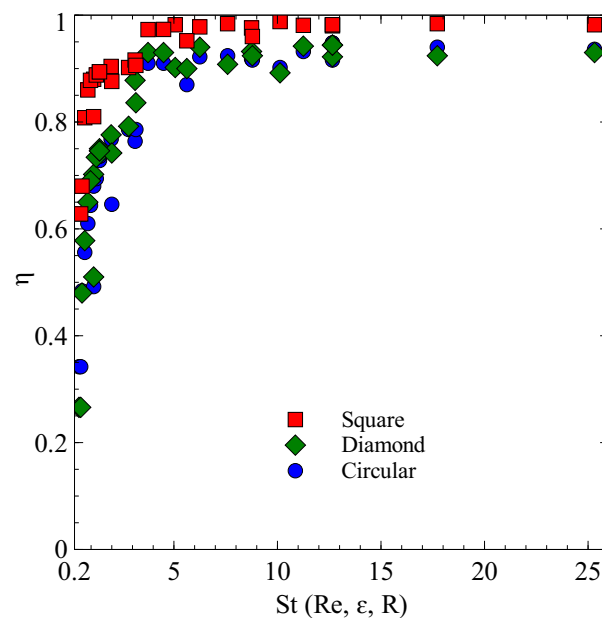


Figure 4.18: Filtration efficiency of filter with circular, diamond and square fiber as a function of St .

4.3.4 Capture contribution of each fiber to the filtration efficiency

The filtration efficiency of filter with different fibers were analysed in section 4.3.3. In order to know more about the information inside the filter, here we focus on the study of contribution of each fiber to the filtration efficiency. The concept of capture contribution η_i proposed by Wang et al. [112] is used in this section. It is defined as the ratio of captured particle number by i th fiber $N_{capture,i}$ to the total number $N_{capture,tot}$ of captured particles:

$$\eta_i = \frac{N_{capture,i}}{N_{capture,tot}} \quad (4.4)$$

It is noted that the $\sum_i \eta_i = 1$.

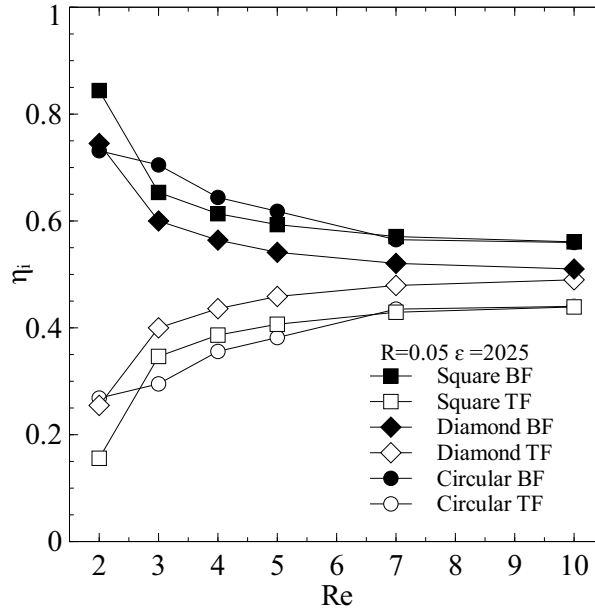


Figure 4.19: Capture contribution of fiber as a function of Re for $R = 0.05$ and $\varepsilon = 2025$.

The fiber located in bottom of computational region (close to outlet) is called bottom fiber (BF) and the other one is called top fiber (TF) in Fig.4.5. The influence of Re on capture contribution η_i of circular, diamond and square fibers is presented in Fig.4.19 and Fig.4.20 respectively. Fig.4.19 shows the capture contribution of fiber as a function of Re for small particles ($R = 0.05$) with high density $\varepsilon = 2025$. For bottom fiber, the capture contribution of circular, diamond and square fibers decreases with Re for $2 \leq Re \leq 5$ and then it keeps a constant value for $7 \leq Re \leq 10$. However, the capture contribution of top fiber increases with Re for $2 \leq Re \leq 5$ and then keeps constant as well for $7 \leq Re \leq 10$.

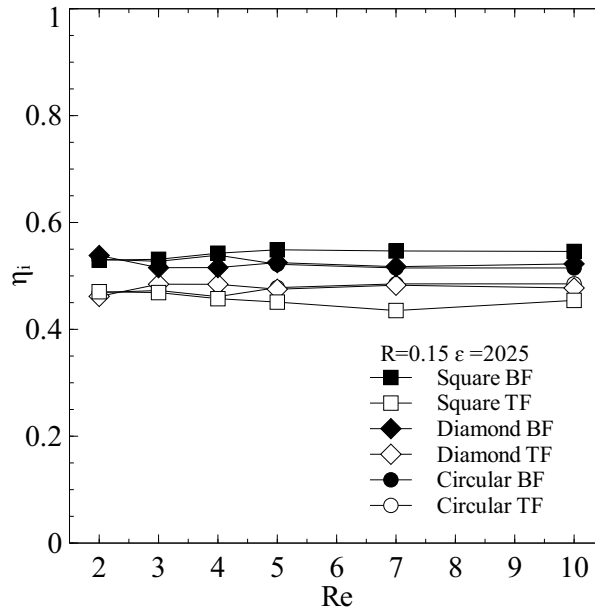


Figure 4.20: Capture contribution of fiber as a function of Re for $R = 0.15$ and $\varepsilon = 2025$.

It can be noted that the capture contribution of circular, diamond and square fibers are almost symmetric on $\eta_i = 0.5$. The top fiber generally makes low contribution to the filtration efficiency compared with bottom fiber. Since the top fiber are placed upstream of filter and the injected particles can change the fluid velocity field, the particles passing through the top fiber still have the possibility to be captured by the bottom fiber. Fig.4.20 presents the capture contribution of fiber as a function of Re for large particles ($R = 0.15$) with high density $\varepsilon = 2025$. The capture contribution of circular, diamond and square fibers varies slightly with Re when $2 \leq Re \leq 10$. There is not much differences for the number of particles captured by the bottom fiber and top fiber. The capture contribution of circular, diamond and square fibers approach closely to $\eta_i = 0.5$ for large particles ($R = 0.15$).

Fig.4.21 and Fig.4.22 present the effect of R on capture contribution of circular, diamond and square fibers. Capture contribution as a function of R for particles with low density is shown in Fig.4.21. For bottom fiber, it is found that the capture contribution of circular, diamond and square fibers decreases remarkably with R for $0.05 \leq R \leq 0.1$ and then reaches a constant value when $0.125 \leq R \leq 0.15$. For the top fiber, the capture contribution of circular, diamond and square fibers increases with R for $0.05 \leq R \leq 0.1$ and is close to $\eta_i = 0.5$. For diamond fiber, the capture contribution of bottom fiber and top fiber are nearly the same when $0.1 \leq R \leq 0.15$. Fig.4.22 demonstrates the capture

contribution of circular, diamond and square fibers as a function of R for particles with high density. As the R increases, less and less particles passing through top fiber are not captured by the bottom fiber. Thus the gap of η_i of circular, diamond and square fibers decreases with R when $0.05 \leq R \leq 0.1$ for bottom and top fibers.

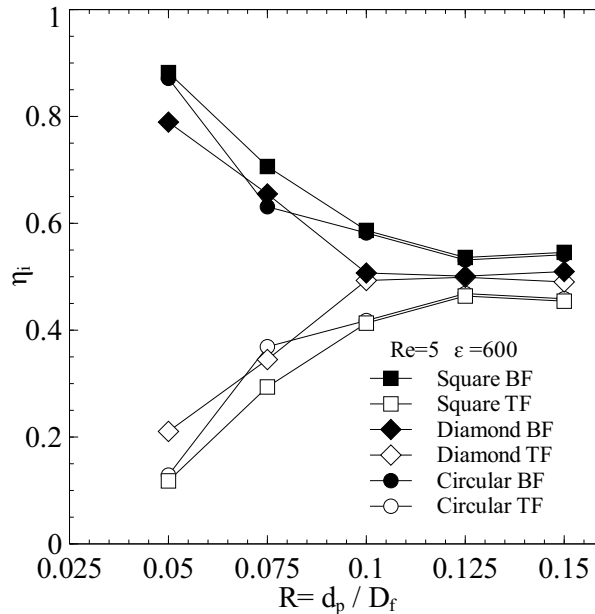


Figure 4.21: Capture contribution of fiber as a function of R for $Re = 5$ and $\varepsilon = 600$.

The influence of $\varepsilon = 2025$ on the capture contribution is presented in Fig.4.23 and Fig.4.24. Fig.4.23 demonstrates that capture contribution of circular, diamond and square fibers as a function of $\varepsilon = 2025$ for small particles $R = 0.05$. η_i decreases with ε for bottom fiber and increases with ε for top fiber. However, for large particles ($R=0.15$), capture contribution varies slightly with ε as shown in Fig.4.24. Capture contribution of diamond fiber is not very obvious for bottom and top fibers when $1000 \leq \varepsilon \leq 2025$.

We consider the effect of Re , R and ε together on the capture contribution, then capture contribution for circular, diamond and square fiber as a function of St is presented in Fig.4.25. The contribution of each bottom fiber decreases with St and then is kept constant for $St > 5$. This is contrary for top fiber, η_i increases with St and then arrive a constant value which is close to the one of bottom fiber for $St > 5$. It is noted that Stokes number has obvious effect on capture contribution of each fiber for $St < 5$. As Stokes number increases ($0 < St < 5$), the gap of contribution of each fiber is gradually reduced due to the effect of inertia.

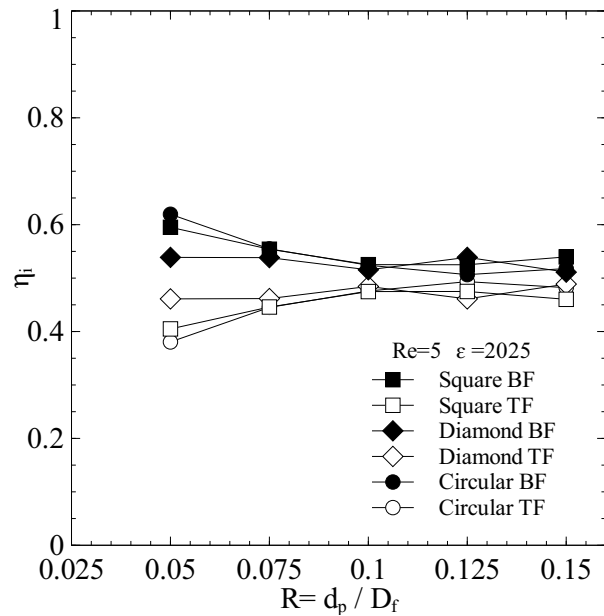


Figure 4.22: Capture contribution of fiber as a function of R for $Re = 5$ and $\varepsilon = 2025$.

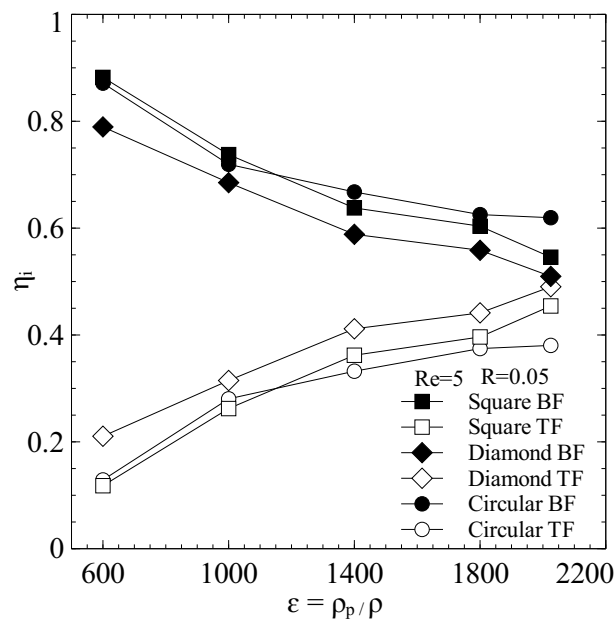


Figure 4.23: Capture contribution of fiber as a function of ε for $Re = 5$ and $R = 0.05$.

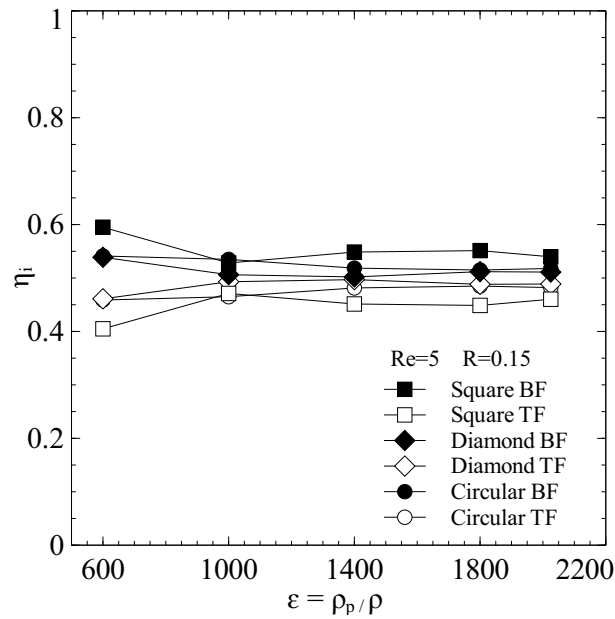


Figure 4.24: Capture contribution of fiber as a function of ε for $Re = 5$ and $R = 0.15$.

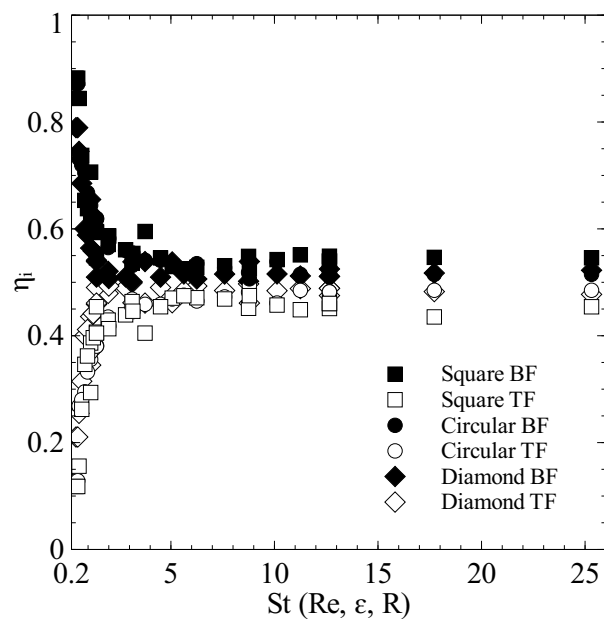


Figure 4.25: Capture contribution of circular, diamond and square fibers as a function of St .

4.3.5 Quality factor of filter with staggered fibers

We use the quality factor, which combines the effect of filtration efficiency and pressure drop together, to measure the filtration performance. The effect of particle properties on the quality factor is analyzed. Results of computation of the quality factor QF for three types of fibers and different kinds of particles are shown in Fig.4.26 and Fig.4.27, respectively. Fig.4.26 shows that the quality factor QF increases with R for high and low particle density. For high particle densities, diamond case exhibits a better quality than the circular and square cases. The reason is that filter with diamond fiber has the lowest pressure drop among three cases although filtration efficiency for square fiber is the largest one. However, for low particle densities, square fiber has the greatest quality factor concerning $R = 0.05$, and $\varepsilon = 600$. Then the QF of diamond and circular fiber increases remarkably compared with the square case, which indicates a better performance for $0.075 \leq R \leq 0.15$. Indeed, the filtration efficiency increases faster than pressure drop, which leads to a rise in quality factor.

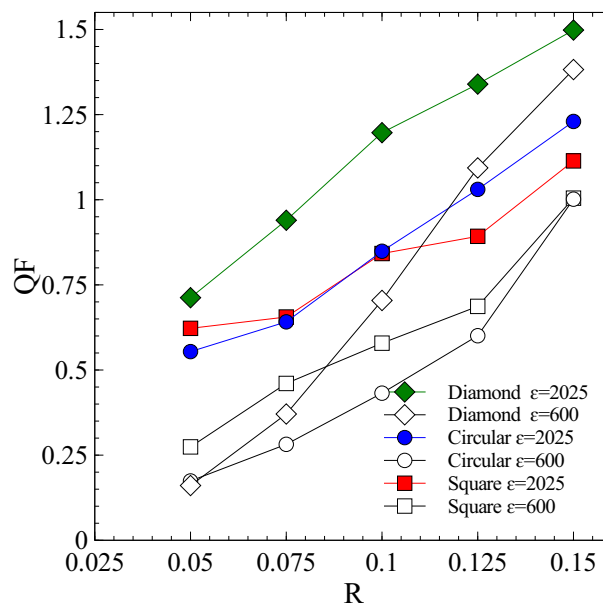
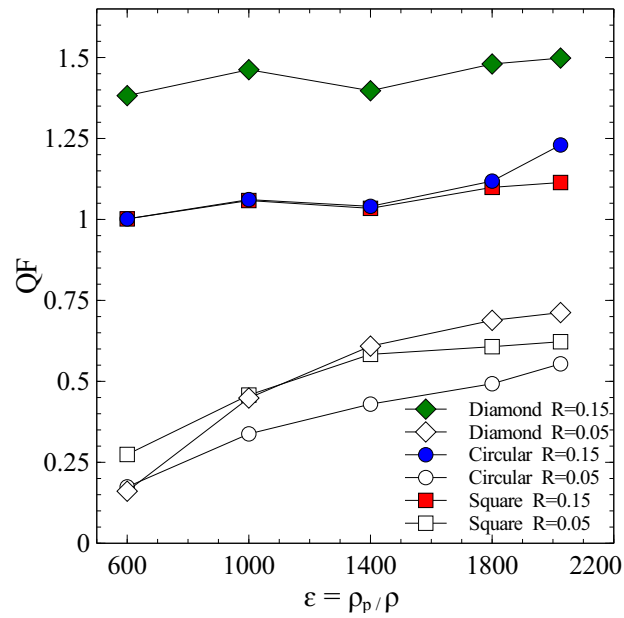
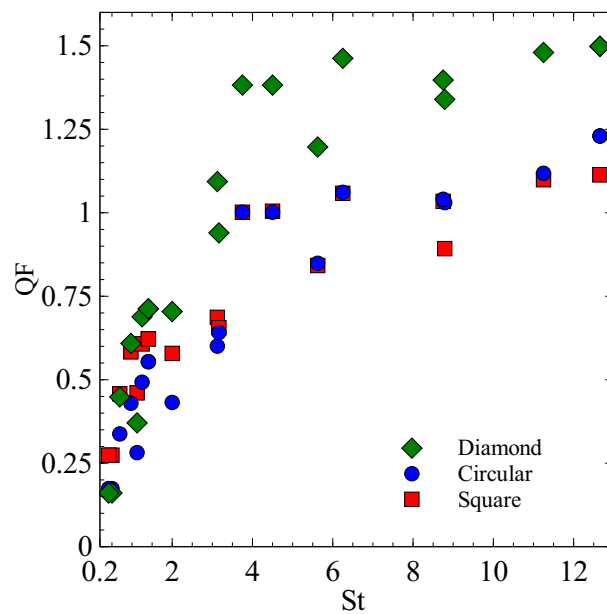


Figure 4.26: Quality factor QF as a function of R .

Fig.4.27 depicts the quality factor QF as a function of particle-to-fluid density ratio. It can be observed that quality factor of three fiber configurations is independent on particle-to-fluid density ratio for $R = 0.15$. However, for $R = 0.05$ the quality factor of three fiber increase with the particle-to-fluid density ratio. Generally, diamond case still indicates a better filtration performance at the same condition. Although square case has a higher

Figure 4.27: Quality factor QF as a function of ε .Figure 4.28: Quality factor QF as a function of St .

filtration efficiency than diamond case as seen in Fig.4.13 and Fig.4.14, it also leads to a higher pressure drop.

Fig.4.28 presents the relationship between quality factor and St for circular, diamond and square fiber. It demonstrates that St has the influence on quality factor for three types of fibers. Quality factor increases with St . For $St < 4$, the gap of QF for circular, diamond and square fibers is small. In the case of $St > 4$, this gap becomes obviously, especially for the case of the diamond and circular fibers. The higher quality factor of staggered diamond fibers is due to higher filtration efficiency and lower pressure drop.

4.4 Conclusions

In this chapter, firstly, three kinds of fiber arrangements, one beside the other, one underneath the other and staggered, are presented. The single fiber capture efficiency for different fiber arrangements is compared, from which the staggered configuration shows higher capture efficiency. Then, staggered circular fibers are used to validate our code, the simulation results agree well with the previous work. Finally, the filtration performance (pressure drop and filtration efficiency) of filter with three types of fibers (circular, diamond and square fibers) is evaluated using a two-way coupling method in staggered arrangement. The effect of pertinent parameters such as Reynolds number Re , R , ε , St on pressure drop and filtration efficiency were investigated at the initial stage of filtration. To obtain a high filtration efficiency and low pressure drop, the quality factor is used to characterize the filtration performance. The following conclusion can be drawn from this study:

Dimensionless drag force for three types of fibers is dependent on Reynolds number and linearly increased with it in the region of $2 \leq Re \leq 10$. Filter with staggered arranged diamond fiber has a lower pressure drop compared with circular and diamond cases, this accord with the results in chapter 3 when concerning single fiber or for arrangement of one beside the other.

The number of captured particles by three type of fibers increases for small particles when Reynolds number varies from 2 to 10. However the filtration efficiency for circular, diamond and square fibers is independent on Re for large particles.

The increases in parameter R leads to a higher filtration efficiency for three types of fibers. The filtration efficiency for circular and diamond fibers is more sensitive to the R than the square fiber.

The filtration efficiency for three type of fibers increases with the ε for small particle,

however it is independent on ε for large particle due to the strong inertial force. The injected particles are more easily captured by the square fiber than circular and diamond fibers.

Filtration efficiency of filter for circular, diamond and square fibers increases with the Stokes number and that this trend diminishes for larger Stokes numbers. The results also reveal that η for square fiber is larger than the one for circular and diamond cases when it arrives a constant value for a fixed St .

In terms of QF , filter with staggered arranged diamond fiber exhibits a better filtration performance for higher density ratio, large particle size and Stokes number. This result is the same for single fiber or for arrangement of one beside the other in chapter 3 when isolated particle and several particles are injected.

Conclusion and perspectives

General conclusions

In this thesis, numerical researches are performed to study and investigate the particle transport and deposition in porous media. A coupled lattice Boltzmann (LBM) and discrete element (DEM) methods to deal with fluid-particle interaction are presented. Filtration performance of filter including capture efficiency and pressure drop are analysed, where single fiber and multi-fiber with different cross-section shape are considered.

We introduced the principle of LBM, DEM as well as coupled of these two methods, where the LBM is employed to describe the fluid flow and the DEM is used to deal with the particle dynamics. With a series of model validations including the Poiseuille flow, Couette flow, flow around a fixed cylinder, Darcy law and Kozeny-Carmann equation, it has been demonstrated that the coupled LBM-DEM have the capability to deal with fluid-particle problems at the particle scale with quite good accuracy and that its implementation in the code used in this work is correct. Moreover, the code has been also validated with more complex validation test cases, by comparison of literature results on filtration experiments in chapter 3 and 4.

The single fiber capture efficiency for circular, diamond and square cross-section shape are numerically investigated for various Stokes number. The capture efficiency of these single fibers all increase with Stokes number. For capture efficiency of circular fiber, a good agreement with existing empirical correction proposed by Schweers et al. are observed for $0.5 \leq St \leq 3$. The square fiber is more favorable to capture the particle on the front side than the circular and diamond cases. However, diamond fiber exhibits a better filtration performance in terms of quality factor for both cases of one particle and several particles injected, which takes the pressure drop into account.

The influence of aspect ratio and orientation angle of rectangular fiber on filtration performance are also studied for various Reynolds number. It has been shown by Fardi

and Liu that pressure drop is independent of Reynolds number for $Re < 1$. With the complementary study conducted during this work, we put in evidence that the pressure drop for filter with rectangular fiber is dependent both the orientation angle and Reynolds number for $2 \leq Re \leq 10$. It increases with the Re for $\theta = 0$ whereas it decreases with the orientation angle for large windward area.

With respect to filtration efficiency, it linearly increased with windward area for $2.08 \leq St \leq 10.4$ due to the strong inertia. Through these analysis, the largest quality factor is obtained for square fiber at $\theta = 0$ or diamond fiber, which leads us to the same conclusion that filter with diamond fiber exhibits better filtration performance when several particles are injected.

In addition to the fiber geometry, the fiber arrangement has effect on the filtration performance. The staggered arranged fibers with circular, diamond and square cross-section are considered to determine the filtration efficiency and pressure drop of filter. The influence of parameters such as $R = \frac{d_p}{D_f}$, ratio of particle density to fluid density $\varepsilon = \frac{\rho_p}{\rho}$ and St on filtration performance are investigated. The increases in parameter R leads to a higher filtration efficiency for circular, diamond and square fiber. The filtration efficiency of filter with circular and diamond fibers is more sensitive to R than the square case. Filtration efficiency increases with ε for small particle, however it is independent on ε for large particle due to the strong inertial force. For small value of Stokes number, the filtration efficiency first increases rapidly and then increases at a relatively slower rate for filter with circular, diamond and square fibers. For large St , filtration efficiency arrives its maximum and becomes essentially independent of St . For filter with circular, diamond and square fibers staggered arranged, a higher quality factor is observed for staggered arranged diamond fibers for high density ratio, large particle size and Stokes number.

Globally, this work presents the numerical study on the particles transport and deposition in filter. Our investigation helps to analyse how particle and fluid properties determine the filtration performance and affect the particle filtration process. However, as a first step, to better understand such phenomenon, following aspects are recommended for further work.

This work investigates the particles transport at the initial stage of filtration, where the fiber shape is not effected by injected particles. This assumption is reasonable while these particles are very small compared to fiber or when system is quite dilute without a large number of particles. However, particle loading on the surface of fibers may not be neglected when filtration process is located at aging stage which corresponds to the

clogging of filter and the changes of fiber shape. With the particles attached on the surface of fiber, the pressure drop in aging stage will increase compared with initial stage. However, the filtration efficiency is not easy to predict due to the variation of fiber shape. Nevertheless the moving boundary can be implemented by LBM-DEM developed in this work, LBM-DEM has the capability to deal with such unsteady filtration process.

The study of particle dense case could be added. For particle-particle interactions, lubrication forces on the sliding particles may be calculated when two particles come to near contact in further research. The extend of this study to more dense cases can be performed with the model developed and used here. Indeed, using definitions presented in chapter 1, our model can be qualified as a four way coupling in the sense that interparticle interactions are already dealt by our program.

The coupled LBM-DEM model has been validated in this work in 2D. Extension of the LBM-DEM model for 3D could be considered for further simulations.

List of symbols

A	Cross-section area
C	Lattice speed (m/s)
C_u	Cunningham coefficient
d_p	Particle diameter (m)
D	Brownian diffusion coefficient
D_f	Fiber diameter (m)
\vec{e}_i	Discrete velocity (m/s)
E	Overall efficiency of a filter
f_i	Distribution function
f_i^{eq}	Equilibrium distribution functions
F^*	Dimensionless drag force
F_c	Contact force (N)
H	Filter width (m)
h	LBM grid spacing
J	Moment of inertia of particle ($\text{kg} \cdot \text{m}^2$)
k_B	Boltzmann constant
K_u	Hydrodynamic factor of Kuwabara's flow
Kn	Knudsen number
L	Filter length (m)
m	Particle mass (kg)
T	Temperature
Δp	Pressure drop (Pa/m)
Pe	Péclet number
Q	Volume flow rate (m^3/s)
QF	Quality factor
R	Intercept coefficient
Re	Reynolds number

St	Stokes number
\vec{U}	Fluid velocity (m/s)
\vec{u}_p	Particle velocity(m/s)
\vec{V}_D	Flow rate per unit area of the cross section (m/s)
\vec{V}_P	Fluid velocity through the pores (m/s)
x, y, z	Coordinates
ρ	Fluid density (kg/m ³)
ρ_p	Particle density (kg/m ³)
β	Fiber volume fraction
μ	Dynamic viscosity of fluid (Pa · s)
κ	Permeability of the medium
η	Filtration efficiency of filter
η_s	Single fiber capture efficiency
η_D	Capture efficiency due to diffusion
η_R	Capture efficiency due to interception
η_{DR}	Capture efficiency due to interception and diffusion
η_I	Capture efficiency due to inertial impaction
η_{IR}	Capture efficiency due to inertial impaction and interception
η_i	Capture contribution
τ	Relaxation time
τ_p	Particle response time
τ_k	Kolmogorov time scale
$\vec{\omega}$	Angular velocities (rad/s)
λ	Mean free path of gas molecules
χ_n	Overlap between two particles (m)
γ_n	Damping coefficient
ν	Kinematic viscosity of fluid (m ² /s)
θ	Orientation angle
ε	Density ratio between particle and fluid
ϕ	Porosity
Φ_s	Sphericity of the particles
Φ_p	Volume fraction of particles

List of Figures

1	Example of problem involving fluid-solid interactions: snapshots from the numerical simulation of piping erosion [8]. Particles are detached under the hydraulic loading. Then, detached particles are transported by the flow toward the channel outlet.	2
2	Example of problem fluid-solid involving interactions: gravity-driven flow [9], particles are represented in light gray and walls in dark gray. The yielded region of the fluid grows from a small portion to the whole sample. When a new equilibrium is reached, the yielded region reduces and the flow is slowed.	2
3	Filtration application, top: filtering stage and clean stage, bottom: particle separation process, n_{upstream} and $n_{\text{downstream}}$ represent the number of particle, at the upstream and downstream respectively [16].	4
1.1	Porosity type (a) intergranular porosity, (b) fracture porosity, (c) cavernous porosity [22].	10
1.2	The structures for stacks of monotonous spheres, a) SC , b) BCC, c) FCC, d) HCP.	11
1.3	Example of particle size distribution curve [30].	13
1.4	The threshold of particles trapped in a triangular construction [33].	14
1.5	(a) Cylinders with square unit cell. (b) Solution domain for exact solutions of streamfunction.	18
1.6	Cake filtration	20
1.7	Schematic view of granular filtration [43]	21
1.8	Schematic view of fibrous filter	21
1.9	Schematic representation of filter [14]	23
1.10	Filtration efficiency of filter (a) and efficiency of UBE (b)	24
1.11	Particle capture by Brownian diffusion	26

1.12	Particle capture by interception	28
1.13	Schematic representation of particle capture by inertial impaction	30
1.14	Capture efficiency of square block as a function of St	31
1.15	Filtration efficiency of filter versus particle diameter illustrating different capture mechanisms [70]	32
1.16	Retention sites (a) surface sites, (b) crevice sites, (c) constriction sites (d) cavern sites [71]	33
1.17	Map of flow regimes in particle-laden flows [74], Φ_p : volume fraction of particles, $\Phi_p = NV_p/V$, N : number of particles, V_p : volume of a single particles, V : volume occupied by particles and fluid, d_p : diameter of particle, τ_p : particle response time = $\rho_p d_p^2 / (18\rho_f \nu)$ for Stokes flow, τ_k : Kolmogorov time scale = $(\nu/\epsilon)^{1/2}$, where ρ_p and ρ_f are particle and fluid density, ϵ is the dissipation rate of turbulence kinetic energy, Stokes number is $St = \tau_p / \tau_k$	36
1.18	Scanning electron micrograph (SEM) of particles captured by the fibers [44].	40
1.19	Particles captured by different capture mechanisms, (a) diffusion ($Pe = 102$), (b) inertial impaction ($St = 1.61$), (c) interception ($R = 0.0357$) [112].	42
1.20	Particles trajectories in the regular and irregular structure filter for $Re = 5$ (a) regular structure filter, (b) irregular structure filter, [90].	43
2.1	Discrete velocities in the D2Q9 model.	49
2.2	A circular solid obstacle mapped on the LB lattice.	52
2.3	A boundary link.	52
2.4	LBM boundary conditions.	55
2.5	Schematic view of streaming step when using periodic boundary conditions.	57
2.6	Illustration of a collision between two particles with overlap χ_n	60
2.7	Flowchart of the coupled LBM and DEM.	64
2.8	Schematic view of 2D Poiseuille flow and boundary condition.	66
2.9	Comparison of velocity profile obtained with LBM and series solutions for Poiseuille flow at different times.	67
2.10	Schematic view of Couette flow in 2D and boundary condition.	69
2.11	Comparison of velocity profile obtained with LBM and series solutions for Couette flow at different times.	70
2.12	Schematic view of the problem of the flow around a circle between two parallel plats.	71

2.13	Velocity profiles obtained with LB methods and with CFD software for a fluid flowing around a circular cylinder, different values d/h of lattice are studied, where d is the cylinder diameter and h is the lattice spacing. . . .	72
2.14	Velocity field in porous media for $\Delta p = 0.4$ Pa	74
2.15	The relationship between discharge Q calculated at the outlet and the product of cross-sectional area and the pressure gradient($A \cdot \nabla p$) follows Darcy's law.	75
2.16	Discharge Q at the outlet is proportional to $\frac{\phi^3}{(1-\phi)^2}$ as in Kozeny-Carman relation.	75
2.17	Schematic view of cylinder moving with a constant velocity applied and boundary condition.	76
2.18	Drag coefficient as a function of Reynolds number of cylinder	77
3.1	Particle trajectory and deposition on a single fiber.	81
3.2	Schematic drawing of fluid velocities at one lattice in LBM.	84
3.3	Particle trajectories with the corresponding streamlines around the fiber for (a) $St = 0.001$, (b) $St = 0.03$ (c) $St = 0.3$, (d) $St = 0.5$, (e) $St = 1$, (f) $St = 1.5$	85
3.4	Particle capture efficiency on fiber as a function of the Stokes number St . The result is compared with the work of Araujo et al [148].	86
3.5	Single fiber capture efficiency as a function of ratio between the particle diameters d_p and fiber diameter D_f obtained from one-way and two-way coupling methods, respectively.	87
3.6	Schematic view of structure of (a) circular fibers (b) diamond fibers (c) square fibers.	88
3.7	Single fiber capture efficiency of isolated particle for fiber with three different shapes.	89
3.8	Trajectories of particle with streamlines for circular, diamond and square fiber	90
3.9	Quality factor as function of St for isolated particle injected.	91
3.10	A steady state velocity vector of flow around a circular fiber calculated with LB method	93
3.11	Velocity field of fluid and particle distribution for $St=0.5$	94
3.12	Comparison between capture efficiency of single circular fiber obtained from numerical method (LBM-DEM) and from the empirical correlations. $Re = 6.8$, $R = 0.0625$	95

3.13	Particles distribution with square and diamond fiber for $St = 0.5$	97
3.14	Front side of fiber is divided by 9 parts from 1 to 9.	98
3.15	Particles distribution on the front side of circular, diamond and square fiber for $St = 1.97$	98
3.16	Single fiber capture efficiency as a function of Stokes number St with different fiber shapes.	99
3.17	Quality factor as a function of Stokes number St with different fiber shapes.	100
3.18	Schematic view of computational domain for simulating flow field around rectangular fiber.	101
3.19	Dimensionless drag force as a function of volume fraction, LB simulation results are presented and compared with the work of Ouyang and Liu [154].	103
3.20	Dimensionless drag force as a function of fiber Reynolds number for $\theta = 0$.	103
3.21	Streamlines around rectangular fiber with an aspect ratio of $w/b = 2$ and orientation angles (a) $\theta = 0$, (b) $\theta = \pi/8$, (c) $\theta = \pi/4$, (d) $\theta = 3\pi/8$, (e) $\theta = \pi/2$, $Re = 8$	104
3.22	Windward area with orientation angle θ	105
3.23	The cross-section area of rectangular fiber	106
3.24	Dimensionless drag force as a function of orientation angle, $Re = 8$	106
3.25	Dimensionless drag force as a function of cross section l_c , $Re = 8$	107
3.26	Filtration efficiency of filter as a function of Reynolds number for $\theta = 0$	108
3.27	Velocity field of fluid and particle positions for $St = 8.33$, $Re = 8$, (a) $\theta = 0$, (b) $\theta = 1/8\pi$, (c) $\theta = 1/4\pi$, (d) $\theta = 3/8\pi$, (e) $\theta = 1/2\pi$	109
3.28	Filtration efficiency as a function of orientation angle for $Re = 8$	110
3.29	Filtration efficiency as a function of cross-section area of rectangular fiber for $Re=8$ and different orientation angles, $w/b = 1, 2, 3, 4$	111
3.30	Filtration efficiency as a function of cross-section area of rectangular fiber for different Re and different orientation angles, $w/b = 1, 2, 3, 4$	111
3.31	Quality factor of filter as a function of Re for $\theta = 0$	112
3.32	Quality factor as a function of orientation angle.	113
3.33	Quality factor as a function of l_c for $Re = 8$	113
3.34	Quality factor as a function of l_c for different Re . For $Re = 8$, the orientation angles $\theta = 0, \pi/8, \pi/4, 3\pi/8, \pi/2$, for $Re = 2, 4, 6, 10$, $\theta = 0$	114
4.1	Fiber arrangements (a) one beside the other, (b) one underneath the other, (c) staggered.	118

4.2	Single fiber capture efficiency as a function of Stokes number with different fiber arrangements.	119
4.3	A schematic diagram of the staggered structure of circular fibers	120
4.4	Dimensionless drag force as a function of (a) Reynolds number Re , (b) volume fraction β and (c) separation ratio $l_0/2w_0$ for circular fibers.	121
4.5	Schematic view of structure of staggered model of filters with (a) circular fibers (b) diamond fibers (c) square fibers.	123
4.6	Streamlines around fibers with (a) circular (b) diamond and (c) square cross-sectional shape for $Re = 5$, $l_0 = 0.0008$ m, $w_0 = 0.0005$ m, $D_f = 0.0004$ m.	125
4.7	Dimensionless drag force versus Re applied on the circular, diamond and square fibers.	125
4.8	Filtration efficiency versus Reynolds number for $R = 0.05$ and density ratio $\varepsilon = 2025$	127
4.9	Filtration efficiency versus Reynolds number for $R = 0.15$ and density ratio $\varepsilon = 2025$	127
4.10	Instantaneous velocity field and particle distribution for filter with circular, diamond and square fibers for $Re = 5$, $R = 0.05$ and $\varepsilon = 2025$	128
4.11	Filtration efficiency versus intercept coefficient R , density ratio $\varepsilon = 600$ and $Re = 5$	129
4.12	Filtration efficiency versus intercept coefficient R , density ratio $\varepsilon = 2025$ and $Re = 5$	130
4.13	Filtration efficiency versus density ratio $\varepsilon = \rho_p/\rho$ for $R = 0.05$ and $Re = 5$	131
4.14	Filtration efficiency versus density ratio $\varepsilon = \rho_p/\rho$ for $R = 0.15$ and $Re = 5$	131
4.15	Filtration efficiency of filter with circular fiber as a function of St	132
4.16	Filtration efficiency of filter with diamond fiber as a function of St	132
4.17	Filtration efficiency of filter with square fiber as a function of St	133
4.18	Filtration efficiency of filter with circular, diamond and square fiber as a function of St	133
4.19	Capture contribution of fiber as a function of Re for $R = 0.05$ and $\varepsilon = 2025$	134
4.20	Capture contribution of fiber as a function of Re for $R = 0.15$ and $\varepsilon = 2025$	135
4.21	Capture contribution of fiber as a function of R for $Re = 5$ and $\varepsilon = 600$	136
4.22	Capture contribution of fiber as a function of R for $Re = 5$ and $\varepsilon = 2025$	137
4.23	Capture contribution of fiber as a function of ε for $Re = 5$ and $R = 0.05$	137

4.24	Capture contribution of fiber as a function of ε for $Re = 5$ and $R = 0.15$. . .	138
4.25	Capture contribution of circular, diamond and square fibers as a function of St	138
4.26	Quality factor QF as a function of R	139
4.27	Quality factor QF as a function of ε	140
4.28	Quality factor QF as a function of St	140
4.29	Comparaison du profil de vitesse obtenu avec la LBM et des solutions en série pour l'écoulement de Poiseuille et l'écoulement de Couette.	174
4.30	Profils de vitesse obtenus avec la méthode LBM et avec un logiciel CFD pour un écoulement de fluide circulant autour d'un cylindre circulaire . . .	174
4.31	Champ de vitesse du fluide et position des particules dans les cas d'écoulements autour de fibres de sections différentes (circulaire, carrée et diamantée), pour $St = 0.5$	175
4.32	Champ de vitesse du fluide et distribution des particules pour $St = 8.33$, $Re = 8$, (a) $\theta = 0$, (b) $\theta = 1/8\pi$, (c) $\theta = 1/4\pi$, (d) $\theta = 3/8\pi$, (e) $\theta = 1/2\pi$	176
4.33	Facteur de qualité en fonction de Re , $\theta = 0$ (a). Facteur de qualité en fonction de l'angle d'orientation, $Re = 8$ (b)	177
4.34	Représentation des lignes de courant autour des fibres de sections transversales différentes (circulaire, losange et carré).	179
4.35	Facteur de qualité QF en fonction de a) R et b) ε	180

Bibliography

- [1] L. M. McDowell-BOYER, J. R. Hunt, and N. Sitar. Particle transport through porous media. *Water Resources Research*, 22(13):1901–1921, 1986.
- [2] S. M. B. Tehrani, A. Moosavi, and H. Sadrhosseini. Filtration of aerosol particles by cylindrical fibers within a parallel and staggered array. *Microsystem Technologies*, 2015.
- [3] G. Kampel, G. Goldsztein H, and J. C. Santamarina. Particle transport in porous media: The role of inertial effects and path tortuosity in the velocity of the particles. *Applied Physics Letters*, 95(19):2013–2016, 2009.
- [4] L. Wang, B. Zhang, X. Wang, W. Ge, and J. Li. Lattice Boltzmann based discrete simulation for gas-solid fluidization. *Chemical Engineering Science*, 101:228–239, 2013.
- [5] X. Cui, J. Li, A. Chan, and D. Chapman. Coupled DEM-LBM simulation of internal fluidisation induced by a leaking pipe. *Powder Technology*, 254:299–306, 2014.
- [6] Edouard, I. *Modélisation numérique des écoulements granulaires denses immergés dans un fluide*. PhD thesis, Institut National Polytechnique de Toulouse, 2014.
- [7] E. J. Ding and C. K. Aidun. Extension of the lattice-Boltzmann method for direct simulation of suspended particles near contact. *Journal of Statistical Physics*, 112(3-4):685–708, 2003.
- [8] F. Lominé, L. Scholtès, L. Sibille, and P. Poullain. Modeling of fluid-solid interaction in granular media with coupled lattice Boltzmann/discrete element methods: application to piping erosion. *International Journal for Numerical and Analytical Methods in Geomechanics*, 37(6):577–596, 2013.

- [9] A. Leonardi, F. K. Wittel, M. Mendoza, and H. J. Herrmann. Coupled DEM-LBM method for the free-surface simulation of heterogeneous suspensions. *Computational Particle Mechanics*, 1(1):3–13, 2014.
- [10] H. C. Yeh and B. Y. H. Liu. Aerosol filtration by fibrous filters - I. Theoretical. *Journal of Aerosol Science*, 5, 1974.
- [11] J. Wang and D. Y. H. Pui. Filtration of aerosol particles by elliptical fibers: A numerical study. *Journal of Nanoparticle Research*, 11(1):185–196, 2009.
- [12] L. Arenzana, R. J. Krizek, and S. F. Pepper. *Injection of dilute microfine cement suspensions into fine sands*, volume 2, pages 1331–1334. Publ by A.A. Balkema, 1989.
- [13] J. N. Ryan and M. Elimelech. Colloid mobilization and transport in groundwater. *Colloids and Surfaces A: Physicochemical and Engineering Aspects*, 107(95):1–56, 1996.
- [14] C. Tien and B. V. Ramarao. *Granular filtration of aerosols and hydrosols*. Elsevier Science & Technology Books, 2007.
- [15] Y. Deng, J. Fan, S. Zhou, T. Zhou, J. Wu, Yin Li, Z. Liu, M. Xuan, and Y. Wua. Euler force actuation mechanism for siphon valving in compact disk-like microfluidic chips. *Biomicrofluidics*, 8(2), 2014.
- [16] E. Ringholm. *Understanding filter beta ratios*, 2017. <http://www.machinerylubrication.com/Read/564/filter-beta-ratios>.
- [17] Y. Wang and D. Adhikary. Hydraulic fracture simulation based on coupled discrete element method and lattice Boltzmann. *World Geothermal Congress 2015*, 5(May):1–5, 2015.
- [18] S. V. Patankar. *Numerical heat transfer and fluid flow*. Hemisphere Pub. Washington, 1980.
- [19] Q. Zou and X. He. On pressure and velocity boundary conditions for the lattice Boltzmann BGK model. *Physics of Fluids*, 9(6):1591–1598, 1997.

-
- [20] T. Crowe Clayton, D. Schwarzkopf John, Sommerfeld Martin, and Tsuji Yutaka. *Multiphase flows with droplets particles*. Taylor & Francis Group, second edition, 2012.
- [21] J. Happel and H. Brenner. *Low Reynolds number hydrodynamics*. Martinus Nijhoff, 1983.
- [22] <http://itc.gsw.edu/faculty/bcarter/physgeol/gw/pores.htm>.
- [23] J. N. Roberts and L. M. Schwartz. Grain consolidation and electrical conductivity in porous media. *Physical Review B*, 31(9):5990–5997, 1985.
- [24] J. J. L. Higdon and G. D. Ford. Permeability of three-dimensional models of fibrous porous media. *Journal of Fluid Mechanics*, 308(-1):341, 1996.
- [25] C. D. Lorenz, R. May, and R. M. Ziff. Similarity of percolation thresholds on the HCP and FCC lattices. *Journal of Statistical Physics*, 98(3-4):961–970, 2000.
- [26] R. E. Larson and J. J.L. Higdon. A periodic grain consolidation model of porous media. *Physics of Fluids A*, 1(1):38–46, 1989.
- [27] J. M. Valverde and A. Castellanos. Random loose packing of cohesive granular materials. *Europhysics Letters*, 75(6):985–991, 2006.
- [28] G. Y. Onoda and E. G. Liniger. Random loose packings of uniform spheres and the dilatancy onset. *Physical Review Letters*, 64(22):2727–2730, 1990.
- [29] L. M. Araya and J. F. Paris. A physicoempirical model to predict the soil moisture characteristic from particle-size distribution and bulk density data. *Soil Sci. Soc. Am. J.*, 45:1023–1030, 1981.
- [30] M. D Fredlund, D. G Fredlund, and G. W Wilson. Prediction of the soil-water characteristic curve from grain-size distribution and volume-mass properties. *Canadian geotechnical journal*, 39(5):1103, 1997.
- [31] S. W. Tyler and S. W. Wheatcraft. Fractal Scaling of Soil Particle-Size Distributions: Analysis and Limitations. *Soil Science Society of America Journal*, 56(2):362, 1992.
- [32] D. G Fredlund and A. Xing. Equations for the soil-water characteristic curve. *Can. Geotechn. J.*, 31:521–532, 1994.

- [33] J. P. Herzig, D. M. Leclerc, and P. Le Goff. Flow of suspensions through porous media—application to deep filtration. *Industrial and Engineering Chemistry*, 62(5):8–35, 1970.
- [34] A. Nabovati, E. W. Llewellyn, and A. C. M. Sousa. A general model for the permeability of fibrous porous media based on fluid flow simulations using the lattice Boltzmann method. *Composites Part A: Applied Science and Manufacturing*, 40(6–7):860–869, July 2009.
- [35] M. Hellou, J. Martinez, and M. El Yazidi. Stokes flow through microstructural model of fibrous media. *Mechanics Research Communications*, 31(1):97–103, 2004.
- [36] M. Hellou. *Etude numerique and experimentale de l'écoulement à structure cellulaire, engendré par la rotation d'un cylindre dans un canal*. PhD thesis, Université de Poitiers, France, 1988.
- [37] S. Kuwabara. The forces experienced by randomly distributed parallel circular cylinders or spheres in a viscous flow at small Reynolds numbers. *Journal of the Physical Society of Japan*, 14:527–537, 1959.
- [38] H. Marshall, M. Sahraoui, and M. Kaviani. An improved analytic solution for analysis of particle trajectories in fibrous, two-dimensional filters. *Physics of Fluids*, 6(2):507, 1994.
- [39] C. Tien. *Introduction to the cake filtration: Analyses, Experiments and Applications*. Elsevier, 2006.
- [40] C. Tien, R. Bai, and B. V. Ramarao. Analysis of cake growth in cake filtration: Effect of fine particle retention. *AIChE Journal*, 43(1):33–44, 1997.
- [41] F. Civan. Practical model for compressive cake filtration including fine particle invasion. *AIChE Journal*, 44(1):2388–2398, 1998.
- [42] R. Kolakaluri, E. Murphy, S. Subramaniam, R. C. Brown, and R. O. Fox. Filtration model for polydisperse aerosols in gas-solid flow using granule-resolved direct numerical simulation. *AIChE Journal*, 61:3594–3606, 2009.
- [43] D. C. Mays. Contrasting clogging in granular media filters, soils, and dead-end membranes. *Journal of Environmental Engineering*, 136(5):475–480, May 2010.

-
- [44] E. Schweers, H. Umhauer, and F. Löffler. Experimental investigation of particle collection on single fibres of different configurations. *Particle and Particle Systems Characterization*, 11:275–283, 1994.
- [45] H. Rembor, R. Maus, and H. Umhauer. Measurements of single fibre efficiencies at critical values of the Stokes number. *Particle and Particle Systems Characterization*, 16:54–59, 1999.
- [46] N. E. L. Haugen and S. Kragset. Particle impaction on a cylinder in a crossflow as function of Stokes and Reynolds numbers. *Journal of Fluid Mechanics*, 661:239–261, 2010.
- [47] H. Wang, H. Zhao, Z. Guo, and C. Zheng. Numerical simulation of particle capture process of fibrous filters using Lattice Boltzmann two-phase flow model. *Powder Technology*, 227:111–122, 2012.
- [48] W. C. Hinds. *Aerosol technology*. Wiley- interscience, 1998.
- [49] R. C. Flagan and J. H. Seinfeld. *Fundamentals of air pollution engineering*. Prentice-Hall: Englewood Cliffs, 1988.
- [50] F. Qian, J. Zhang, and Z. Huang. Retraction: Effects of the operating conditions and geometry parameter on the filtration performance of the fibrous filter. *Chemical Engineering and Technology*, 38(5):789–797, 2009.
- [51] S. A. Hosseini and H. V. Tafreshi. Modeling particle filtration in disordered 2-D domains: A comparison with cell models. *Separation and Purification Technology*, 74(2):160–169, 2010.
- [52] D. C. Mays and J. R. Hunt. Hydrodynamic aspects of particle clogging in porous media. *Environmental Science and Technology*, 39(2):577–584, 2005.
- [53] J. Wang, D. R. Chen, and D. Y. H. Pui. Modeling of filtration efficiency of nanoparticles in standard filter media. *Journal of Nanoparticle Research*, 9(1):109–115, 2007.
- [54] A. Li and G. Ahmadi. Dispersion and deposition of spherical particles from point sources in a turbulent channel flow. *Aerosol Science and Technology*, 16(4):209–226, 1992.

- [55] I. B. Stechkina and N. A. Fuchs. Studies on fibrous aerosol filters - I. Calculation of diffusional deposition of aerosols in fibrous filters. *Annals of Occupational Hygiene*, 12(9):59–64, 1966.
- [56] K. W. Lee and B. Y. H. Liu. Theoretical study of aerosol filtration by fibrous filters. *Aerosol Science and Technology*, 1(2):147–161, 1982.
- [57] C. Wang and Y. Otani. Removal of nanoparticles from gas streams by fibrous filters: A review. *Industrial and Engineering Chemistry Research*, 52(1):5–17, 2013.
- [58] Z. G. Liu and P. K. Wang. Pressure drop and interception efficiency of multifiber filters. *Aerosol Science and Technology*, 26(4):313–325, 1997.
- [59] C. Zhu, C. Lin, and C. S. Cheung. Inertial impaction-dominated fibrous filtration with rectangular or cylindrical fibers. *Powder Technology*, 112(1-2):149–162, 2000.
- [60] J. Payen, P. Vroman, M. Lewandowski, A. Perwuelz, S. Calle-Chazelet, and D. Thomas. Influence of fiber diameter, fiber combinations and solid volume fraction on air filtration properties in nonwovens. *Textile Research Journal*, 82:1948–1959, 2012.
- [61] R. Israel and D. E. Rosner. Use of a generalized Stokes number to determine the aerodynamic capture efficiency of Non-Stokesian particles from a compressible gas Flow. *Aerosol Science and Technology*, 2(1):45–51, 1982.
- [62] H. D Landahl and R. G Herrmann. Sampling of liquid aerosols by wires, cylinders, and slides, and the efficiency of impaction of the droplets. *Journal of colloid science*, 4(2):103–36, 1949.
- [63] I. B. Stechkina, A. A. Kirsch, and N. A. Fuchs. Studies in fibrous aerosol filters – IV. Calculation of aerosol deposition in model filters in the range of maximum penetration. *Annals of Occupational Hygiene*, 12(3):1–8, 1969.
- [64] R. C. Brown. *Air Filtration*. Pergamon Press, Oxford, 1993.
- [65] C. N. Davies. The separation of airborne dust and particles. *Proceedings of the Institution of Mechanical Engineers, Part B: Management and engineering manufacture*, 1(1-12):185–213, 1953.

-
- [66] S. K. Suneja and C. H. Lee. Aerosol filtration by fibrous filters at intermediate Reynolds numbers (<100). *Atmospheric Environment*, 8(11):1081–1094, 1974.
- [67] D. J. Brandon and S. K. Aggarwal. A numerical investigation of particle deposition on a square cylinder placed in a channel flow. *Aerosol Science and Technology*, 34(4):340–352, 2001.
- [68] M. Salmanzadeh, M. Rahnama, and G. Ahmadi. Particle transport and deposition in a duct flow with a rectangular obstruction. *Particulate Science and Technology*, 25(5):401–412, 2007.
- [69] S. Jafari, M. Salmanzadeh, M. Rahnama, and G. Ahmadi. Investigation of particle dispersion and deposition in a channel with a square cylinder obstruction using the lattice Boltzmann method. *Journal of Aerosol Science*, 41(2):198–206, 2010.
- [70] K. W. Lee and B. Y. H. Liu. On the minimum efficiency and the most penetrating particle size for fibrous filters. *Journal of the Air Pollution Control Association*, 30(4):377–381, 1980.
- [71] Y. Delanchambr. *Contribution à l'étude de l'écoulement d'une suspension à travers un milieu poreux et du mécanisme de la filtration*. PhD thesis, Université de Nancy, France, 1966.
- [72] C. N. Davies. *Air filtration*. Academic Press, London, 1973.
- [73] G. W. Jackson and D. F. James. The permeability of fibrous porous media. *The Canadian Journal of Chemical Engineering*, 64(3):364–374, 1986.
- [74] S. Elghobashi. On predicting particle-laden turbulent flows. *Applied Scientific Research*, 52(4):309–329, 1994.
- [75] O. Filippova and D. Hänel. Lattice-Boltzmann simulation of gas-particle flow in filters. *Computers & Fluids*, 26(7):697–712, 1997.
- [76] H. Wang, H. Zhao, Z. Guo, Y. He, and C. Zheng. Lattice Boltzmann method for simulations of gas-particle flows over a backward-facing step. *Journal of Computational Physics*, 239:57–71, 2013.
- [77] C. Shin. Finite element simulation of deep bed filtration. *Chemical Engineering Science*, 61(8):2324–2329, 2006.

- [78] Z. Sun, R. E. Logé, and M. Bernacki. 3D finite element model of semi-solid permeability in an equiaxed granular structure. *Computational Materials Science*, 49(1):158–170, 2010.
- [79] M. Breuer, J. Bernsdorf, T. Zeiser, and F. Durst. Accurate computations of the laminar flow past a square cylinder based on two different methods: Lattice-Boltzmann and finite-volume. *International Journal of Heat and Fluid Flow*, 21(2):186–196, 2000.
- [80] L. Chen, H. Luan, Y. Feng, C. Song, Y. He, and W. Tao. Coupling between finite volume method and lattice Boltzmann method and its application to fluid flow and mass transport in proton exchange membrane fuel cell. *International Journal of Heat and Mass Transfer*, 55(13-14):3834–3848, 2012.
- [81] A. S. Sangani and A. Acrivos. Slow flow past periodic arrays of cylinders with application to heat transfer. *Int.J.Multiphase Flow*, 8(3):193–206, 1982.
- [82] J. P. Morris, P. J. Fox, and Y. Zhu. Modeling low Reynolds number incompressible flows using SPH. *Journal of Computational Physics*, 136(1):214–226, September 1997.
- [83] J. W. Swegle, D. L. Hicks, and S. W. Attaway. Smoothed particle hydrodynamics stability analysis. *Journal of Computational Physics*, 116(1):123–134, 1995.
- [84] A. Valizadeh and J. Monaghan. SPH simulation of 2D turbulence driven by a cylindrical stirrer. *European Journal of Mechanics - B/Fluids*, 51:44–53, 2015.
- [85] A. J. C. Ladd and R. Verberg. Lattice-Boltzmann simulations of particle-fluid suspensions. *Journal of Statistical Physics*, 104(5):1191–1251, 2001.
- [86] Z. Guo and T. Zhao. Lattice Boltzmann model for incompressible flows through porous media. *Physical Review E*, 66(3):1–9, September 2002.
- [87] R. Przekop, A. Moskal, and L. Gradoń. Lattice-Boltzmann approach for description of the structure of deposited particulate matter in fibrous filters. *Journal of Aerosol Science*, 34(2):133–147, 2003.
- [88] A. Grucelski and J. Pozorski. Lattice Boltzmann simulations of flow past a circular cylinder and in simple porous media. *Computers & Fluids*, 71:406–416, January 2013.

-
- [89] P. Niedoba, L. Čermak, and M. Jícha. Meshfree methods for computational fluid dynamics. *EPJ Web of Conferences*, 45:1–6, 2013.
- [90] V. Ansari, A. S. Goharrizi, S. Jafari, and B. Abolpour. Numerical study of solid particles motion and deposition in a filter with regular and irregular arrangement of blocks with using Lattice Boltzmann method. *Computers and Fluids*, 108:170–178, 2015.
- [91] H. Cheng, J. Cheng, and G. Yeh. A particle tracking technique for the Lagrangian-Eulerian finite element method in multi-dimensions. *International Journal for Numerical Methods in Engineering*, 39(11):15–1, 1996.
- [92] S. Chen, C. S. Cheung, C. K. Chan, and C. Zhu. Numerical simulation of aerosol collection in filters with staggered parallel rectangular fibres. *Computational Mechanics*, 28(2):152–161, 2002.
- [93] P. A. Cundall and O. D. Strack. A discrete numerical model for granular assemblies. *Geomechanics*, 29(1):47–65, 1979.
- [94] S. Luding. Introduction to discrete element methods. Basic of contact force models and how to perform the micro-macro transition to continuum theory. *European Journal of Environmental and Civil Engineering*, 12:785–826, 2008.
- [95] Z. Feng and E. E. Michaelides. The immersed boundary-lattice Boltzmann method for solving fluid-particles interaction problems. *Journal of Computational Physics*, 195(2):602–628, 2004.
- [96] Y. T. Feng, K. Han, and D. R. J. Owen. Coupled lattice Boltzmann method and discrete element modelling of particle transport in turbulent fluid flows : Computational issues. *International journal for numerical methods in engineering*, 72(June):1111–1134, 2007.
- [97] L. Jing and J. A. Hudson. Numerical methods in rock mechanics. *International Journal of Rock Mechanics & Mining Sciences*, 39(4):409–427, 2002.
- [98] F. Lominé and L. Oger. Transport of small particles through a 3D packing of spheres: experimental and numerical approaches. *Journal of Statistical Mechanics: Theory and Experiment*, 2006(07):P07019–P07019, July 2006.

- [99] T. W. Han. *Experimental and numerical studies of aerosol penetration through screens*. PhD thesis, Texas A&M University, 2013.
- [100] J. A. Harrop and J. I.T. Stenhouse. The theoretical prediction of inertial impaction efficiencies in fibrous filters. *Chemical Engineering Science*, 24(7):1475–1481, 1969.
- [101] D. H. Michael and P. W. Norey. Particle collision efficiencies for a sphere. *Journal of Fluid Mechanics*, 37(3):565–575, 1969.
- [102] C. Wang, M. Beizaie, and C. Tien. Deposition of solid particles on a collector: Formulation of a new theory. *AIChE Journal*, 23(6):879–889, 1977.
- [103] J. B. Wong, W. E. Ranz, and H. F. Johnstone. Inertial impaction of aerosol particles on cylinders. *Journal of Applied Physics*, 26(2):244–249, 1955.
- [104] K. R. May and R. Clifford. The impaction of aerosol particles on cylinders, spheres, ribbons and discs. *Annals of Occupational Hygiene*, 10(2):83–95, 1967.
- [105] K. W. Lee and B. Y. H. Liu. Theoretical Study of Aerosol Filtration by Fibrous Filters. *Aerosol Science and Technology*, 1(2):147–161, 1982.
- [106] S. A. Hosseini and H. Vahedi Tafreshi. On the importance of fibers’ cross-sectional shape for air filters operating in the slip flow regime. *Powder Technology*, 212(3):425–431, 2011.
- [107] V. A. Kirsh. Stokes flow and deposition of aerosol nanoparticles in model filters composed of elliptic fibers. *Colloid Journal*, 73(3):345–351, 2011.
- [108] H. Wang, H. Zhao, K. Wang, and C. Zheng. Simulating and modeling particulate removal processes by elliptical fibers. *Aerosol Science and Technology*, 48(2):207–218, 2014.
- [109] H. Huang, K. Wang, and H. Zhao. Numerical study of pressure drop and diffusional collection efficiency of several typical noncircular fibers in filtration. *Powder Technology*, 292:232–241, 2016.
- [110] C. Y. Wang. Stokes flow through an array of rectangular fibers. *International Journal of Multiphase Flow*, 22(1):185–194, 1996.

-
- [111] B. Fardi and B.Y. H. Liu. Efficiency of fibrous filters with rectangular fibers. *Aerosol Science and Technology*, 17(1):45–58, 1992.
- [112] H. Wang, H. Zhao, K. Wang, Y. He, and C. Zheng. Simulation of filtration process for multi-fiber filter using the Lattice-Boltzmann two-phase flow model. *Journal of Aerosol Science*, 66:164–178, 2013.
- [113] K. C. Lin, H. Tao, and K. Lee. An early stage of aerosol particle transport in flows past periodic arrays of clear staggered obstructions: A computational study. *Aerosol Science and Technology*, 48(12):1299–1307, 2014.
- [114] B. Fardi and B. Y. H. Liu. Flow field and pressure drop of filters with rectangular fibers. *Aerosol Science and Technology*, 17(1):36–44, 1992.
- [115] U. Frisch, B. Hasslacher, and Y. Pomeau. Lattice as automata for the Navier-Stokes equation. *Physical Review Letters*, pages 1505–1508, 1986.
- [116] U. Frisch, D. D’Humières, B. Hasslacher, P. Lallemand, Y. Pomeau, and J. P. Rivet. Lattice gas hydrodynamics in two and three dimensions. *Complex Systems*, 1:649–707, 1987.
- [117] D. Enskog. *Kinetische theorie der vorgänge in mässig verdünnten gasen*. PhD thesis, Uppsala, 1917.
- [118] TG. Chapman, S. Cowling. *The mathematical theory of Non-uniform gases: An account of the kinetic theory of viscosity, thermal conduction and diffusion in gases*. Cambridge University Press: Cambridge, New York, Melbourne, 1991.
- [119] J. Hardy, Y. Pomeau, and O. de Pazzis. Time evolution of a two-dimensional model system. I. Invariant states and time correlation functions. *Journal of Mathematical Physics*, 14(12):1746, 1973.
- [120] J. Hardy, O. De Pazzis, and Y. Pomeau. Molecular dynamics of a classical lattice gas: Transport properties and time correlation functions. *Physical Review A*, 13(5):1949–1961, 1976.
- [121] D. D’Humières, P. Lallemand, and U. Frisch. Lattice gas models for 3D hydrodynamics. *Europhysics Letters (EPL)*, 2(4):291–297, 1986.

- [122] G. R. McNamara and G. Zanetti. Use of the boltzmann equation to simulate lattice-gas automata. *Physical Review Letters*, 61(20):2332–2335, 1988.
- [123] J. M. Bernsdorf. *Simulation of Complex Flows and Multi-Physics with the Lattice-Boltzmann Method*. PhD thesis, University of Amsterdam, 2008.
- [124] F. J. Higuera and J. Jiménez. Boltzmann approach to lattice gas simulations. *Europhysics Letters (EPL)*, 9(7):663–668, 1989.
- [125] J. M. V. A. Koelman. A simple Lattice Boltzmann scheme for Navier-Stokes fluid flow. *Europhysics Letters (EPL)*, 15(6):603–607, 1991.
- [126] S. Chen, H. Chen, D. Martnez, and W. Matthaeus. Lattice Boltzmann model for simulation of magnetohydrodynamics. *Physical Review Letters*, 67(27):3776–3779, 1991.
- [127] H. Chen, S. Chen, and W. H. Matthaeus. Recovery of the Navier-Stokes equations using a lattice-gas Boltzmann method. *Physical Review A*, 45(8):5339–5342, 1992.
- [128] P. L. Bhatnagar, E. P. Gross, and M. Krook. A model for collision processes in gases. I. Small amplitude processes in charged and neutral one-component systems. *Physical Review*, 94(3):511–525, 1954.
- [129] D. Yu, R. Mei, L. Luo, and S. Wei. Viscous flow computations with the method of lattice Boltzmann equation. *Progress in Aerospace Sciences*, 39(5):329–367, July 2003.
- [130] E. S. Boek and M. Venturoli. Lattice-Boltzmann studies of fluid flow in porous media with realistic rock geometries. *Computers and Mathematics with Applications*, 59(7):2305–2314, April 2010.
- [131] L. Wang, Z. Guo, B. Shi, and C. Zheng. Evaluation of three lattice Boltzmann models for particulate flows. *Communications in Computational Physics*, 13(4):1151–1171, 2013.
- [132] C. Pan, L. Luo, and C. T. Miller. An evaluation of lattice Boltzmann schemes for porous medium flow simulation. *Computers & Fluids*, 35(8-9):898–909, September 2006.

-
- [133] Y. H. Qian, D. D’Humières, and P. Lallemand. Lattice BGK models for Navier-Stokes equation. *EPL (Europhysics Letters)*, 17:479–484, 1992.
- [134] M. A. Gallivan, D. R. Noble, J. G. Georgiadis, and R. O. Buckius. An evaluation of the bounce-back boundary condition for lattice Boltzmann simulations. *International journal for numerical methods in fluids*, 25(June 1996):249–263, 1997.
- [135] X. He, Q. Zou, L. Luo, and M. Dembo. Analytic solutions of simple flows and analysis of nonslip boundary conditions for the lattice Boltzmann BGK model. *Journal of Statistical Physics*, 87(1-2):115–136, 1997.
- [136] A. J. C. Ladd. Numerical simulations of particulate suspensions via a discretized Boltzmann equation. Part 1. Theoretical foundation. *Journal of Fluid Mechanics*, 271(1):285–309, 1994.
- [137] C. K. Aidun, Y. Lu, and E. J. Ding. Direct analysis of particulate suspensions with inertia using the discrete Boltzmann equation. *Journal of Fluid Mechanics*, 373:287–311, 1998.
- [138] H. Kruggel-Emden, E. Simsek, S. Rickelt, S. Wirtz, and V. Scherer. Review and extension of normal force models for the Discrete Element Method. *Powder Technology*, 171(3):157–173, 2007.
- [139] F. Lominé and L. Oger. Dispersion of particles by spontaneous interparticle percolation through unconsolidated porous media. *Phys. Rev. E*, 79(5):1–12, 2009.
- [140] S. Dippel J. Schäfer and D. E. Wolf. Force schemes in simulations of granular materials. *J. Phys. I France*, 6:5–20, 1996.
- [141] T. Schwager and T. Pöschel. Coefficient of restitution and linear-dashpot model revisited. *Granular Matter*, 9(6):465–469, 2007.
- [142] F. Lominé and L. Oger. Transit time during the interparticle percolation process. *Physical Review E*, 82(4):041301, October 2010.
- [143] H. J. Herrmann F. Alonso-Marroquin, R. Garcia-Rojo. *Micro-mechanical investigation of the granular ratcheting*. In T. Triantafyllidis (Ed.), *Cyclic Behaviour of Soils and Liquefaction Phenomena*. Taylor & Francis, 2004.

- [144] D. O. Potyondy and P. A. Cundall. A bonded-particle model for rock. *International Journal of Rock Mechanics and Mining Sciences*, 41(8 SPEC.ISS.):1329–1364, 2004.
- [145] L. Verlet. Computer "experiments" on classical fluids I. Thermodynamical properties of Lennard-Jones molecules. *Physical Review*, 159(5), 1967.
- [146] M. Yang, S. Li, and Q. Yao. Mechanistic studies of initial deposition of fine adhesive particles on a fiber using discrete-element methods. *Powder Technology*, 248:44–53, 2013.
- [147] M. Ouyang and B. Y. H. Liu. Analytical solution of flow field and pressure drop for filters with noncircular fibers. *Aerosol Science and Technology*, 23(3):311–320, 1995.
- [148] A. D. Araújo, J. S. Andrade, and H. J. Herrmann. Critical role of gravity in filters. *Physical Review Letters*, 97(13):138001, September 2006.
- [149] K. Luo, F. Wu, K. Qiu, Z. Wang, and J. Fan. Effects of preferential concentration on collision and erosion between solid particles and tube bank in a duct flow. *International Journal of Heat and Mass Transfer*, 83:372–381, 2015.
- [150] S. Elghobashi. Particle-laden turbulent flows: direct simulation and closure models. *Applied Scientific Research*, 48:301–314, 1991.
- [151] J. Yao and M. Fairweather. Inertial particle resuspension in a turbulent, square duct flow. *Physics of Fluids*, 22(3):1–15, 2010.
- [152] B. M. Rabiee, S. Talebi, O. Abouali, and E. Izadpanah. Investigation of the characteristics of particulate flows through fibrous filters using the lattice Boltzmann method. *Particuology*, 21:90–98, 2015.
- [153] K. Wang and H. Zhao. The influence of fiber geometry and orientation angle on filtration performance. *Aerosol Science and Technology*, 49(2):75–85, 2015.
- [154] M. Ouyang and B. Y. H. Liu. Analytical solution of flow field and pressure drop for filters with rectangular fibers. *Journal of Aerosol Science*, 29(1-2):187–196, 1998.
- [155] W. Li, S. Shen, and H. Li. Study and optimization of the filtration performance of multi-fiber filter. *Advanced Powder Technology*, 27(2):638–645, 2016.

-
- [156] H. Duval, D. Masson, J. B. Guillot, P. Schmitz, and D. D'Humières. Two-dimensional lattice-Boltzmann model of hydrosol depth filtration. *AIChE Journal*, 52(1):39–48, 2006.

Résumé en français

Chapitre 1 Revue de la littérature sur l'interaction hydrodynamique et mécanique du fluide et du solides particules

Les écoulement diphasique fluide-solide sont fréquemment rencontrés dans la nature et le domaine de l'ingénierie. On peut par exemple citer les industries minières et cimentières, le transport de particules dans les filtres, l'industrie de la production d'énergie ainsi que l'ingénierie environnementale. L'écoulement fluide-solide soulève un grand nombre de problèmes scientifiques en termes de complexité des mécanismes physiques.

L'écoulement des suspensions à travers le milieu poreux est un phénomène commun. Les équations de Navier-Stokes sont généralement utilisées pour résoudre le champ du fluide dans les milieu poreux. La fraction du volume des pores sur le volume total dans les milieux poreux est appelée porosité qui est un paramètre très important. D'une manière générale, il existe trois types de porosité, porosité intergranulaire, porosité à la rupture et porosité caverneuse. Considérons le milieu poreux composé de sphère, pour arrangé régulièrement, les quatre types les plus communs de cellules unitaires sont les cubes cubiques simples (SC), cubiques centrés sur le corps (BCC), cubes à faces centrées (FCC) et hexagonales (HCP) . La porosité maximale des milieux poreux correspondant à SC est de 47,6%. Pour arrangé au hasard, la limite supérieure de la porosité est de 36%. La loi de Dracy et l'équation de Kozeny-Carman sont souvent utilisées dans l'écoulement des fluides dans les milieux poreux. Pour des configurations simples de milieux poreux, la solution de Kuwabara peut être utilisée pour déterminer le champ de vitesse du fluide.

La séparation fluide-particules fait référence à un procédé de filtration de particules transportée par un fluide. La compréhension et la maîtrise de la filtration de particules sont très importante en raison de sa forte utilisation dans les activités humaines. En

ce qui concerne le transport et le dépôt de particules dans des milieux poreux, le dépôt de particules à la surface des milieux poreux peut modifier la morphologie des pores. L'accumulation de particules entraîne un colmatage progressif du filtre. En conséquence, la perméabilité diminue et la chute de pression augmente, ce qui détériore la durée de vie du filtre. Ainsi, il est essentiel d'estimer quantitativement une performance de filtre.

En termes de processus de filtration, différents de types de filtration existent, ils peuvent être classés en filtration de gâteau, filtration granulaire, filtration fibreuse, etc. Le transport de particules à travers les milieux poreux est un phénomène très complexe dû à la diversité des mécanismes impliqués. Dans la filtration, le facteur de qualité, γ compris l'efficacité de filtration et la chute de pression, est utilisé pour évaluer les qualité de filtration. L'efficacité de filtration du milieu filtrant propre est liée à l'efficacité de la capture de fibre isolé. La relation entre eux peut être créée en raison de différents mécanismes de capture, tels que la diffusion brownienne, l'interception et l'impaction inertielle. La capture de particules via la diffusion brownienne est liée au nombre adimensionnel appelé nombre de Péclet (Pe). Le coefficient d'interception, un paramètre adimensionné, (R) est utilisé pour décrire l'effet de l'interception. L'impaction inertielle est quant à elle régie par le paramètre adimensionnel appelé nombre de Stokes (St). La séparation des particules du fluide nécessite un système de filtration à haute efficacité avec une faible chute de pression. La prédiction de la chute de pression à travers un filtre est donc très importante. Il peut être directement évalué à partir du débit de fluide. L'arrangement des fibres et la géométrie des fibres ont également une influence significative sur l'efficacité de la capture et la chute de pression. Ces dernière années, le processus de filtration de particule a été étudié par de nombreux chercheurs. Plusieurs modèles mathématiques ont été proposés et des investigations expérimentales ont été effectuées pour prédire et améliorer la chute de pression et l'efficacité de la capture.

Chapitre 2 Méthods numérique LBM et DEM

Dans ce chapitre, nous présentons une méthode numérique couplant la méthode lattice Boltzmann (LBM) et la méthode des éléments discrets (DEM). L'écoulement du fluide est calculé par la LBM tandis que la dynamique des particules est simulée via la DEM.

Nous utilisons le modèle classique D2Q9. Le domaine de calcul dans la méthode LBM est d'abord divisé en un maillage carré régulier. La phase liquide dans LBM est alors supposée comme un groupe de particules de fluide se trouvant à chaque nœud du réseau. Elles sont contraintes de migrer le long des liens vers le nœuds les plus proches et d'entrer

en collision les unes avec les autres aux niveau de nœuds.

Les variables microscopiques des fluides comme la densité du fluide et la vitesse du fluide peuvent être déduites des moments de la fonction de distribution.

$$\rho = \sum_{i=0}^8 f_i \quad (4.5)$$

$$\vec{u} = \frac{1}{\rho} \sum_{i=0}^8 f_i \vec{e}_i \quad (4.6)$$

La DEM est une approche numérique très populaire pour traiter les interactions de contact entre particules solides. Les particules se déplacent selon la loi de Newton et leurs contacts sont modélisés par un loi de contact basée sur une approche de sphères légèrement déformables. Nous utilisons le modèle LSD (linear spring dashpot) et une extension de la méthode proposée par Cundall-Strack, pour modéliser respectivement la force de contact normale et la force de contact de cisaillement.

Les forces hydrodynamiques et les moments résultants sont déduits du calcul LBM et utilisés dans le cycle DEM pour calculer de nouvelles positions et vitesses de particules solides, qui à leur tour définissent les nouvelles conditions aux limites pour le problème de la dynamique des fluides. La réalisation du couplage LBM-DEM est faite en considérant que chaque méthode est caractérisée par une discrétisation temporelle différente. Les méthodes LBM-DEM couplées sont implémentées dans un code "maison" développé au Laboratoire de Génie Civil et Génie Mécanique (LGCGM) dénommé "Albadec".

Les problèmes classiques de mécanique des fluides sont présentées afin de valider le code de calcul 2D basé sur l'algorithme LBM et sur le couplage des LBM-DEM respectivement. Les résultats de la simulation de l'écoulement de Poiseuille, l'écoulement de Couette et de l'écoulement autour d'un cylindre circulaire sont présentés.

Chapitre 3 Simulation numérique de la capture de particules sur une seule fibre

Dans ce chapitre, nous étudions l'effet de la taille des particules d_p et du nombre de Stokes St sur l'efficacité de la capture des particules en utilisant deux méthodes. La première est un couplage unidirectionnel combinant la méthode Lattice Boltzmann (LBM) avec une approche ponctuelle Lagrangienne. La seconde est un couplage bidirectionnel basé

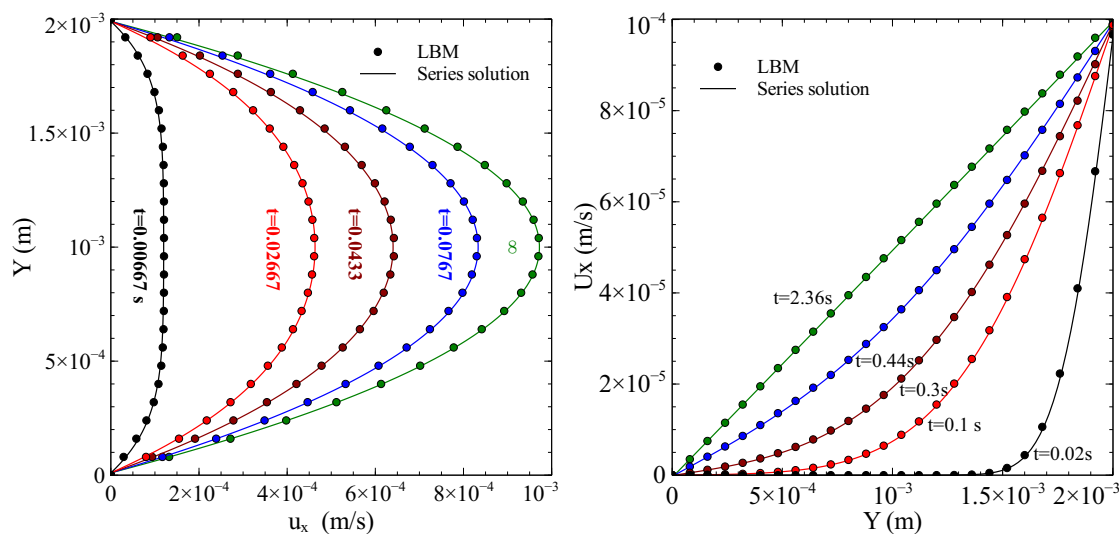


Figure 4.29: Comparaison du profil de vitesse obtenu avec la LBM et des solutions en série pour l'écoulement de Poiseuille et l'écoulement de Couette.

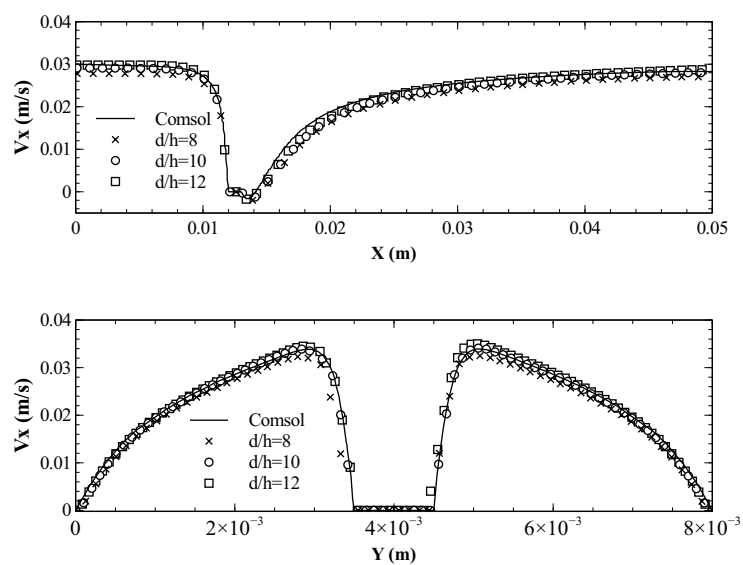


Figure 4.30: Profils de vitesse obtenus avec la méthode LBM et avec un logiciel CFD pour un écoulement de fluide circulant autour d'un cylindre circulaire

sur le couplage entre la méthode Lattice Boltzmann (LBM) et la méthode des éléments discrets (DEM). Contrairement à la première méthode, cette dernière permet de prendre en compte l'action des particules sur le fluide. Nous nous concentrons sur l'étude pour trouver la taille de particule critique entre la méthode de couplage unidirectionnelle et bidirectionnelle. Puis l'efficacité de la capture d'une fibre, caractérisée par le nombre de Stokes (St), et le facteur de qualité sont étudiés par les méthodes LBM-DEM.

Le transport et le dépôt de particules à la surface d'une fibre de section circulaire, losange et carré sont simulés par la méthode de couplage unidirectionnel et LBM-DEM. Les trajectoires des particules ainsi que les lignes de courant sont analysées pour les écoulement autour des fibres circulaires, losanges et carrées. L'efficacité de la capture en fonction de St est comparée avec d'autres travaux. Le facteur de qualité de la fibre isolé est calculés dans les différents cas.

La Fig.4.31 présente le champ de vitesse du fluide et la position des particules pour des écoulement autour de fibres circulaires, losanges et carrées.

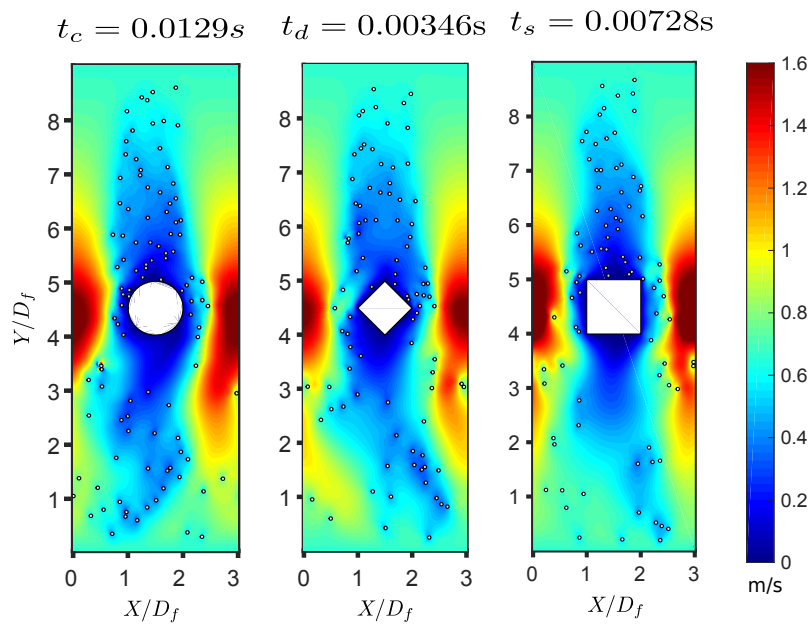


Figure 4.31: Champ de vitesse du fluide et position des particules dans les cas d'écoulements autour de fibres de sections différentes (circulaire, carrée et diamantée), pour $St = 0.5$.

Ensuite, L'effet de l'orientation et du rapport d'aspect d'une fibre rectangulaire sur la chute de pression, sur l'efficacité de la capture, puis sur le facteur de qualité été étudiés numériquement pour différents nombres de Reynolds.

La Fig.4.32 représente l'image instantanée du champ de vitesse du fluide et de la position

des particules pour des angles d'orientation de la fibre rectangulaire différents. Elle met en évidence que le transport de particules affecte grandement le champ de vitesse du fluide.

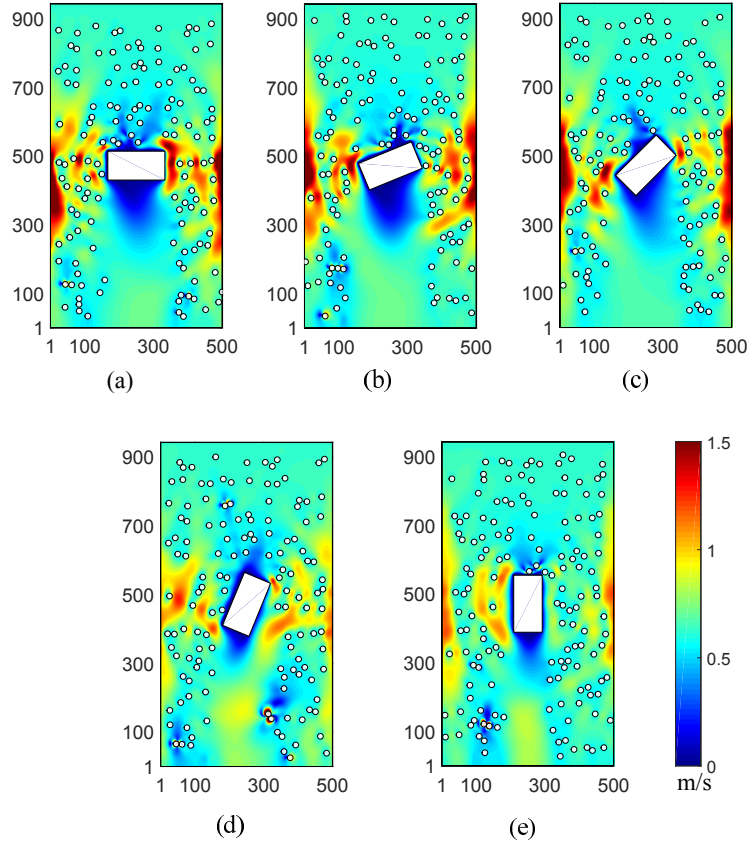


Figure 4.32: Champ de vitesse du fluide et distribution des particules pour $St = 8.33$, $Re = 8$, (a) $\theta = 0$, (b) $\theta = 1/8\pi$, (c) $\theta = 1/4\pi$, (d) $\theta = 3/8\pi$, (e) $\theta = 1/2\pi$.

La Fig.4.33 (a) représente la relation entre le facteur de qualité et le nombre de Reynolds pour différents rapports d'aspect. Pour $\theta = 0$, le facteur de qualité diminue rapidement lorsque Re varie de 2 à 4, puis change graduellement lorsque Re varie de 4 à 10. En effet, la chute de pression augmente plus rapidement que l'efficacité de la capture, ce qui entraîne une baisse du facteur de qualité. La Fig.4.33 (b) montre l'effet de l'angle d'orientation sur le facteur de qualité pour $Re = 8$. Le facteur de qualité pour la fibre rectangulaire augmente d'abord avec l'angle d'orientation, puis diminue.

Suite à l'étude réalisé dans ce chapitre, les conclusions suivantes peuvent être formulées :

- Pour les petites particules $d_p \leq 8 \mu\text{m}$, le couplage unidirectionnel dans notre modèle est suffisamment précis pour estimer le transport et le dépôt des particules. L'efficacité de

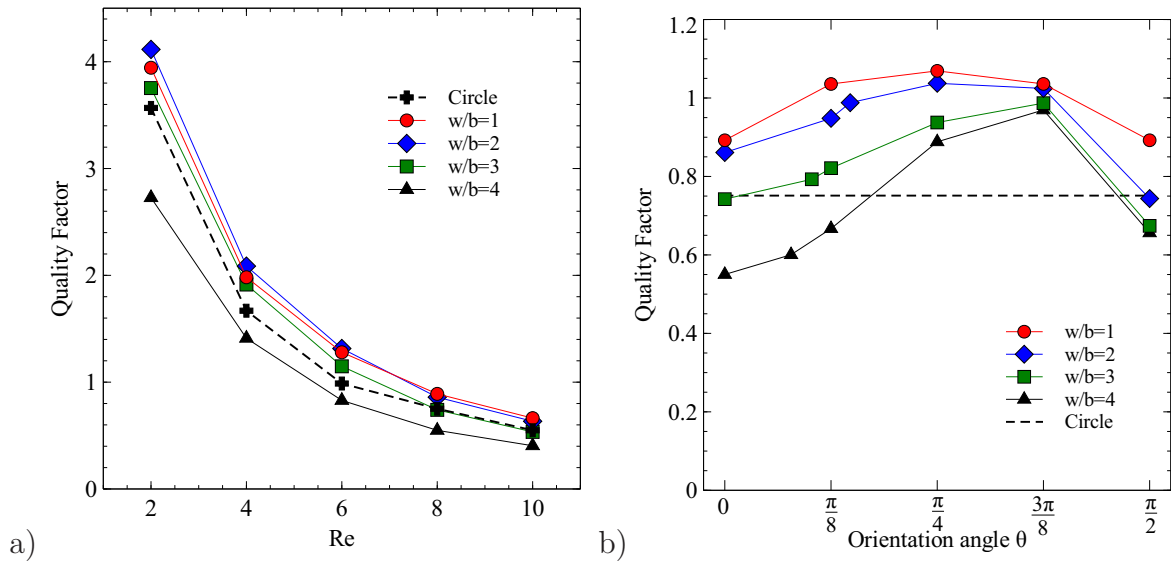


Figure 4.33: Facteur de qualité en fonction de Re , $\theta = 0$ (a). Facteur de qualité en fonction de l'angle d'orientation, $Re = 8$ (b)

la capture de notre simulation concorde bien avec les résultats d'Araujo et al. Cependant, en ce qui concerne les particules plus grosses, le couplage bidirectionnel est beaucoup plus pratique en raison de la prise en compte de l'influence du mouvement des particules sur l'écoulement.

- L'impaction des particules sur la face avant de la fibre de forme carrée est plus important que sur les fibres circulaires et losanges.

- La fibre de losange présente une meilleure performance en termes de facteur de qualité.

- La chute de pression causée par la fibre dépend non seulement de l'angle d'orientation, mais aussi du nombre de Reynolds lorsque $2 \leq Re \leq 10$.

- En ce qui concerne l'efficacité de la filtration avec une fibre rectangulaire, elle dépend à la fois de l'angle d'orientation et du rapport d'aspect. Cependant, l'efficacité de la filtration augmente légèrement avec Re .

- En termes de qualité de filtration en prenant en compte l'efficacité de la capture et la chute de pression, le facteur de qualité diminue avec le nombre de Reynolds pour $\theta = 0$. Cependant, le facteur de qualité augmente avec l'angle d'orientation et atteint son maximum à une certaine valeur, puis diminue. On trouve que le facteur de qualité le plus grand est obtenu pour la fibre carrée à $\theta = \pi/4$

Chapitre 4 Simulation numérique du processus de filtration pour filtre à fibre disposées en quinconce

L'agencement des fibres, tel que le mode parallèle et le mode en quinconce, influence de manière significative les performances de filtration, y compris l'efficacité de la capture et la chute de pression. Généralement, dans les mêmes conditions, le modèle en quinconce est meilleur que le modèle en parallèle en termes de qualité de filtration, car le modèle en quinconce présente un rendement de la capture plus élevé alors que la chute de pression est quasiment identique.

Dans ce chapitre, d'abord, nous présentons trois types d'arrangements de fibres, l'un à côté de l'autre, l'un en dessous de l'autre et en quinconce. L'efficacité de capture de fibre unique obtenue à partir du travail expérimental de Schweers et al et nos résultats de simulation sont comparés pour trois configurations de fibres. Ensuite, le processus de filtration du filtre avec des fibres circulaires, losange et carrées disposées en quinconce ont été étudié numériquement. Les effets du nombre de Reynolds, du rapport entre le diamètre des particules et les fibres (R) et du rapport entre la masse volumique des particules et le fluide (ε) sur la chute de pression et l'efficacité de la capture sont étudiés. Pour R on fait varier le diamètre des particules et pour ε on fait varier la masse volumique des particules. Les résultats des simulations de circulaire, losange et carée sont comparés pour explorer l'effet de la forme transversale de la fibre sur les facteur de qualité.

La Fig.4.34 présente les champs d'écoulement autour de la fibre avec différentes formes pour un nombre de Reynolds $Re = 5$. Une partie des lignes de courant dans le domaine de calcul sont représentées. On remarque que les lignes de courant proches de la fibre carrée changent remarquablement. De toute évidence, la forme de la section transversale de la fibre modifie la structure du champ de fluide qui conduit à la variation de la chute de pression à travers le filtre.

La Fig.4.35 a) présente le facteur de qualité en fonction de R pour les masses volumiques des particules élevées et faibles. Pour les particules de masse volumique élevées, les fibres losanges présente une meilleure qualité que les fibres circulaires et carrés. Cependant, pour les masses volumiques faibles, les fibres carrées ont le facteur de qualité le plus élevé en ce qui concerne $R = 0,05$ et $\varepsilon = 600$. Alors le facteur de qualité du losange et circulaire augmente remarquablement par rapport au carré, ce qui indique une meilleure performance pour $0.075 \leq R \leq 0.15$. La Fig.4.35 b) présente le facteur de qualité en fonction de ε . On peut observer que le facteur de qualité de trois fibres est indépendant de ε pour $R = 0.15$.

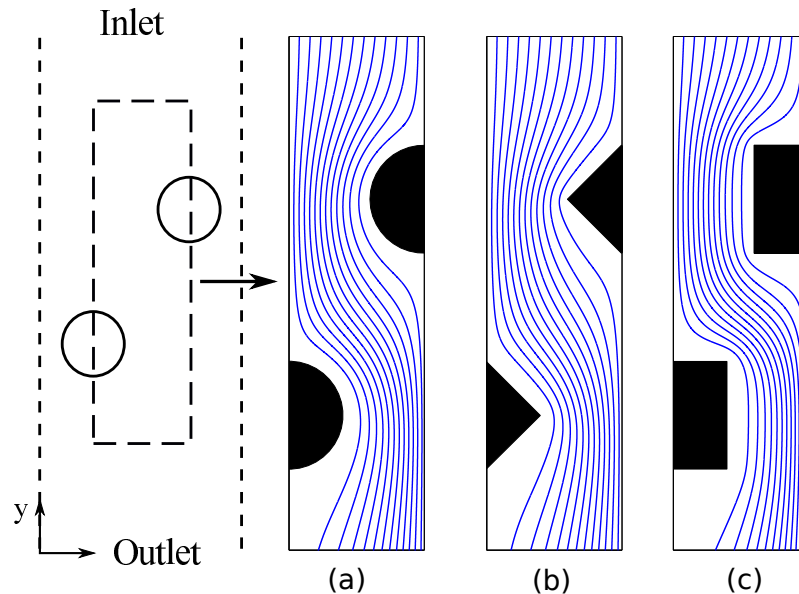


Figure 4.34: Représentation des lignes de courant autour des fibres de sections transversales différentes (circulaire, losange et carré).

Cependant, pour $R = 0.05$, le facteur de qualité de trois fibres augmente avec ε .

Sur la base de l'étude présentée dans ce chapitre, les conclusions suivantes peuvent être formulées :

- Pour trois types d'arrangements de fibres, les configurations en quinconce sont plus efficaces pour capturer les particules.

- Le filtre à fibre de section losange a une chute de pression inférieure à celle des cas circulaire et de carré.

- Pour l'efficacité de la capture, lorsque le nombre de Reynolds augmente, le nombre de particules capturées par les fibres augmente pour les particules de petite taille. Cependant, l'efficacité de la capture des fibres circulaires, losanges et carrées est indépendante de Re pour les grosses particules.

- Une augmentation du rapport R entre le diamètre de la particule et celui de la fibre conduit à une augmentation de la capture des particules. Ceci est d'autant plus vrai pour les fibres de formes circulaires et losanges comparativement à celles de formes carrées.

- L'efficacité de la capture des trois types de fibres augmente avec ε pour les petites particules, mais elle est indépendante de ε pour les grosses particules en raison de la forte force d'inertie.

- En termes de facteur de qualité, combinant l'effet de la capture et la chute de pression, le filtre à fibre de losange présente une meilleure qualité de filtration pour deux cas (1)

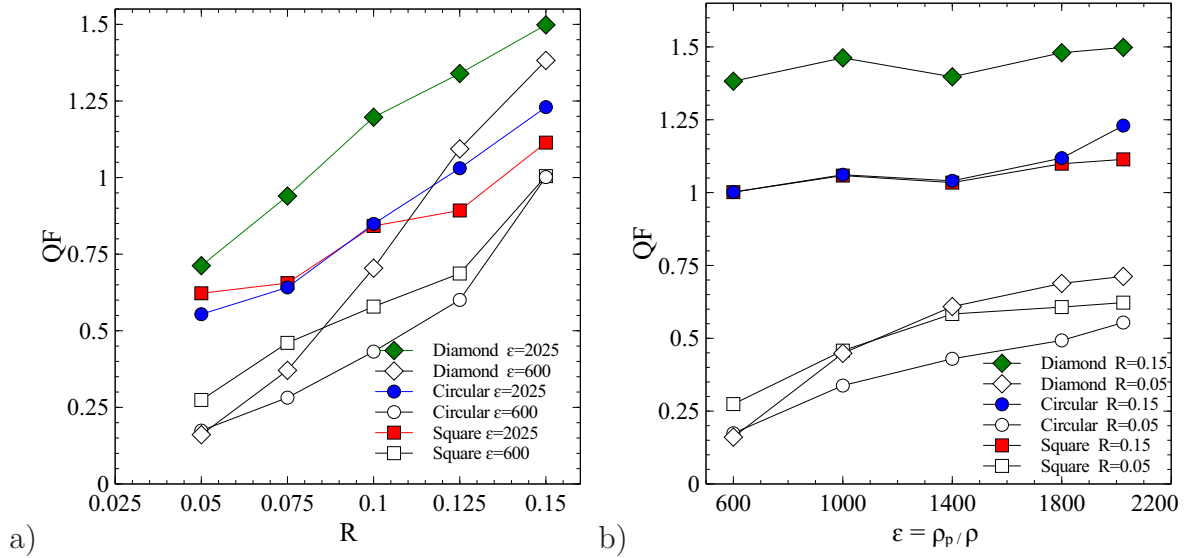


Figure 4.35: Facteur de qualité QF en fonction de a) R et b) ε .

$\varepsilon = 2025$ et $0.05 \leq R \leq 0.15$, (2) $R = 0.15$ et $600 \leq \varepsilon \leq 2025$.

Conclusions et Perspectives

Enfin dans une dernière partie, on présente les conclusions et perspectives de ce travail. Plus précisément, des simulations numériques ont été effectuées pour étudier le flux diphasique fluide-solide. Des méthodes de Lattice Boltzmann (LBM) et d'éléments discrets (DEM) ont été développées pour étudier le transport et le dépôt de particules dans des milieux poreux. La qualité de filtration du filtre, y compris l'efficacité de la capture et la chute de pression, ont été étudiées et analysées dans le cas de fibres circulaires, losanges et carrées. Les facteurs de qualité du filtre sont également estimés. Cette étude aide à analyser comment les propriétés des particules et du fluide déterminent la qualité de filtration et affectent le processus de filtration des particules.

Pour finir, ce manuscrit présente plusieurs perspectives de recherche afin de poursuivre les études réalisées au cours de cette thèse.

AVIS DU JURY SUR LA REPRODUCTION DE LA THESE SOUTENUE

Titre de la thèse:

Numerical study of particle transport and deposition in porous media

Nom Prénom de l'auteur : FAN JIANHUA

Membres du jury :

- Monsieur HELLOU Mustapha
- Monsieur LOMINE Franck
- Monsieur MARTINEZ Juan
- Monsieur WANG Huaqing
- Monsieur LECOQ Nicolas
- Monsieur HEITZ Dominique
- Madame AHMADI SENICHAULT Azita
- Monsieur BEAUDOIN Anthony

Président du jury : *Azita* AHMADI-SENICHAULT

Date de la soutenance : 29 Mars 2018

Reproduction de la these soutenue

- Thèse pouvant être reproduite en l'état
 Thèse pouvant être reproduite après corrections suggérées

Fait à Rennes, le 29 Mars 2018

Signature du président de jury

Le Directeur,

M'hamed DRISSI



A handwritten signature in black ink, appearing to be "A. Senichault", written over a horizontal line.

Résumé

L'objectif de ce travail de recherche est d'étudier numériquement le transport et le dépôt de particules dans des milieux poreux à l'échelle des pores.

Premièrement, un couplage entre la méthode de Boltzmann sur réseau (LBM) et la méthode des éléments discrets (DEM) est réalisé et utilisé pour simuler l'écoulement d'un fluide chargé en particules. La LBM est utilisée pour décrire l'écoulement du fluide autour des fibres tandis que la DEM est utilisée pour traiter la dynamique des particules. Ce couplage est bidirectionnel dans le sens où le mouvement des particules affecte le flux de fluide et réciproquement. Ce modèle nous a permis de prédire l'efficacité de capture et la chute de pression à l'étape initiale du processus de filtration. Le facteur de qualité est également calculé pour déterminer la qualité de filtration.

Ensuite, on se focalise sur l'étude de l'efficacité de la capture de fibres de formes de section transversale différentes (circulaire, losange et carrée). Les résultats issus de nos simulations du processus de filtration de la fibre circulaire concordent bien avec les corrélations empiriques. L'impact des particules sur la face avant de la fibre de forme carrée est plus important que dans les cas de fibre de formes circulaire et losange. Cependant, en raison d'une chute de pression plus faible, la fibre de section losange présente une meilleure qualité de filtration. Ensuite, les variations du facteur de qualité dues à l'angle d'orientation et au rapport d'aspect des fibres ont été étudiées numériquement pour la forme rectangulaire. Pour chaque cas, on a déterminé la valeur optimale de la zone au vent pour laquelle le facteur de qualité est maximal. La comparaison des valeurs du facteur de qualité obtenues pour les différentes formes de fibre montre une meilleure performance pour la fibre de section carrée orientée avec un angle de $\pi/4$.

Enfin, l'influence de l'arrangement des fibres sur la qualité de la filtration est analysée en considérant la configuration en quinconce pour les différentes formes. Les simulations conduites pour différentes tailles de particules et différentes valeurs de la densités (particule/air) montrent que la fibre de section losange est plus performante en termes de facteur de qualité pour les particules de grande taille et pour les valeurs de densité élevée. La présente étude fournit des pistes pour optimiser le processus de filtration et prédire la qualité de filtration.

Mots-clef : Méthode de Boltzmann sur réseau, méthode des éléments discrets, transport et dépôt de particules, efficacité de la capture, filtration des particules, filtre.

Abstract

The objective of the present research was to numerically investigate the transport and deposition of particles in porous media at the pore scale.

Firstly, a developed coupled lattice Boltzmann method (LBM) and discrete element method (DEM) is used to simulate the fluid-particle flow. LBM is employed to describe the fluid flow around fibers whereas DEM is used to deal with the particle dynamics. The corresponding method is two-way coupling in the sense that particle motion affects the fluid flow and reciprocally. It allowed us to predict the capture efficiency and pressure drop at the initial stage of filtration process. The quality factor is also calculated for determining the filtration performance.

Secondly, we focus on the study the capture efficiency of single fiber with circular, diamond and square cross-section, respectively. The results of LBM-DEM for filtration process of single circular fiber agree well with the empirical correlation. The impact of particles on the front side of square-shaped fiber is more favorable than those on circular and diamond cases. However, diamond fiber exhibits a good filtration performance. Then the variations of quality factor due to the different orientation angle and aspect ratio of rectangular fiber were studied using LBM-DEM. For each case, we have found the optimal value of the windward area to which corresponds a maximum value of the quality factor. The comparison of the performance of the different forms of fibers shows that the largest quality factor is obtained for square fiber oriented with angle $\pi/4$.

Finally, the influence of the arrangement of fiber on filtration performance is analyzed by considering the staggered configuration. Simulations conducted for several particle size and density show that the diamond with staggered array performs better for large particles and high particle-to-fluid density ratio in terms of quality factor. The present study provide an insight to optimize the filtration process and predict filtration performance.

Keywords: Lattice Boltzmann method, discrete element method, particle transport and deposition, capture efficiency, particle filtration, filter.